

# Asteroid Muography

Design feasibility of a hodoscopic  
spacecraft-based detector in-  
tended for muon tomography of  
asteroid interiors

R. David D. Hodge

Technische Universiteit Delft

# Asteroid Muography

## Design feasibility of a hodoscopic spacecraft-based detector intended for muon tomography of asteroid interiors

by

R. David D. Hodge

to obtain the degree of Master of Science  
at the Delft University of Technology,  
to be defended publicly on October 19, 2018.

Student number: 4625765  
Project duration: January 28, 2018 – October 19, 2018  
Thesis committee: Dr. ir. A. Menicucci, TU Delft, supervisor  
Dr. D. Stam, TU Delft, supervisor  
Prof. dr. ir. P.N.A.M. Visser TU Delft, committee chair

An electronic version of this thesis is available at <http://repository.tudelft.nl/>.  
Cover Photo is of Comet 67P/Churyumov-Gerasimenko, courtesy of ESA, Rosetta Mission  
Images [5]

# Acknowledgements

There are any number of witty, cliched, quotations regarding the fact that no action undertaken by humanity occurs in a vacuum. Probably because it's true. At the risk of overburdening what should be a simple nicety at the beginning of this work, it is all too easy take this assertion that no one exists in a vacuum to extremes and draw causal connections between this work and more people and circumstances than would fit on just one page, let alone ever actually be read. To wit, in the interests of that oft-elusive quality of concision I shall borrow a bit of formalism from the language used to describe mathematical theorems:

$$A \ni \left\{ \begin{array}{ll} \text{Katherine} & \text{Drapeau} \\ \text{Robert} & \text{Hodge} \\ \text{Beverly} & \text{Drapeau} \\ \text{Bill} & \text{Drapeau} \\ \text{Alessandra} & \text{Menicucci} \\ \text{Daphne} & \text{Stam} \\ \text{Sean} & \text{Pepper} \end{array} \right\}$$

Where  $A$  is the group of the contributors most causally linked to the success of this undertaking through personal support and or academic guidance.

In addition, I'd like to express thanks to Kevin Lynch and Fan Li, who wrote, and shared to an open source forum, a critical piece of code that I have used extensively in my simulations. My fellow users on that selfsame online community, the Stanford SLAC Geant4 forum, have also provided key insights on occasion that have indubitably saved weeks or months of trial and tribulation.

*R. David D. Hodge  
Delft, October 2018*

# Abstract

Asteroids, or more formally, Small Solar System Bodies, offer a wealth of scientific knowledge and, increasingly, economic potential. Regrettably, because of their small size and the fact that the largest groups of asteroids in the solar system are situated tens of millions of kilometers from Earth, ground based observations yield limited data, mostly confined to surface characteristics. To date, space missions traveling to asteroids, or other SSSBs, have also been principally focused upon collecting data from the surface, or within approximately 2m thereof. More penetrative interior survey methods exist in terrestrial application, but methods like seismology and core drilling would require specific equipment and direct landing on the asteroid.

Muography potentially presents a means of going in-between these two extremes of the study of asteroid interiors. High energy galactic cosmic ray primaries constantly, and randomly, impact all objects in the solar system, generating secondary showers of particles when they interact with stationary matter. Of primary interest to this project, unsurprisingly, are muons. These particles have a considerable mass, are generally very energetic ( $> 200$  MeV), and exist in positive or negative species with a charge magnitude equal to that of 1 electron[36]. These factors contribute to a very low energy loss through conventional mechanisms like ionization, bremsstrahlung, or pair production, making muons very penetrative.

Their high energy, highly penetrative nature, and relative abundance as GCR secondaries present an opportunity to perform radiography of the inside of rocks of considerable magnitude. Prettyman et al, who have performed initial analyses of the space-borne tomographic methodology itself, estimate that the interior of asteroids up to 1km in diameter may be surveyed with this technique.

This report details the project of a feasibility study for a small-scale hodoscopic detector of the type that could be flown with a somewhat standardized satellite bus no larger than the commonly-used "small" or "micro" satellite categories.

The result of the final design trade study was a hodoscopic detector with 3 sensitive planes, internal, inter-plane, shielding made of layered aluminum and high density polyethylene (HDPE). The particle sensors consist of two semi-conductor based PSD arrays per sensitive plane sandwiching a dual-layer "grid" of borosilicate glass paddles designed to take advantage of the Cherenkov effect caused by transiting, high energy, charged particles. Any such transiting particle that successfully passes through the entire detector, and which successfully meet all of the criteria of the basic active shielding algorithm designed for this project, have a 72% chance of being muons.

This ID probability is aided in the overall success of muon discrimination by the simulation finding that the asteroid itself blocks most high-energy GCR primaries with trajectories that would pass through the field of view of the detector. Furthermore, backscatter radiation from primary-particle impacts on the sand-side surface of the asteroid model is almost universally of either relatively low energy that is easily filtered out by the active shielding algorithm, or muons that have most likely transited the asteroid from the opposing side. In simulations, more than 70% of backscatter particles were less than 200 MeV, which is below the detection threshold of the instrument. Of the two outlying backscattered particle groups that were not below this threshold, the 6GeV alpha particles had an extremely low flux, and the 2GeV protons exhibited a maximum flux of less than 5 particles  $m^{-2}s^{-2}sr^{-1}GeV^{-1}$ . While this flux is significant compared with the expected flux of transmitted muons, it is insignificant compared to the fluxes of GCR primary particles of far higher energy that the instrument was already tested against.

Ultimately, independent simulation results from the instrument-centered trials and the asteroid-centered trials both lend evidence to support the conclusion that such a space-based detector aimed at muography *is* feasible, and that a detector similar to that which was ultimately selected in the final-trade study would be a decent place to start in more detailed design studies. One further critical conclusion, and recommendation, that resulted from the final comparison of separate environmental and instrument simulations, is that, while not realistically possible for this project, access to a high performance computing cluster could easily allow *combined* environment+instrument simulation.

There was, indeed, a bit of extra time at the end of the study to attempt a much (much) reduced version of such a simulation, and, while it was ultimately not of sufficient quality to use in the concluding arguments of this thesis, it did hint at interesting behaviors that might fall out of an integrated simulation. Perhaps the most intriguing hint found was that there could be some orbital altitudes at which a muographic instrument could experience transmitted-muon fluxes significantly higher than the inverse square law of radiant intensity would predict. Future investigation of this potential phenomenon is strongly suggested.

# Contents

<b>List of Figures</b>	<b>vii</b>
<b>List of Tables</b>	<b>ix</b>
List of Symbols & Abbreviations . . . . .	xii
<b>1 Introduction</b>	<b>1</b>
1.1 Project Framework . . . . .	2
1.1.1 Design Philosophy . . . . .	2
1.1.2 Project Scope . . . . .	4
<b>2 Background</b>	<b>6</b>
2.1 Environment . . . . .	6
2.1.1 Asteroids . . . . .	6
2.1.2 Particle Radiation Theory . . . . .	12
2.1.3 Radiation Environment . . . . .	20
2.2 Detection Methods . . . . .	22
2.2.1 Photon-based Particle Detectors . . . . .	22
2.2.2 Semiconductor Detectors . . . . .	28
<b>3 Simulation</b>	<b>30</b>
3.1 Instrument Simulation . . . . .	30
3.1.1 SiPM Simulation . . . . .	30
3.1.2 Scintillation Simulation . . . . .	32
3.1.3 Cherenkov Simulation . . . . .	38
3.2 Asteroid Simulation . . . . .	44
3.2.1 Asteroid Model . . . . .	44
3.2.2 Asteroid Radiation Environment Simulation . . . . .	46
<b>4 Design</b>	<b>56</b>
4.1 Assumptions . . . . .	56
4.1.1 Mission . . . . .	56
4.1.2 Physics and Simulation . . . . .	57
4.1.3 Detector Design . . . . .	58
4.1.4 Spacecraft Design . . . . .	63
4.2 Requirements . . . . .	64
4.3 Preliminary Design Trade Studies . . . . .	66
4.3.1 High Level Trade Study . . . . .	66
4.3.2 Mid Level Trade Study . . . . .	68
4.3.3 Implication of Initial Simulation Results . . . . .	74
4.4 Final Design Trade Study . . . . .	76
4.4.1 Active Shielding Algorithm . . . . .	76
4.4.2 Parametric Study on Boundary Conditions . . . . .	79
4.4.3 Parametric Study on Geometric Configuration . . . . .	82
<b>5 Verification and Validation</b>	<b>90</b>
5.1 Instrument Simulation Verification . . . . .	91
5.1.1 Basic Physics Test . . . . .	91
5.2 Asteroid Environment Simulation Validation . . . . .	98
<b>6 Conclusions &amp; Recommendations</b>	<b>102</b>
6.1 Review of Research Questions . . . . .	102

---

6.2	Conclusions & Recommendations . . . . .	105
6.2.1	Recommendations . . . . .	105
<b>A</b>	<b>Mid Level Trade off AHP Matrix</b>	<b>108</b>
<b>B</b>	<b>Limited Instrument/Environment Combined Simulation</b>	<b>109</b>
	<b>Bibliography</b>	<b>114</b>

# List of Figures

2.1 Oort Cloud and Kuiper Belt . . . . .	7
2.2 Main Asteroid Belt and Trojans . . . . .	7
2.3 Asteroid Density . . . . .	9
2.4 Asteroid 25143 Itokawa . . . . .	10
2.5 Asteroid 4179 Toutatis . . . . .	10
2.6 GCR Primary Intensities . . . . .	12
2.7 Ionization Momentum Geometry . . . . .	14
2.8 Muon Critical Energy . . . . .	17
2.9 Atmospheric Muon Flux . . . . .	20
2.10 Lunar Surface Radiation Dosage . . . . .	22
2.11 Benzene Static Bond Structure . . . . .	23
2.12 Benzene Electron-Cloud Bond Structure . . . . .	23
2.13 Linear Cata-condensed Hydrocarbons . . . . .	24
2.14 Organic Molecule Electron Energy Levels . . . . .	24
2.15 Low Speed Particle in Dielectric Medium . . . . .	25
2.16 High Speed Particle in Dielectric Medium . . . . .	26
2.17 Cherenkov Threshold . . . . .	26
2.18 SiPM/SPAD Passive Pulse Shape . . . . .	27
2.19 SiPM Microstructure . . . . .	28
2.20 SiPM Frequency Response . . . . .	28
2.21 Semiconducting Direct Particle Detection . . . . .	29
3.1 SENS C Series SiPM PDE . . . . .	31
3.2 Grid-run Scintillator Calibration . . . . .	35
3.3 Standard Deviation in Scintillator Calibration . . . . .	36
3.4 Geant4 SiPM Sim Scintillation Calibration Muons . . . . .	37
3.5 Geant4 SiPM Sim Scintillation Calibration Protons . . . . .	38
3.6 Regularity of Internal Reflection Trajectories within Cherenkov Radiator . . . . .	39
3.7 Geant4 SiPM Sim Cherenkov Radiation Calibration Protons . . . . .	40
3.8 Grid-run Cherenkov Calibration . . . . .	41
3.9 Standard Deviation in Cherenkov Calibration . . . . .	42
3.10 Line Run of single Cherenkov Paddle . . . . .	43
3.11 Line Run of single Cherenkov Paddle - processed photon count . . . . .	43
3.12 100m Asteroid Model . . . . .	46
3.13 Backscatter Setup . . . . .	49
3.14 Backscatter Differential Flux . . . . .	50
3.15 Backscatter Differential Flux: Charged Particles Only . . . . .	50
3.16 Backscatter Mean Kinetic Energy . . . . .	51
3.17 Backscatter Mean Charged Species Abundance . . . . .	52
3.18 Muon Calibration Count Rate . . . . .	53
3.19 Transmitted Muon Differential Flux . . . . .	54
3.20 Transmitted Muon Count Rate . . . . .	55
4.1 High Level Design Combinations . . . . .	66
4.2 High Level Design Data Collection Possibilities . . . . .	67
4.3 Global Instrument Model . . . . .	68
4.4 Generic Spacecraft Bus Model . . . . .	69
4.5 Mid level trade study Option 1A/2A Functional Model . . . . .	70
4.6 Mid level trade study Option 1B/2B Functional Model . . . . .	70



4.7 Mid level trade study Option 1C/2C Functional Model . . . . .	71
4.8 Mid level trade study Option 3A Functional Model . . . . .	71
4.9 Mid level trade study Option 3B Functional Model . . . . .	72
4.10 Mid level trade study Results . . . . .	73
4.11 Cherenkov Paddle Configuration . . . . .	75
4.12 Effect of Pitch/Yaw on MDE . . . . .	79
4.13 Effect of Pitch/Yaw on MIDP . . . . .	80
4.14 Effect of Pitch/Yaw on MDE and MIDP with medium Muon proportion . . . . .	81
4.15 Effect of Pitch/Yaw on MDE and MIDP with high Muon proportion . . . . .	81
4.16 Geometric Parameter Study Results 1 . . . . .	84
4.17 Geometric Parameter Study Results 1 . . . . .	85
4.18 Geometric Parameter Study Results 2 . . . . .	87
4.19 Geometric Parameter Study: Final Design . . . . .	88
5.1 Geant4 Scintillation Verification - Protons . . . . .	92
5.2 Geant4 Scintillation Verification - Muons . . . . .	93
5.3 Geant4 Cherenkov Verification - Protons . . . . .	94
5.4 Geant4 Cherenkov Verification - Electrons . . . . .	95
5.5 Incident Electron Deviation from Cherenkov Theory . . . . .	95
5.6 Incident Electron Deviation from Cherenkov Theory . . . . .	96
5.7 Geant4 Cherenkov Verification - Alpha Particles . . . . .	96
5.8 Number of Alpha-particle Secondaries . . . . .	97
5.9 Muon Differential Flux Comparison . . . . .	99
5.10 Simulated vs Scaled Muon Flux . . . . .	100
A.1 AHP Matrix . . . . .	108
B.1 Spherical Sector Area . . . . .	110
B.2 Reproduction of Figure 4.14 . . . . .	112
B.3 Reproduction of Figure 4.15 . . . . .	112
B.4 Final Integrated Study MDE vs. Altitude . . . . .	113

# List of Tables

2.1 Asteroid Types . . . . .	8
3.1 Correlation Coefficient Strength . . . . .	35
3.2 Cherenkov Calibration Sensitivities . . . . .	40
3.3 25143 Itokawa Regolith Minerology . . . . .	44
3.4 25143 Itokawa Regolith Elemental Mass Fractions . . . . .	45
4.1 Mission Assumptions . . . . .	56
4.2 Physics and Simulation Assumptions . . . . .	57
4.3 Detector Architecture Assumptions . . . . .	59
4.4 Photon Detecting Sensor Assumptions . . . . .	60
4.5 Electronics and Semiconductors Assumptions . . . . .	62
4.6 Spacecraft Design Assumptions . . . . .	63
4.7 Mid Level Trade off Design Options . . . . .	69
4.8 Mid Level Trade off Evaluation Criteria . . . . .	72
5.1 Single Particle Verification Tests . . . . .	91
5.2 Composition Comparison, NASA vs. Thesis . . . . .	98

# Nomenclature

## Abbreviations

AHP	Analytical Hierarchy Process
FFBD	Functional Flow Block Diagram
HDPE	High Density Polyethylene
IAU	International Astronomical Union
LEO	Low Earth Orbit
MDE	Muon Detection Efficiency
MIDP	Muon Identification Probability
NEA	Near Earth Asteroid
PDE	Photon Detection Efficiency
PDF	Probability Density Function
PMT	Photomultiplying Tube
PVT	Polyvinyl Toluene
QCD	Quantum Chromodynamics
SiPM	Silicon Photomultiplier
SMASS	Small Main-belt Asteroid Spectroscopic Survey
SPAD	Silicon Photon Avalanche Diode
SSSB	Small Solar System Body

## Symbols

$\alpha$	Fine Structures Constant
$\beta$	Particle Velocity Ratio $\frac{v_p}{c}$
$\delta_F$	Density (Fermi) Correction Term to Bethe Formula
$\gamma$	Lorentz Factor
$\lambda$	Wavelength
$\Omega$	Solid Angle [steradians]
$\phi_N$	Differential Flux of Incident GCR Primaries [ $m^{-2}sr^{-2}s^{-2}GeV^{-1}$ ]
$\rho_D$	Material Density [ $g/cm^3$ ]

$\theta$	Half Angle of Cherenkov Cone
$\theta_p$	Angle between $\overline{v_p}$ and $\overline{F_C}$
$A$	Mass Number
$a_p$	Orthogonal distance between electron and axis of $\overline{v_p}$
$A_{AVG}$	Mean Atomic Mass
$A_{SD}$	Area of Sensitive Detector Volume [ $m^2$ ]
$b_p$	Direct Pair Production Loss Integrant
$C$	Shell Correction Term to Bethe Formula (For Slow Particles)
$C_I$	Internal Energy Conversion Factor (Organic Scintillators)
$C_s$	Scintillation Efficiency Non-Linearity Correction Factor
$d_M$	decay length of a given meson [ $g/cm^3$ ]
$E_0$	Incident Energy of Particle [eV]
$E_I$	Ionization Energy of an Atom
$E_{\mu 0}$	Energy of Muon at Sea Level (Earth) [eV]
$E_{\mu}$	Energy of a Muon [eV]
$E_{p(n)}$	Mean energy of scintillation photons emitted by secondary (or ternary etc.) solute material (n)
$E_{photon}$	Photon Energy [eV]
$F_C$	Coulombic Force [N]
$f_{xy}$	Total quantum efficiency of transfer of excitation energy from solute Y to solute X
$h$	Planck's Constant = $1.23984193$ [ $eV/\mu m$ ]
$I_N$	Differential Intensity of GCR Primaries [ $\frac{nuclei}{m^2 \dots sr \cdot GeV}$ ]
$K(\omega)$	Conversion factor, energy to number of photons
$k_B$	Birks' Constant (material property of scintillators)
$m_e$	Mass of an Electron [Fundamental Unit, or eV]
$m_{\mu}$	Resting Mass of a Muon [eV]
$N_A$	Avagadro's Number
$n_e$	Number of Electrons in Medium
$N_S$	Number of photons emitted during Scintillation
$P_{\mu}$	Probability that muon survives from production until sea level (Earth Atmosphere)
$P_{\pi}$	Proportion of Incident Energy transferred to $\pi$ orbitals in Organic Scintillator

---

$q_e$	Total quantum efficiency of Fluorescence
$S$	Scintillating Efficiency [ $\frac{emittedenergy}{inputenergy}$ ]
$t_{run}$	Simulated Time [s]
$v_p$	Particle Velocity [m/s]
$X_0$	Bremsstrahlung Proportionality Constant
$Z$	Atomic Number
$Z_{AVG}$	Mean Atomic number
$c$	Speed of Light in Vacuum
$I$	Radiative Intensity [ $W/m^2$ ]
$n$	Refractive Index
$P$	Power Transmitted by Radiation [W]
$Q$	Total charge of a particle in units of 1 $q_e$
$T$	Ionization Energy Loss
$c$	speed of light [m/s]

# Introduction

Space... is expensive. It costs somewhere between \$10,000 and \$100,000 (USD) per kilogram to launch into Low Earth Orbit (LEO) according to a 2017 NASA report [76]. Averaged over a wide array of vehicles and missions, this amounts to a mean of around \$20,000 per kilogram. It is this, more than anything, that constrains the world of spaceflight to small, low-mass, spacecraft, and all of the associated structural, logistical, and, above all, *operational* headaches that subsequently space engineering. Propellant is generally the largest portion of mass in any non-stationary spacecraft, often accounting for more than three quarters of every gram launched into space.

What if, however, you *didn't* have to bring every last molecule of propellant with you? What, indeed, if you didn't even have to launch most of the structural mass of a spacecraft? What if you could acquire these resources *after* leaving the gaping maw of Earth's gravity well? The short answer is that one could expect enormous savings in launch cost; and that, in a nutshell, is the driving impetus behind the growing interest in so-called In Situ Resource Utilization as applied to Space. To quote the more popular phrase, such acquisition of raw materials aimed at furthering the goals of space exploration, is manifest in the burgeoning field of space mining.

Even in its infancy, the topics that can be categorized within the broad them of space mining are extremely varied. From mining the water resources in the shadowy edges of lunar craters for propellant and human consumption needs, to supporting deep space travel by establishing fuel stations in the Asteroid Belt, an explosion of interest, publications, and feasibility studies has erupted on this topic within the last decade or so. asteroids, it must be noted in particular, seem to capture the imagination of both researchers and public. Perhaps this is because of the fabled M-class asteroids like 16 Psyche, which is thought to be composed almost entirely of metal, including an estimated \$700 quintillion (USD) worth of precious metals like gold, platinum, and palladium [3]. Or perhaps it is simply because the Asteroid Belt is, at least for now, more legally open to commercial activity than the Moon or Mars [68]. Perhaps it is simply because asteroids provide a unique opportunity to kill two birds with one stone and prospect commercial exploitation of deep space minerals in cooperation with scientific missions to a little-explored, scientifically interesting, corner of the Solar System.

Indeed, asteroids, in addition to their prospective mineral bonanza, present a unique opportunity to look into the remote past of the Solar System itself. They are, according to current theory, composed of those remnants of planetesimals and dwarf planets that ultimately did not accrete into the larger planets that we coexist with today [15]. They are, therefore, most likely left-overs from the earliest days of planetary formation billions of years ago. To date, however, there have been only a handful of missions to such small solar system bodies, and the compositional data available for most asteroids is minimal at best, limited to what can be collected from remote spectroscopy performed from earth-based instruments [48].

This emerging confluence of growing commercial interest in asteroids, and the persistent lack of data that frustrates existing scientific interest, presents something of a unique opportunity. Such constructive interference between normally isolated communities virtually ensures that asteroids will be given an increasingly prominent spot in the list of exploration mission priorities in the coming years. Indeed, there are no fewer than five planned and en route asteroid missions on the books for the next decade, from both private and public sectors [2]. At the most basic level, the impetus behind *this* thesis project is to exploit this sweet spot of high interest in asteroids. It does this by proposing to fill a knowledge gap that has hereto forward plagued theoretical and modeling efforts of asteroid and planet formation: namely the fact that there is little or no directly available data regarding the interior of asteroids. Existing data on asteroids is almost exclusively linked to surface characteristics [15].

This project is partially inspired by a white paper written by Prettyman et al for NASA's Innovative Advanced Concepts program in 2014 that explores the possibility of applying muon tomography to the interior of asteroids [61]. Their simulations showed that the method itself is likely feasible, and could, critically, provide constraining data about the interior of asteroids that is needed to complete our understanding of asteroids themselves and their role in the formation of the Solar System. But, before moving forward, an obvious and excellent question arises: How do muons help us to understand the structure and composition of asteroid interiors?

The answer lies in some of the unique properties of muons themselves. Muons are leptons that exist with a charge of either positive or negative 1e. They are characterized by being around 100 times more massive than electrons and having a remarkably long average lifespan relative to similar massive exotic particles [36]. The large mass, combined with the characteristic leptonic lack of susceptibility to the weak atomic force lend muons a very low total interaction cross section with conventional matter. They can, in other words, penetrate solid rock to depths of several kilometers. Coupled with the fact that muons are common products of the hadronic showers of GCR primaries impacting conventional matter [47] (like Earth's atmosphere or asteroid regolith), muons make an excellent naturally occurring particle for use in radiography of massive, or very dense, structures otherwise impenetrable by more commonly used forms of radiation like x rays. They have been, for example, used to peer into the interior of an active volcano in Japan [70], and to probe shipping containers looking for heavy radioactive elements [52].

This thesis is aimed at the next logical step in the study of feasibility for this method applied upon an asteroid as proposed by Prettyman et al: investigating the practicable designs for a detector capable of collecting muon data for tomographic purposes in space.

## 1.1. Project Framework

### 1.1.1. Design Philosophy

While it is, perhaps, somewhat unusual to find a subsection dedicated to “design philosophy” in a technical thesis, it seems to be one of the more concise ways to define, and communicate, the scope of a project.

To wit: This project is, at its core, a feasibility study. For the purposes of best understanding the concrete definition of the project, it is useful to place “feasibility study” within the greater systems design construct. Engineering Design classically consists of a few well-agreed-upon chronological steps: Ideation and Trade off, Preliminary Design, Detail Design, Prototyping and Testing, and, finally, Production and Operation. The concept of “Feasibility Study” in this project was incorporated within this overall design chronology somewhere within the Ideation and Trade off phase. The quintessential question that must be answered in any such endeavor is: Is there a more or less operable design option that satisfies what broad general requirements may exist before starting (like launch vehicle restrictions or environmental requirements posted by ESA or NASA) and falls within constraints? A feasibility

study, therefore, is, in and of itself, something of a microcosm of the entire design process. It is a rough approximation of what may eventually become a final product. The fundamental underlying goal of a feasibility study is to generate objective evidence to answer the question of whether or not it is worth the time, effort, and money required to move on to the Preliminary Design phase.

And that is precisely the fundamental purpose of this project: to generate sufficient evidence to allow a reasonable conclusion as to whether or not it is possible and practical to employ muon-based tomography in a space environment, specifically in an Asteroid environment. The critical steps necessary to answer this query are to:

- Identify Boundary Conditions
  - Environmental
  - Technical
    - ◊ Probable Spacecraft Bus Characteristics
    - ◊ Reasonable Mass, Volume, and Power Budgets
    - ◊ Available Detection Technologies
- Identify Physical/Operational Design Parameters
  - Universal Design Parameters
  - Mutually Exclusive Design Parameters
- Synthesize bare minimum number of Parametric Models to cover all Design Parameters
- Perform Trade off Study on these Parametric Models
  - Identify Mission Success Criteria
  - Identify Total Mission Loss Criteria
  - Compare Parametric Models based upon Criteria
  - Rank / Eliminate Options
- Verify/Validate Model(s)
- Perform Application Study with best Design

If one peruses the general process outlined above, the resemblance, in miniature, to the overarching design process is clear.

For a number of reasons, it was most effective to undertake the general tenets of the feasibility study as defined above within an Systems Engineering framework; perhaps chief amongst said reasons is the high degree of ubiquity of such systems engineering application across the space industry. Thus, the steps of identifying boundary conditions becomes the step of making, documenting, and *justifying* simplifying assumptions. The identification of physical and operational design parameters merges with the identification of mission success and failure criteria to yield a formalized hierarchy of design requirements. The execution of the Trade Study remains distinct; evident in both perceptive variations of the feasibility-study process, as does the process of verification and validation. Finally, one may consider the direct analogue of the Application Study within the higher-level design process to be the prototyping and testing phase.

Why is it important to point out that the feasibility study process is simply a miniature of the overarching design process while also emphasizing the distinctions between them? Simply to make one point very clear: this project *does* include design activities, but the scope is *much* more limited than a full design process. A satisfactory product of this feasibility study is, therefore, a simple binary statement of whether or not a small, or micro, satellite-compatible sensor can be *practically* designed to collect particle radiation data of sufficient quality in orbit around an asteroid to yield useful tomographic mapping of that asteroid's interior. Unlike a full design project, no final design will be formally presented; though the final parametric model of the feasibility study may provide a useful foundation upon which future researchers may be able to base their true design process.

To this end, the assumptions and requirements development are treated concisely in the Design chapter. It is necessary to note that, as with many feasibility studies, full validation was not possible because it would have required the construction of a working prototype to



check the validity of the simulations. Thus, for the instrument itself, only verification was performed, wherein the fundamental physical building blocks of the model were tested; a process distinct from validation *only* in that the data and/or theory used for comparison is well established, peer reviewed, and publicly available. Validation, as defined in this context, is a far more specific comparison of a prototype with a simulation. At the end, some level of validation did prove possible when checking some of the final asteroid environment simulation results against results published in the aforementioned NASA Advanced Innovative Concepts white paper by Prettyman et al that explored the concept of asteroid muography with similar particle simulations [61]. These results, were *not* verified by specific data gathered in, and about, asteroid radiation environments, but they *are* an independent baseline published by a credible source. Thus, it was decided that the definition of validation discussed above, namely the requirement for specific, hard, corroborating data, could be relaxed a bit in this case.

### 1.1.2. Project Scope

Ultimately, it was necessary to apply the broad conceptual framework of this project, outlined in the previous sub-section on design philosophy, to draw clear boundaries around the project within which both simplifying assumptions and derived requirements could be written. To this end, this project was ultimately considered to consist of two main topics. The first topic, which dominated between 80-90% of the project timeline, was the exploration of feasible instrument design options through a number of trade off, and parametric, studies involving a number of analytical tools including (but not limited too): Analytical Hierarchy Process (AHP) design trade-off, and increasingly sophisticated particle simulation studies that gradually integrated more and more elements of "real-life" into their scope.

The second topic regarded the simulation of the expected environment, and associated boundary conditions, of an asteroid in the main Belt. The first topic, regarding the instrument design options, was myopically focused in on small details like geometric configurations and detection methods; the second topic, in almost direct opposition, required a far-broader look at what amounts to the entirety of the local space-environment, and all of the simplifying assumptions associated with treating something of such a relatively vast scope. Ultimately, the intensely opposing natures of many of the characteristics of these two main topics (not the least of which is the massive difference in scale!) lead them to be considered as two largely opposing conceptual "poles".

Investigating each one of these opposing "poles" of the project, by itself, was straightforward and relatively easy; the greatest difficulty of the entire thesis ultimately arose when trying to forge a connection between the two. Arguably, this attempt to forge a connection was only partially successful; and understanding the basis of that difficulty provides the context necessary to outline the clear project boundaries and limitations mentioned in the preceding paragraph. In the end this was simply as follows: simulation results from separate environment and instrument models could be retroactively considered in an analytical assessment of feasibility; but a joint simulation proved beyond the limited computational and time constraints of this project.

Ultimately however, this retroactive consideration of the combined implication of both separate project "poles" was deemed adequate. Thus, the largest remaining limitation of this project was the inability to perform physical testing on an instrument prototype to validate simulation results. Ultimately this limits the scale of conclusions: very specific quantitative conclusions are not justifiable with such unvalidated data; leaving, primarily, broad, qualitative conclusions to be drawn. The reader will see this theme mentioned often throughout the thesis. It reflects a painstaking self-audit performed to ensure that all conclusions drawn and logical steps taken were as well supported as possible, and, *critically* did not exceed either the project scope detailed here, or reasonable limits of deduction or induction. This can hardly be emphasized enough: most conclusions drawn are qualitative, not because of laziness or time crunch, but because more specific conclusions made without validating experimental

data are not justifiable, and ultimately not useful to any future researchers.

Ultimately, the best definition of the project scope lies in the formal constraint of the research questions.

### Research Questions

1. What radiation environment might a spacecraft encounter in any of the primary evaluation sites?
    - (a) What is the radiation environment at the Asteroid Belt / NEA ?
      - i. What are the characteristics of muon emissions that have traversed the thickness of said asteroid; as opposed to same-side muon generation in the surface regolith?
      - ii. Are there any other appreciable sources of muon emissions that may interfere with the detection of particles that directly penetrate the full asteroid?
      - iii. Will the other types of radiation present at the study site pose a risk of false detection and unusable data for the detector?
    - (b) Given these answers, what is the optimum target size and/or location for an asteroid subjected to muon tomography?
  2. What detection method(s) are best suited to a low-power, small form-factor, cheap, space-tolerant, hodoscopic detector design?
  3. What passive shielding/ active-filtration configuration will adequately allow for the selection of the targeted, penetrative, muons?
    - (a) What shielding (passive filtration) will best shield the detector from non-muon radiation with a minimum amount of mass?
    - (b) Is it possible to design a simple "active shielding" filtration algorithm that will enable the sorting of unwanted detection events from the desired muon radiation?
  4. What performance characteristics are necessary to allow the instrument to successfully detect muons in orbit around an asteroid, or emplaced upon the surface of one?
    - (a) What is the optimum field of view for a singular instrument in surveying a roughly spherical asteroid about which it is in orbit?
    - (b) What is the optimum pointing accuracy of the instrument?
- NOTE: Cherenkov detectors give inherent angular information without pixels.

# 2

## Background

### 2.1. Environment

#### 2.1.1. Asteroids

To begin, a discussion of the current knowledge regarding asteroids is warranted. It is, perhaps, useful to start this discourse with a clarification of terminology and classification; which, for asteroids, is complex.

Originally, small bodies discovered in the solar system which exhibited the same typical movement across the celestial sphere as the planets, were known interchangeably as either asteroids or planets. This was either in reference to their point-like appearance in the relatively primitive telescopes of the day, and because of their characteristic observable pattern of motion, "wandering" across the sky like the planets [28] [10]. The intervening years have yielded a comparative wealth of information about asteroids. They are hugely disparate in size, composition, orbital characteristics, and other factors; which makes classification difficult. By convention of the International Astronomical Union (IAU), solar system bodies are differentiated into sun, planet, dwarf planet, and everything else is lumped into the aforementioned category Small Solar System Bodies (SSSB) [20]. Within this last category, the general term "asteroid" refers to any body that is larger than 1m in diameter, smaller bodies are known as "meteoroids" [20].

Classically, asteroids were further categorized principally by their orbits. These families are still widely used, and include: Near Earth Objects (NEOs), the classical Asteroid Belt between the orbits of Mars and Jupiter, the Trojans which lie in the various stable Sun-Jupiter Lagrange points, and all objects that orbit further out which are lumped into the category "Trans Neptunian Objects." Further differentiation of this last category splits it into the Kuiper Belt, largely beyond the orbit of Pluto, and the Oort cloud located at the fringes of the solar system [25]. These major asteroid loci are shown in the following image:

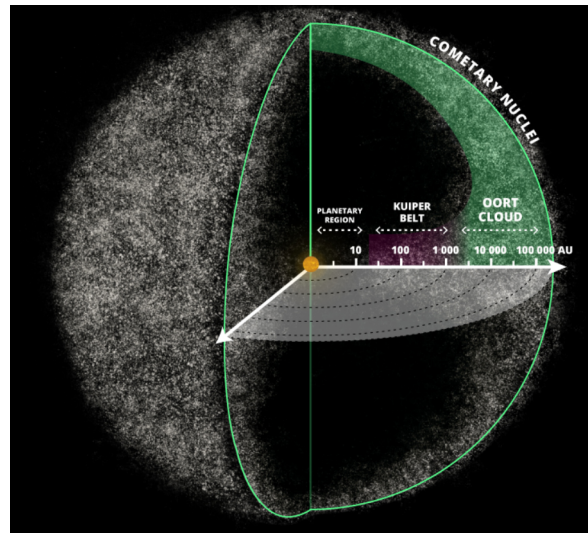


Image courtesy of <https://space-facts.com/oort-cloud/>

Figure 2.1: Illustration of relative scale of the outermost groups of Small Solar System Bodies: Kuiper Belt and Oort Cloud

For reasons of practicality and the low probability that any missions will visit the outermost collections of SSSBs located in the Kuiper Belt and Oort Cloud, most of the following discourse will focus upon NEOs and Asteroid Belt objects because of their much greater proximity. These collections of SSSBs are shown in the following image:

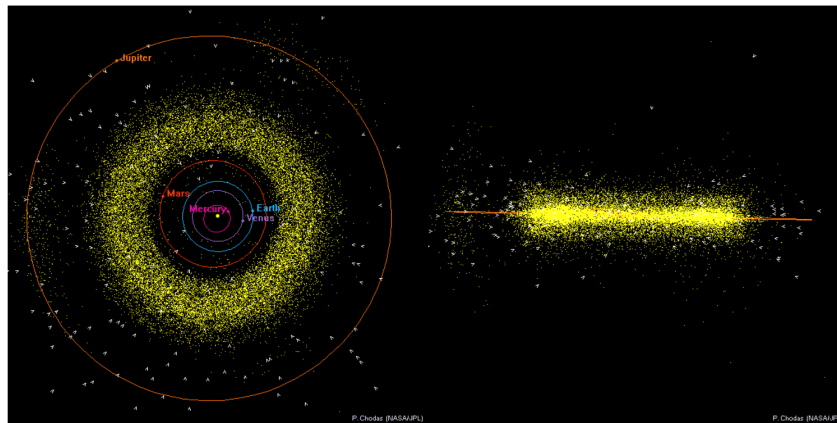


Image courtesy of NASA JPL

Figure 2.2: Illustration of relative scale and placement of inner groups of Small Solar System Bodies: Main Asteroid Belt and Trojan Asteroid Groups

For the purposes of surveying the practicability of muon tomography applied to asteroids, it is more useful to consider a categorization of SSSBs that relies more upon size and/or composition. No explicit nomenclature difference beyond the tacit asteroid/meteoroid dichotomy mentioned earlier exists to separate SSSBs based upon size, however, as the previously mentioned asteroid-muography white paper written by Prettyman et al states, the penetrative range of muons that are simultaneously high energy and of sufficient frequency of occurrence to be useful is somewhere around 1km [61]. This is size classification enough, and plenty of SSSBs of this size exist in both the main Asteroid Belt and close enough to Earth to merit classification as Near Earth Objects.

Compositional characterization is more useful, as the 1 km muon range previously mentioned is fairly dependent upon compositional characteristics like density and atomic mass of the constituent elements. Again, there is no formally standardized classification scheme, but one

that is both in common use, and of relevance to this project is the Small Main-Belt Asteroid Spectroscopic Survey (SMASS) taxonomy [24]. This classification is an expansion of an older taxonomy proposed by Chapman Morrison and Zellner in the 1970's, and builds upon their principle three asteroid classes. These basic categories are Carbonaceous (C-class), Metallic (M-class) and Siliceous (S-class). The SMASS system further differentiates these categories based upon spectral differences thusly:

Table 2.1: Spectral Classifications of Asteroids according to SMASS [24]

Primary Classification	Sub-Classification	Description
C	B C Cg Ch Cgh Cb	Bluer, higher albedo, more volatiles than C Common Carbonaceous Strong UV absorption feature around $0.7\mu\text{m}$ Transition between C and B
S	A Q R K L S Sa Sq Sr Sk Sl	Reddish, strong Olivine spectral feature Small but strong metallic spectral signal Reddish, High Albedo, small metallic signal Low Albedo, shallow $1\mu\text{m}$ absorption Similar to K, redder in visual spectrum Common Siliceous Transition Types
X	M E P Xc Xe Xk	Common Metallic (usually Fe Ni) High Albedo, Metallic Rich Minerals Very Low Albedo, non-metallic, organics-rich Transition Types
T	none	Unknown composition, possible C, P or D
D	none	Reddish, very low albedo, close to P
Ld	none	Transition Type
O	none	Rare, strong absorption feature $\lambda > 0.75\mu\text{m}$
V	none	High Albedo, mother body likely 4 Vesta

It is worth mentioning that another type of SSSB exists, namely comets; though it is, perhaps debatable whether these are all truly solar system bodies. These objects are characterized by the presence of a vapor trail and ionized coma as they travel through solar wind within the frost line. Many asteroids that orbit continually beyond the frost line show spectral evidence of volatile ices and other compounds that might indeed form a tail if the orbit was a bit closer to the sun [25]. Likewise, there are many asteroids which pass within the frost line on highly elliptical orbits, similar to the more famous examples of comets, which may have been comets at one point, but have now exhausted all volatile matter on their surfaces after many perihelion passages.

For the ultimate goal of understanding the structure of the interior of smaller asteroids with muon tomography, the hereto forward mentioned chemical composition is highly important, as a causal factor in the determination of material density. However, due to micro and macroporosity, the bulk density of an asteroid, even the generally denser M and S types, can vary across nearly an order of magnitude. This is demonstrated by the density estimates of several well known asteroids that are shown in the following figure:

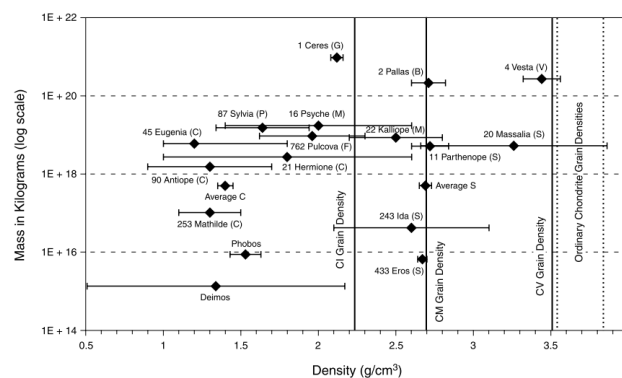


Image courtesy of Britt et al [22]

Figure 2.3: Estimated Density with error bars for a number of well-known asteroids

As is evidenced by the microporosity of a meteorite dissected after falling to Earth, even the bulk density of meteorites robust enough to withstand re-entry and impact are immensely dependent upon the macroscopic structure of the body itself [22]. The magnitude of the error bars in Figure 2.3, is, in and of itself, a decent quantitative justification for the application of muon tomography to asteroids. We simply do not know much about the internal structure of the asteroids.

While muon tomography is unlikely to achieve sufficient resolution to provide accurate characterization of microporosity, there is reason to suspect that the technique could easily supply information on macroporosity and bulk structure at the resolution of at least tens of meters (for instance, Tanaka et al's characterization of magma tube features of around this scale via muon tomography [45]). Also, though the relationship is highly non-linear, Prettyman et al's simulations suggest that the resolution achievable with muons increases as asteroid size decreases due to the larger number of low-energy muons able to penetrate smaller diameters [61]. It is useful, for the purpose of defining simulation boundary conditions and inputs to have a more in-depth survey of a specific asteroid, or representative set of asteroids. The morphology of three asteroids will be hereafter discussed. Each have been visited by spacecraft, and are within an order of magnitude the approximately 1km diameter muon range. Two, 25143 Itokawa and 4179 Toutatis, are quite similar "rubble pile" asteroids, and differ substantially in observable structure, and composition from the third, 2867 Steins.

### 25143 Itokawa and 4179 Toutatis Case Study

Both Itokawa and Toutatis are remarkably similar bi-lobal asteroids that are almost certainly of the rubble-pile morphology as theorized by Fujiwara and Huang respectively [31] [42]. Both asteroids are elongated, have a narrower neck near the center of the major axis, and exhibit fairly large surface aggregates (boulder sized), as opposed to the smoother regolith that is more common on larger asteroids like Eros. These asteroids can be seen below:

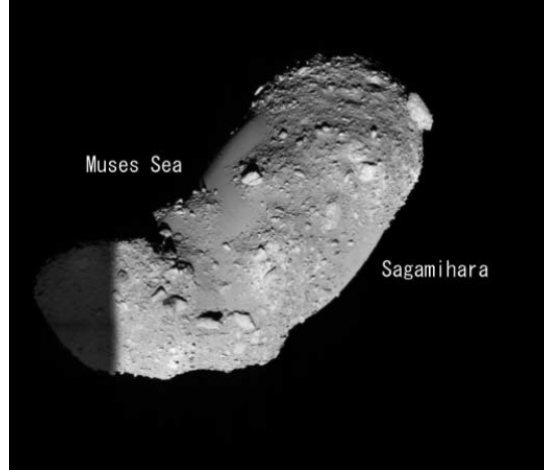


Image courtesy of Fujiwara et al [31]

Figure 2.4: Asteroid 25143 Itokawa, as imaged by the Hayabusa Spacecraft

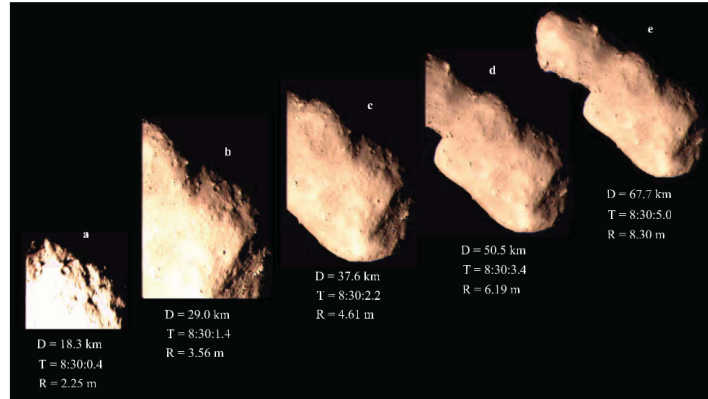


Image courtesy of Huang et al [42]

Figure 2.5: Asteroid 4179 Toutatis, as imaged by the Chang'e 2 Spacecraft

It is obvious from these true-color images that the mineralogy of these two asteroids is distinct. Further differences include: size, density, spectral classification (SMASS), and rotation period. Toutatis is an irregular ovoid of approximate dimensions  $4.75 \times 2.4 \times 1.95$  km; Itokawa has dimensions of  $535 \times 294 \times 209$  km. Toutatis has a bulk density of approximately  $2.1 \text{ g/cm}^3$ , while Itokawa has a bulk density of about  $1.9 \text{ g/cm}^3$ . Toutatis is an Sk class, and Itokawa is generally considered to be a Class S or Q, or some sub-class thereof. Toutatis rotates at an angular velocity of  $0.0356 \text{ rad/hr}$ , Itokawa rotates at the much faster rate of  $0.5235 \text{ rad/hr}$  [42] [31].

Of these characteristic parameters, the rotational rate of asteroids is worth delving a bit deeper into. This is primarily because general theory suggests that all asteroids larger than about 1 km in diameter are rubble piles. This is simply because the rotational velocity of larger asteroids are uniformly smaller than the angular velocity at which centripetal acceleration exceeds the micro-gravity that is thought to be the main cohesive force holding them

together[22]. While this is not conclusive evidence, other features observed on both Itokawa and Toutatis also support this theory.

Crater theory is probably amongst the two or three most important interpretive methods that exist for determining the structure of many asteroids. Asteroids are particularly important in the field of Planetary Sciences because they are thought to represent a glimpse into the major collision-accretion epoch of the solar system. It is not an exaggeration to state that the vast majority of formative phenomena of most asteroids in the last few billion years have probably been impactive [22].

Both Itokawa and Toutatis exhibit several large craters, and there is evidence of older craters that have been eroded by more recent impacts. The presence of several large boulders, and a relatively low amount of sub-centimeter regolith (on Itokawa especially) are indicative of high energy impacts that ejected smaller aggregate [31]. Taking this evidence of high-energy impacts together with classical fracture mechanics of brittle materials (like Siliceous Chondrites), it is evident that a solid asteroid would have shattered. The rubble-pile model is vastly more likely due to the energy-damping effect of shock waves propagating through loose rubble which allows such bodies to absorb far more punishment than solid fragments [15].

These observations yield a few conclusions about the practical application of muography: Firstly, the low bulk density of many asteroids is well suited to allow muon penetration (this even includes M class metallic asteroids, an excellent example of which is asteroid 16 Psyche which shows strong surface metallic spectrographic signatures, but has a bulk density of about  $4.5 \text{ g/cm}^3$ , considerably less than the granular density of its biggest constituent: iron [22]). Furthermore, the preponderance of these large, lumpy, rubble pile asteroids indicates a probability of large, relatively random, inclusions and abrupt changes in density throughout the interior of such asteroids. This would complicate tomographic efforts and likely increase the amount of time necessary to achieve a minimum resolution.

### Implications for Muography

Perhaps one of the more important implications of the various characteristics surveyed in the above case study is the fact that most asteroids rotate. The interaction of muons with the matter they traverse (which will be discussed in greater detail in the next sub-section), changes slightly when the particles of the transit medium are not at rest with respect to the velocity vector of the particle itself. However, for high energy particles especially, the the relative magnitude of the velocity of rotating asteroid particles is negligible compared to that of the incident primary particle. The more important effect of asteroid rotation relates to tomography. The combination of (strongly perturbed) orbital motion of the instrument must be coupled with sometimes highly irregular rotational dynamics when processing muon hit data. This is beyond the scope of this thesis.

Another major constraint of asteroid muography, as mentioned by Prettyman et al, is that the shape function of an asteroid is needed in order to calculate the average density along the trajectory of each detected particle [61]. The intersections of these 3D 'lines of average density' provide the basis of the technique of tomography [70]. If a rubble pile asteroid like Itokawa is used as the generic basis of comparison, the likely irregular distribution of relatively small inclusions may pose a problematic barrier to useful tomography. Namely that the resolution of the collected data may not be sufficient to differentiate the smaller constituent chunks that the asteroid is thought to be made of [31]. This is likely to yield a quantitative requirement on the minimum resolution required of any useful instrumentation scheme that will be investigated further in the execution of the thesis proper. Until then, it seems a reasonable first-order assumption to posit that any detector should be able to detect an inclusion equal in size to the largest verifiably singular boulder on Itokawa: the 50 meter boulder "Yoshinodai" found on the asteroid's western hemisphere (Itokawa was chosen as the basis of this assumption over Toutatis or Steins because it is the only asteroid surveyed herein that is within the size constraints imposed by muon range) [31].



### 2.1.2. Particle Radiation Theory

#### Primary Galactic Cosmic Rays

Primary Galactic Cosmic Rays are the principle source of muons in nature. While the origin of these highly relativistic particles is still in open debate (especially for the highest energy cosmic rays above  $10^{18} \text{ eV}$  which are thought to be extra-galactic in origin), most are thought to come from sources within the Milky Way galaxy [56]. There are a number of different particle types that are commonly seen in GCR primaries, including ionized nuclei of heavier elements. Generally, these rays consist of conventional matter, though positron and anti-proton rays have been known to occur in very low concentrations relative to their standard particle counterparts. Higher order anti-particles (like anti He nuclei) have never been observed though they are theoretically possible [56]. The relative abundance of several of the most common GCR primaries, represented as the differential intensity  $I_N$ , are shown in the following figure:

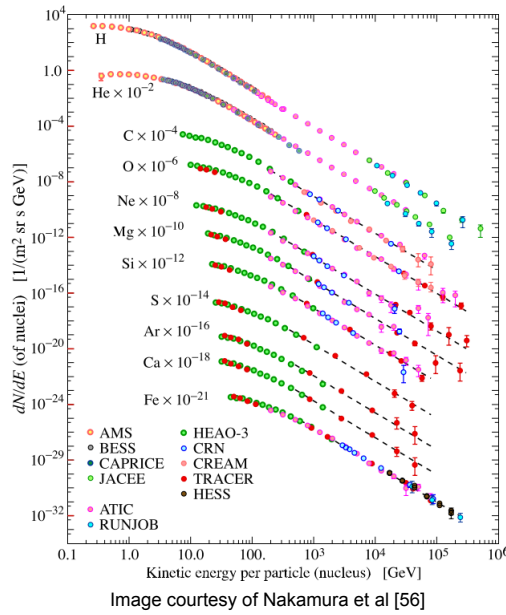


Figure 2.6: Intensity function for several of the most common GCR primaries over a large range of typically observed energies.

It should be noted that Figure 2.6 is a collation of a number of different data sources; these correspond to the differing data markers seen in each intensity curve. The single most important piece of information that can be gleaned from Figure 2.6 is the maximum flux:  $10^4 \text{ m}^{-2} \text{ sr}^{-1} \text{ s}^{-1} \text{ GeV}^{-1}$ . This is corroborated by Geisser [34]. With the CREME96 model used by SPENVIS, it is possible to generate a Geant4 macro that simulates the background GCR primary radiation expected anywhere in the Solar System [40][50]. This macro handles all of the species, energy-level, and trajectory probabilities that are implied in Figure 2.6, and require only a timing reference to properly simulate the differential GCR flux. This timing rate is normalized to the above-mentioned maximum differential flux rate.

As aforementioned, GCR primaries have a very nearly uniform incidence probability over the celestial sphere. The anomalies to this trend are generally thought to be caused by a few sources in the close-by galactic neighborhood, but represent deviations that are orders of magnitude less than the overall GCR flux observed on Earth [56]. It is reasonable to assume that any model that incorporates GCR primaries can be based upon the use of such a random spatial distribution, and a nucleus type / energy distribution based upon the spectra seen in Figure 2.6.

It is further necessary to mention that, since most GCRs are charged particles, they are influ-

enced, especially at lower energies by the cyclic variations in solar flux [17]. A semi-empirical GCR model incorporating this information was developed by Badhwar et al in 1996 that has been verified with experimental data collected over a number of space shuttle missions; the spectral energies predicted are within  $\pm 10\%$  of observed values. This variance is of limited relevance to this project, however, because at the orbital radius of the Asteroid Belt, the influence of the solar magnetic field is much reduced, this will be discussed in greater depth in a later subsection. Also, solar influence on GCR primaries is generally strongest for particles of low magnetic rigidity (lower energy primaries) which are of less interest for muography due to the correspondingly low energy of the muons produced when such primaries interact with matter [17].

Much of the remaining information with respect to GCRs relevant to muography refers to the secondary particles produced in hadronic showers after GCR primaries collide with a nuclei in some collection of matter. This will be discussed in a later subsection.

### Particle Interaction with Matter

The theory of the passage of particle radiation through matter is dominated by the discussion of energy losses of the particle as it transits; both scattering/ionization and radiative losses. While, theoretically, any of the four fundamental forces could influence the exchange of energy between a generic incident particle and the surrounding medium, gravity and the weak nuclear force are several orders of magnitude less powerful interactions than electromagnetic forces, which is itself about two orders of magnitude weaker than the strong nuclear force [1]. The strong nuclear force, however, is exceptionally limited in range, and does not act upon leptons like muons or electrons [36]. Thus, it is reasonable to state that the interaction of charged particle radiation and matter is dominated by electromagnetic effects across most commonly observed particle energies. The detection of neutrons, which are of course almost entirely charge-less is accomplished by indirect deduction from other phenomena. The most common neutron detection methods are absorption and elastic scattering [55]. The first tracks the quickly-decaying products that result from neutron capture in a nucleus, and the second relies upon tracking the electromagnetic effects of nucleus/atomic excitation from neutron collision that can result in ionization. Neutrinos are almost exclusively effected by influence of weak-force interactions; which makes them very nearly impossible to detect.

Beyond this general summary, however, this review of literature focuses primarily upon the physics of charged particles passing through matter because muons exist only in either a positive or negative charged state[34]. There are a few major mechanisms associated with charged particle radiation interaction with matter: scattering, ionization, and radiative losses [55]. Scattering, and more specifically the hadronic showers that give rise to muons, are discussed further in the next subsection. Ionizing and radiative losses will be briefly treated below:

Ionizing losses are described well by the Bethe equation, which relates the transfer of momentum from an incident ion to the surrounding atomic electrons. This can be considered to first order in a straightforward application of classical mechanics and Coulombs law. Consider the following situation:

Figure 2.7 shows a positive particle transiting through matter, and passing close to a bound electron in that matter. Through Coulombic interaction, some of the transiting particle's momentum is transferred to the electron. It is important to note that as the positive particle moves past the electron, the component of force exerted along the particle's velocity vector does not contribute to momentum transfer. If the velocity of the transiting particle relative to the electron is high (which it almost always is), then the push/push or pull/pull component of Coulombic attraction exerted along the velocity vector will cancel out. The direction of the Coulomb force, therefore, whether attractive or repulsive is not particularly important here. Therefore, it is primarily with the orthogonal component of the attractive force that one is interested [1]. That is:

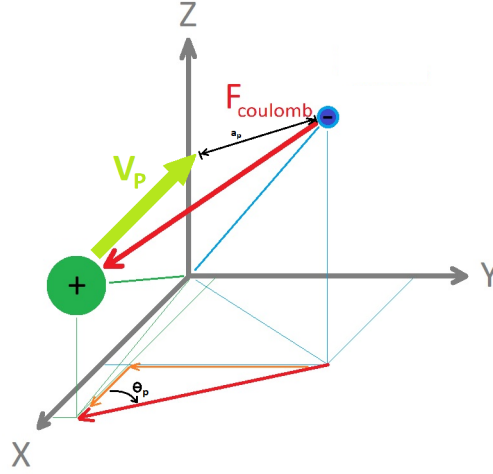


Figure 2.7: Illustration of charged particle passing close to a bound electron - Momentum Transfer

$$d\vec{p} = \overline{F_C} dt = \overline{F_C} \cdot \overline{v_p} dt = F_C v_p \cos(\theta_p) \quad (2.1)$$

Where  $\overline{F_C}$  is the Coulombic force,  $\overline{v_p}$  is the particle velocity, and  $\theta_p$  is the angle between the two. If one changes Equation 2.1 into terms of the cartesian reference frame, the equation becomes:

$$d\vec{p} = F_C \frac{a_p}{\sqrt{x^2 + a_p^2}} \frac{dx}{v_p} \quad (2.2)$$

Where  $a_p$  is the orthogonal distance between the electron and the axis of  $\overline{v_p}$ . If one then uses Coulomb's law to represent  $F_C$  in terms of electrical charge acting in a vacuum ( $F_C = \frac{1}{4\pi\epsilon_0} \frac{q_1 q_2}{\rho^3} \overline{\rho}$ ,  $\overline{\rho}$  = position vector from one particle to the other [37]), one arrives at the following:

$$d\vec{p} = \frac{Q q_e^2}{4\pi\epsilon_0 (x^2 + a_p^2)} \frac{a_p}{\sqrt{x^2 + a_p^2}} \frac{dx}{v_p} \quad (2.3)$$

Where  $Q$  is the total charge of the transiting particle as a multiple of the fundamental charge of an electron (+1 in the case of Figure 2.7). It is worth noting here that though the particle is transiting a medium (arguably the diametric opposite of vacuum), this derivation is based upon the subatomic scale where the macroscopic effects of a non-vacuum electrical permittivity ( $\epsilon$ ) do not occur, thus all of the equations included herein use the vacuum form of electrical permittivity:  $\epsilon_0$ . If one solves Equation 2.3 for the momentum transfer as the transiting particle travels from a very great distance from the electron to a very great distance from the electron, one obtains the following expression [1]:

$$|\vec{p}| = \left| \int_{-\infty}^{\infty} d\vec{p} \right| = \int_{-\infty}^{\infty} \frac{Q q_e^2}{4\pi(x^2 + a_p^2)} \frac{a_p}{\sqrt{x^2 + a_p^2}} \frac{dx}{v_p} = \frac{2Q\alpha\hbar c}{a_p v_p} \quad (2.4)$$

Where  $\hbar$  is the reduced Planck constant,  $\alpha$  is the so-called 'Fine Structure Constant' ( $\alpha = \frac{1}{4\pi\epsilon_0} \frac{q_e^2}{\hbar c}$ ), and  $c$ , of course, is the speed of light. There are a number of conventions with

respect to  $\alpha$  in particular which are confusing and not very well documented. In all of the remainder of this document, unless otherwise noted, the fundamental definition (above) will be used. Other definitions apply a basic scaling to values like  $\hbar$  and  $\epsilon_0$  for convenience such that  $\alpha = \frac{q_e^2}{4\pi}$ . This so-called "natural units" convention is very common in high energy physics, but, again, is somewhat misleading and poorly documented in the literature here surveyed [36].

Returning to the derivation, assuming the conservation of momentum and energy apply (all other losses are assumed to be negligible in this particular derivation), it is fairly simple to obtain the energy loss of the transiting particle from the transferred momentum [1].

$$T = \frac{1}{2m_e}p^2 = \frac{1}{2m_e}(m_e v_p)^2 = \frac{1}{2}m_e v_p^2 = \frac{2Q^2\alpha^2(c\hbar)^2}{a_p^2 v_p^2 m_e} \quad (2.5)$$

Where  $T$  is the energy transferred from the transiting particle to the electron, and  $m_e$  is the mass of an electron; the mass of the electron is used here because the momentum used ( $p$ ) refers to the momentum of the electron itself. To get the total (average) energy loss over the entire transit of the radiated particle, one must integrate the expression for  $T$  over all possible electrons within range:

$$dE = \int_{a_{max}}^{a_{min}} \int_0^{2\pi} T n_e d\phi a_p da_p dx = 4\pi n_e \frac{Q^2\alpha(c\hbar)^2}{v_p^2 m_e} \ln\left(\frac{a_{max}}{a_{min}}\right) dx \quad (2.6)$$

Here  $n_e$  is the number of electrons in the medium. Equation 2.6 essentially sums up all individual energy losses  $T$  within a minimum and maximum radial distance ( $a_{min}$  and  $a_{max}$ ) over all azimuthal angles ( $\phi$ ) about the particle's velocity vector ( $\vec{v}_p$ ). This is, in essence, summing up all energy losses over each infinitesimal distance traversed,  $dx$  within a corresponding infinitesimal volume  $d\phi a_p da_p$  (which corresponds to the canonical polar differential volume element  $rdrd\theta dz$ ).

The definition of the maximum and minimum radii  $a_{max}$  and  $a_{min}$  are based upon the radial distance at which the Coulombic force is no longer strong enough to affect electrons, and where the maximum amount of energy transfer occurs respectively. The maximum distance corresponds to where the transferred energy,  $T$ , can no longer overcome the basic excitation energy  $E_I$  of the atoms; that is to say, can no longer impart enough energy to ionize [1].

$$T_{min} = E_I = \frac{2Q^2\alpha^2(c\hbar)^2}{a_{max}^2 v_p^2 m_e} \quad (2.7a)$$

$$a_{max} = \left( \frac{2Q^2\alpha^2(c\hbar)^2}{v_p^2 m_e} \frac{1}{E_I} \right)^{1/2} \quad (2.7b)$$

Correspondingly, the minimum distance is where the maximum possible amount of energy is transferred, a direct nuclear collision. The specifics of this phenomenon are not derived here. However, the minimum radius is described in the following equations [37]:

$$T_{max} = 2\gamma^2 m_e \beta^2 c^2 = \frac{2Q^2\alpha^2(c\hbar)^2}{a_{min}^2 v_p^2 m_e} \quad (2.8a)$$

$$a_{min} = \left( \frac{2Q^2\alpha^2(c\hbar)^2}{m_e (\beta c)^2 2\gamma^2 m_e \beta^2 c^2} \right)^{1/2} \quad (2.8b)$$

Where the relation  $\beta = v_p/c$  was substituted into the denominator of Equation 2.8b. The term  $\gamma$  refers to the Lorentz factor used in relativity theory. When one divides Equation 2.7b by Equation 2.8b the following expression arises:

$$\frac{a_{max}}{a_{min}} = \left( \frac{2\gamma^2 \beta^2 c^2 m_e}{E_I} \right)^{1/2} \quad (2.9)$$

Substituting Equation 2.9 into Equation 2.6 yields the original formulation of the ionization loss relation as derived by Bohr [1]:

$$-\frac{dE}{dx} = 4\pi \frac{Q^2 \alpha^2 (c\hbar)^2}{\beta^2 c^2 m_e} \rho_D \frac{Z}{A} N_A \frac{1}{2} \ln \left( \frac{2\gamma^2 \beta^2 c^2 m_e}{E_I} \right) \quad (2.10)$$

Where  $\rho_D$  is the bulk density of the transit medium,  $Z$  is the number of protons in the nuclei of the transit medium (either absolute or average),  $A$  is the mass number (again, either absolute or average), and  $N_A$  is Avagadro's number; such that  $n_e = \rho_D \frac{Z}{A} N_A$ . This form of the equation is generally sufficient for lower energy particles of larger mass. It does not fit electrons well, and corrections are needed for both high energy particles and higher density media. To this end, Equation 2.10 was modified by a number of physicists including Fermi, Bloch, Bethe, etc. to adjust for quantum mechanical influences on this classical theory [1]. These additions are not derived here.

$$-\frac{dE}{dx} = 4\pi \frac{Q^2 \alpha^2 (c\hbar)^2}{\beta^2 c^2 m_e} \rho_D \frac{Z}{A} N_A \left[ \frac{1}{2} \ln \left( \frac{2\gamma^2 \beta^2 c^2 m_e T_{max}}{I^2} \right) - \beta^2 - \frac{\delta_F}{2} - \frac{C}{2} \right] \quad (2.11a)$$

$$-\frac{dE}{dx} = K \frac{Q^2}{\beta^2} \frac{Z}{A} \left[ \frac{1}{2} \ln \left( \frac{2\gamma^2 \beta^2 c^2 m_e T_{max}}{I^2} \right) - \beta^2 - \frac{\delta_F}{2} - \frac{C}{2} \right] \quad (2.11b)$$

Where  $\delta_D$  and  $C$  are the density and shell correction factors respectively. These are primarily dominant in the transit of either high or low energy particles respectively [1]. Equation 2.11a is the Bethe formula as cursorily derived in this report, while Equation 2.11b is a more canonical form where the factor  $K = \frac{4\pi q_e^2}{c^2 m_e} N_A$  is added to account for all of the constant terms in Equation 2.11a, and the entire equation is divided by  $\rho_D$  to normalize and give units of  $MeVcm^2/g$  [55].

Bethe's formula describes the interaction of particles with matter well in the range of approximately 10 MeV to 10 GeV; though this energy range varies greatly depending on particle type and transit medium properties. Also, the experimental results upon which the Bethe-formula is based are skewed by very rare high-energy-loss events; this makes it better to use a most-probable-energy loss formula [55]. This is a modified form of Equation 2.11:

$$\Delta p = \zeta \left[ \ln \frac{2\gamma^2 \beta^2 c^2 m_e}{I} + \ln \frac{\zeta}{I} + j - \beta^2 - \delta \right] \quad (2.12a)$$

$$\zeta = \left( \frac{K}{2} \right) \left( \frac{Z}{A} \right) Q^2 \left( \frac{x}{\beta a^2} \right) \quad (2.12b)$$

$$\int \frac{dE}{dx} = \frac{\Delta p}{x} \quad (2.12c)$$

$$j = 0.200 \quad (2.12d)$$

However, as previously mentioned, other, radiative, losses begin to become considerable at higher energies. The point at which ionizing losses equal radiative losses for a particular transit scenario is known as the *critical energy* [55]. This point is relevant to muons, and is shown graphically below:

According to Prettyman et al, muons in the range of energies from 1 GeV to 1000 GeV or higher are of interest in the survey of small asteroid interiors [61]. Thus, according to Figure 2.8,

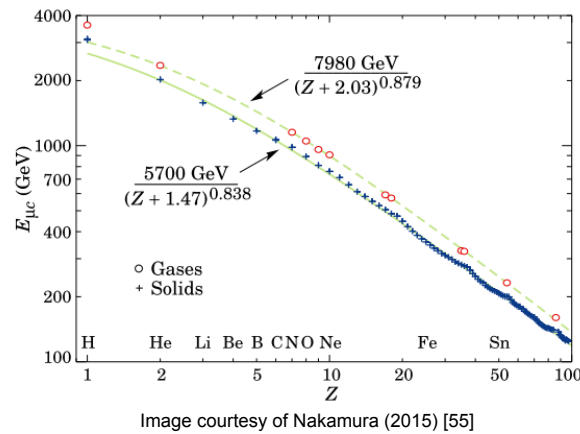


Figure 2.8: Critical Energy of Muons for several Atomic Numbers

muons traveling, for example, through a silicaceous asteroid have a critical energy of approximately 500 GeV. The primary radiative loss mechanisms are Bremsstrahlung, electron pair formation, Cherenkov radiation (under certain circumstances) and nuclear interactions. The first three will be briefly discussed herein, while Cherenkov radiation is discussed within the Simulation chapter.

It is, however, important to first consider the relative applicability of the various particle/matter interaction theories discussed in this literature review. The constraining factors in this discussion are the fact that it is anticipated that the model can be cleanly divided into detector and asteroid. The investigations surrounding the detector comprised the vast majority of the project, though the final part of the thesis involved simulations with asteroid models (compositionally based on 25143 Itokawa). For this reason, the constraints of the detector are assumed to be dominant, and can be used to discern the relative importance of various particle/matter interactions (and the corresponding depth of theory included herein).

The detector will, inevitably, consist of a very thin geometry (relative to the sometimes kilometers-long penetration range of higher energy muons through rock). This geometry will also likely be almost exclusively composed of relatively low  $Z$  compounds like glass, polymers, aluminum, etc. This includes shielding designed to excluded low energy particles.

The implications of these basic constraints, in conjunction with the most useful muon energy range proposed by Prettyman et al [61] (1-1000GeV) are that long-range energy loss models are not particularly relevant for detector physics, and that energy loss mechanisms associated with either very high energy muons (500 GeV +) are less relevant than models that describe the behavior of more common energies. . While the translation of these concepts into a useful design was a large part of the thesis, here they provide grounds for stating that the acceptable error in any measurement can be relatively high. These constraints indicate that for detector physics, ionizing/collisional energy is the dominant physical process, and that, aside from the potential use of Cherenkov Radiation as a detection scheme, other radiative losses can be neglected for verification purposes. The default physics list (a C++ object containing all relevant physical computation modules for a particular application) of Geant4 will still simulate any such events, but they will not be investigated further.

Because these losses for higher energy muons become very relevant when one considers the inverse modelling concentraion, where one models particle transport through the bulk of the asteroid itself, a brief description will be included of the physics behind these other, higher-order losses.

### Bremsstrahlung Losses

Bremsstrahlung is a phenomenon produced by the acceleration/deceleration of particles as they transit a number of opposing and offset electrical fields produced by the nuclei and electrons of the transit medium. While the theory of bremsstrahlung is very complex, a simple semi-empirical model exists that describes the basic theory adequately [1]:

$$-\frac{dE}{dx} = \frac{E_0}{X_0} \quad (2.13a)$$

$$\frac{1}{X_0} = \frac{4Z(Z+1)\alpha^3}{m_e^2} N_A \ln\left(\frac{183}{Z^{1/3}}\right) \quad (2.13b)$$

Where  $E_0$  refers to the initial energy of the particle and  $X_0$  is a proportionality constant.

### Direct Pair Production Losses

Pair production refers to the direction conversion of energy from high energy nuclear impact or interactions that results in the production of paired charged particles; one particle and its anti-particle. Most commonly this is the production of an electron and a positron due to the impact of another particle upon a nucleus, but can also result in the production of higher energy charged particle/antiparticles like muons, tau particles, pions, kaons, etc. [36]. A certain amount of momentum is transferred from an incident particle (either force-carrying particle or lepton/hadron) to an atomic nucleus that is relatively close to rest. The fundamental mass-energy equivalence theorem posited by Einstein then allows for the creation of particles from the energy released by the transiting particle if the energy exceeds the rest energy of the particle/anti-particle pair. Electron/positron pair production, for example, requires a transfer of energy of no less than 1.02 MeV to produce at-rest particles. Further energy is transferred to the produced pair in the form of momentum until the next threshold, for a heavier particle pair to be produced, is reached [36].

For the purposes of this review, it is deemed that a semi-empirical model based principally upon experimental results is most appropriate. Deeper treatment of direct pair production theory is not warranted because, as previously discussed, the critical energy for muons transiting siliceous rock (for example) is still in the range of several hundred GeV [55]; indicating that the bulk of muons suitable for muography lose most of their energy, in transit, via ionization.

Nevertheless, some treatment is necessary: the following equation describes the energy loss of muons (or any charged particle) due to direct pair production [35]:

$$-\frac{dE}{dx} = Eb_p(E) \quad (2.14)$$

Where the function  $b_p$  is the integral of the differential pair production cross section over the cylindrical volume of influence; the axis of which is the path of the transiting particle. This function, based upon the theory of Kel'ner and Kopov has been empirically curve fit by Wright for a muon transiting a standard isotope of siliceous rock ( $Z = 11$ ,  $A = 22$ ) [35]:

$$b_p = \begin{cases} 0.37 \ln\left(\frac{E_\mu}{m_\mu} - 0.95\right) \times 10^{-6} & E_\mu < 100 \text{ GeV} \\ 2.75 \left(\frac{\ln(E_\mu/m_\mu) - 5.43}{\ln(E_\mu/m_\mu) - 4.34}\right) \times 10^{-6} & 100 \leq E_\mu \leq 10000 \text{ GeV} \end{cases} \quad (2.15)$$

Where  $m_\mu$  and  $E_\mu$  are the rest mass and total energy of a muon respectively. This theory from Kel'ner and Kopov can be modified and curves fit for any transit medium, but it is deemed that the above semi-empirical direct pair production model is sufficient to provide first order qualitative validation of simulation results; that is to say, this provides a curve shape and an order of magnitude against which pair-production loss results calculated by a simulation tool can be compared for first order validation.

### Galactic Cosmic Ray - Secondary Particles

Theoretically, any particle, lepton or hadron, can be produced by either electromagnetic or hadronic cascades induced by the collision of GCR primary nuclei with other nuclei present in matter. This is an immense field of research that has spanned over a century, and is still rich with unexplored territory and experimental opportunity. This review will therefore be restricted solely to the the production of muons; particularly of higher energy muons.

Muons can be produced in either hadronic showers characterized by the collision of two nuclei, more commonly by the decay of the initial secondary particles produced by such a collision, or even by photon scattering processes like the previously mentioned pair-production. Hadronic scattering, particularly, is described by a very complicated set of theories captured under the umbrella of Quantum Chromodynamics (QCD) [34]. For all practical intents and purposes, this mechanism by which primary GCRs produce particle cascades, is beyond the scope of this project. This section will instead focus on the semi-empirical equations describing the energy spectrum of muons in the atmosphere. In addition, perhaps more importantly, the scaling of these transport equations used to describe particle cascades in the Earth's atmosphere to reflect particle cascades in other mediums (like asteroid regolith) will be discussed.

This problem will be considered from a practical perspective. This section will detail the hypothetical implementation of a simple simulation wherein muons are "injected" in a stochastic way that reflects the energy distribution and the event frequency of muons produced by the collision of GCR primaries with an asteroid.

Muon energy spectra are most commonly represented as a differential flux, or a differential intensity, of the form  $\frac{dN}{dE_\mu}$  with units of  $[\frac{\#particles}{cm^2 \cdot sr \cdot s \cdot eV}]$ . Sometimes the energy unit in the denominator is normalized to a momentum unit by dividing by the speed of light [12]. The physical manifestation of such an equation is literally the number of particles per unit energy (multiplied by constant detection parameters, area, solid angle, and time). It is evident that one could use such a relation ( $\frac{dN}{dE_\mu}$ ) in conjunction with a random number generator to develop a Monte-Carlo "muon-injector" for simulation. By integrating the differential muon flux, and making use of the fact that this integral flux in Earth's atmosphere displays a fairly typical normal distribution with non-trivial skewness [49], one could utilize a Gaussian random number generator with the aforementioned parameters to generate a random particle energy, then utilize the equation for the particle flux to inject the correct number of particles into the simulation. Because GCR primary incidence (and therefore muon generation) is a stochastic process with a fairly constant production rate in the time domain, one could base the random number generator solely upon particle energy distributions. One of the classic empirical formulae for  $\frac{dN}{dE_\mu}$  derived by Geisser his book on Cosmic Ray Physics in 1990 [34]:

$$\frac{dN}{dE_\mu} \approx 0.14E_\mu^{-2.7} \left( \frac{1}{1 + \frac{1.1E_\mu \cos(\theta)}{115\text{GeV}}} + \frac{0.054}{1 + \frac{1.1E_\mu \cos(\theta)}{850\text{GeV}}} \right) \quad (2.16)$$

Equation 2.16 was derived by convolving the production rates of the most common muon production channels, namely the decay of pions and kaons into a parameterized formula (pions represent the first term in parentheses, kaons the second); then fitting this formula to existing muon flux data like that from Allkofer et al [34][12]. This equation is valid primarily between muon energies of approximately 10 GeV and 1000 GeV, neglects energy losses and muon decay, and generates the following characteristic spectral curve [34]:



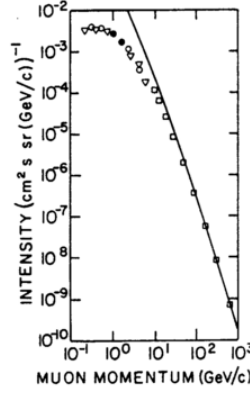


Image courtesy of Gaisser (1990) [34]

Figure 2.9: Flux of muons in Earth's atmosphere parameterized by energy. Solid line is the plot of Equation 2.16, data points show experimental data from multiple sources

When it becomes necessary to scale the production flux of muons to shower media other than Earth atmosphere, it is useful to utilize a form of Equation 2.16 as re-written by Prettyman et al [61]:

$$\frac{dN}{dE_{\mu_M}} \approx a E_{\mu}^k \left( \frac{A_M}{1 + (E_{\mu}/\epsilon_M)B_M} \right) \quad (2.17)$$

Where the subscript  $M$  represents one of the two primary mesonic parent particles present in cosmic ray particle showers that decay into muons (pions and kaons). Equation 2.17, therefore refers to just one of the terms in the parentheses of Equation 2.16. Prettyman makes use of the fact that the term  $E_{\mu}/\epsilon_M$  is related to the decay length of a meson  $d_M = \frac{E_M}{\epsilon_M}$ ; where  $E_M \approx E_{\mu}$  in this case because the primary muon-producing meson decay chains ( $K^{+/-} \rightarrow \mu^{+/-} + \nu_{\mu}$  and  $\pi^{+/-} \rightarrow \mu^{+/-} + \nu_{\mu}$ ) transfer almost all of the energy of the parent molecule to the vastly heavier muon instead of the associated neutrino [61][34]. The decay length is also defined as  $d_M = \rho_D \gamma c \tau_M$ ; where  $\rho_D$  is the transit medium density,  $\gamma$  is the Lorentz factor,  $\tau_M$  is the mean decay time of the parent particle, and  $c$  is, of course, the speed of light [61]. A cursory unit analysis shows that  $d_M$  has units of  $[g/cm^2]$  which is the conventional mode of discussing any kind of particle interaction length or depth due to its independence from the material properties of the transit material. When this decay length relation is substituted into Equation 2.16 or Equation 2.17 it is evident that it is the only term in either equation that has a dependency upon transit medium density  $\rho_D$ . Therefore, it is possible to scale the semi-empirical muon production differential flux shown in Equation 2.16 to any transit medium density just by substituting the appropriate  $\rho_D$  into the expression for the decay length of the parent particle,  $d_M$ . Prettyman et al performed evaluations of this technique by comparing various experimental and simulation results with this semi-analytical scaling approach with good agreement [61].

### 2.1.3. Radiation Environment

Cosmic rays have a statistically uniform probability of incidence across all possible directions in a spherical distribution of sources about the target point. However, they are also comparatively rare [17]. The incident flux of cosmic rays is roughly the same at any point in the known solar system (so far as we know) [17], but the number of subsequently generated muons differs greatly depending upon the medium through which the particle cascade occurs. On the surface of Earth, muons are observed with a fairly constant flux of at least 1 per square centimeter per minute [12]. It is estimated that the interaction of muons with the solid materials composing asteroids will yield transmissive muon fluxes nearly an order of magnitude less than this [61]. Furthermore, muography depends upon particles that are

transmitted through the bulk of the object; a non-trivial number of lower energy muons are generated and backscattered by cosmic rays incident upon the near surface of the object. Such lower-energy background radiation poses a significant design challenge to all spacecraft. GCR backscattering, as well as solar particles and trapped radiation fields, are highly dependent upon the particular environment experienced by the instrument in question. The two proposed environments for this project, LEO for initial instrument tests in a CubeSat, and the Asteroid Belt or a NEO as an ultimate goal, are considered hereafter:

### Asteroid Belt / Near Earth Object

Away from any planet with a significant magnetic field, the vast majority of the incident particle radiation is from either GCR primaries (discussed under section 2), or from solar particle radiation. Though some asteroids may pass close enough to Jupiter to experience non-trivial amounts of incident radiation from that planet, for the purposes of this review, such rare interactions will be neglected. Furthermore, radiation from latent trace radioactive elements present in the asteroid itself will be neglected.

Though there is still a considerable amount of solar weather incident at the average orbital radius of the asteroid belt (around 3-5 AU), the law of inverse squares intrinsic to the transmitted power of any isotropically radiated energy (like solar particle radiation) dictates that the incident radiative intensity is orders of magnitude less than that at Earth's average orbital radius. This is reflected in the following equation:

$$I = \frac{P}{4\pi r^2} \quad (2.18)$$

Where  $P$  represents the power transmitted by the radiation, and  $r$  represents the radius from the emitting source; in this case that source is the sun.

Asteroids within the main belt would experience an incident radiative intensity of somewhere between 4-11% that which hits the Earth. Near Earth Asteroids (NEA, alias Near Earth Objects) obviously experience an incident solar radiation intensity roughly equal to that of Earth.

Even considering the higher incident solar particle flux experienced by NEAs, most asteroids have very little magnetic field, if any at all. For example: 951 Gaspra, surveyed by the Galileo spacecraft in 1990, has a field strength approximately 25000 times less than that of Earth [72]. Therefore, few, if any, particles are trapped in close proximity to the asteroids, which further limits the local flux of incident particles that might be experienced by a spacecraft in orbit about such an asteroid.

Thus, by far the dominant radiation sources at an asteroid would be solar/GCR particle rays and their secondaries. The primary relevance of this fact is the lack of any natural absorption or shielding; Earth based instruments, or even those in LEO might experience lower fluxes of particles in some energy regions that allow for easier differentiation of recorded particle types. This will not be possible at any location in the Asteroid Belt.

To this end, more than simply muon fluxes will need to be simulated for instrument design evaluations. This simulation will make use of three non-muon particle sources: GCR primaries (with spherically even distribution), solar flux (approximate vectors coincident with solar nadir vector), and back-scattering off the closest asteroid surface from these two primary sources. A reasonable first order approximation of GCR backscattering (which would be dominant over solar particle backscattering at the distance of the asteroid belt) can be achieved by observing backscattering on the Lunar Surface. This is, in fact, an even better approximation for NEAs because of the similarity between orbital configurations of the moon and NEAs. A representative dose of all particles incident upon, and backscattered off, of lunar regolith is shown in the following figure:

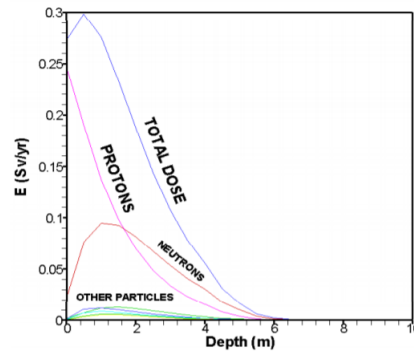


Image courtesy of De Angelis et al [26]

Figure 2.10: Lunar Surface Radiation dose: both backscattered and incident particles

For the purposes of simulation, De Angelis et al provide a model that could be used as a decent first order approximation of backscattered GCR secondary radiation off of asteroids. Ultimately, however, this may have to be included in more comprehensive GEANT4/GRAS simulations [26].

## 2.2. Detection Methods

### 2.2.1. Photon-based Particle Detectors

#### Scintillation

Scintillation refers to the phenomenon whereby some of the energy imparted to a particular type of medium by a transiting particle is absorbed by bound electrons and then re-emitted in the form of photons. Unlike Cherenkov radiation, this phenomenon is intrinsically linked to a very specific class of materials known (unsurprisingly) as scintillators. Useful scintillators are characterized by a few common traits[21]:

- Transparent to emitted photons
- Emitted photons within optimal sensitivity range of photomultipliers (either PMTs or SiPMs).
- Similar refractive index to glass for easy coupling with existing photomultiplier configurations.
- Fast decay rate of electron de-excitation to generate rapid, and easily distinguishable pulses
- Linearity in the relationship between emission intensity and incident particle energy.

The actual mechanism by which the scintillation photons are emitted is complex, and varies widely between different types of scintillating materials. There are, for instance, at least three major separate quantum mechanisms for the excitation and energetic decay of bound electrons in organic, inorganic, and (noble) gaseous scintillators respectively [19]. Because of the impracticality of maintaining an impermeable pressure volume for either gaseous or liquid scintillators on a CubeSat, only solid scintillators will be discussed in this review. Furthermore, as is described in detail in the assumptions section of the Design chapter, scintillators were used in several of the designs evaluated in this feasibility study, and organic scintillators were used in all such simulations.

## Overview of Organic Scintillation

Organic scintillators are almost all based upon aromatic compounds; specifically those with multiple joined aromatic rings. The particular mechanism for scintillation in such compounds revolves around the proliferation of pi-bond electrons in such benzene rings [21].

Benzene rings (and more complex molecules in which they are constituents) are characteristically non-saturated hydrocarbons with planar, trigonal, bonds. The non-saturated nature of such aromatic rings is critical to their scintillation effect because simple chemistry according to the theory of Lewis mandates the conservation of electrons between constituent parent species and any stable compound they then form [51]. Without going into the exhaustive description of this basic phenomenon, the accounting of electrons in aromatic rings results in exactly three double covalent bonds between carbon atoms in the molecule. This can be seen as follows:

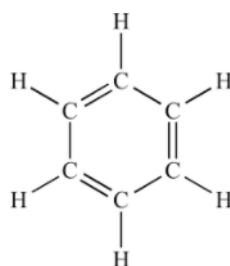


Image courtesy of UCLA ([http://www.chem.ucla.edu/harding/IGOC/B/benzene\\_ring.html](http://www.chem.ucla.edu/harding/IGOC/B/benzene_ring.html))

Figure 2.11: Static Covalent Bond Structure of Aromatic Ring

Quantum theory, however, tells us that these discrete double-bonds are not likely to occur in nature; these so-called "pi-bonds" (named thus because they are formed by electrons in the higher energy pi orbital) actually wind up existing as more of a cloud around the entire ring [21]. Thus, such aromatic molecules are more accurately represented as one of the following energetic configurations (lower positions in the figure indicates much higher probability):

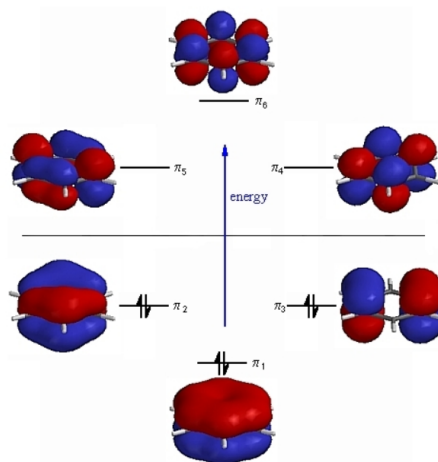


Image courtesy of University of Calgary (<http://www.chem.ucalgary.ca/courses/350/Carey5th/Ch11/ch11-4-1.html>)

Figure 2.12: Electron Cloud Representation of distributed pi-bonds in Aromatic Rings

The more time electrons spend distributed away from atomic nuclei, the less their ionization energy, in general [21]. This effect is increased to a great extent when multiple unsaturated aromatic rings are linked together as the constituent electrons are then spread out across all rings. This is particularly true of a particular class of molecules known as "linear-cata-condensed" hydrocarbons which include multiple benzene rings that essentially share one of their polygonal sides [21].

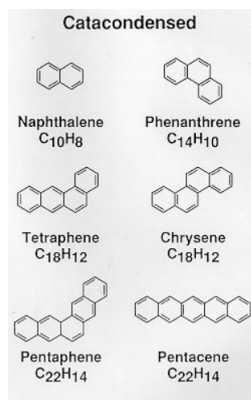


Image courtesy of Space Telescope Science Institute ([http://www.stsci.edu/lawton/research\\_dtmotivation.html](http://www.stsci.edu/lawton/research_dtmotivation.html))

Figure 2.13: Cata-condensed Aromatic Hydrocarbons

In particular, anthracene is a very efficient scintillator, and is generally used as a baseline against which all other organic scintillators are compared [21].

The actual scintillation mechanism is made possible by the large number of individual energy states possible for an electron in the pi-bond orbitals of such molecules. A basic treatment originally mentioned by Pratt in 1949 (and treated by Birks in his book, cited herein), models electron in each ring as a 1-dimensional circular oscillator. Said single dimension is the displacement around a circle of circumference sufficient to circumscribe the carbon vertices of the aromatic hexagon. Substituting this approximation into the Schrödinger equation and solving (the details of which were deemed beyond the scope of this review) yields a large number of discrete singlet and triplet electron energy levels [21]. A non-specific exemplar of such an energy distribution is shown below:

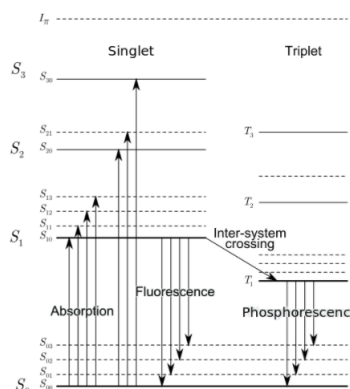


Image courtesy of Wikipedia.org ([https://en.wikipedia.org/wiki/Scintillation\\_physics](https://en.wikipedia.org/wiki/Scintillation_physics))

Figure 2.14: Typical Singlet and Triplet energy levels of an organic molecule that exhibits fluorescent properties

As can be seen on the diagram, electrons in these molecules undergo two primary processes, excitation (energy absorption) and de-excitation in the form of emission of photons and/or heat energy. In the terminology of Birks, fluorescence refers to near-instantaneous re-emission of light energy, while phosphorescence is usually a considerably slower photon emission [21]. While fluorescence is generally a process caused by incident photons exciting electrons which then re-emit photons at a lower energy, ionizing radiation passing through such compounds can cause a similar effect; this is scintillation. Scintillation in organic compounds usually exhibits a slow (phosphorescent) and a fast (fluorescent) component. The slow component causes the characteristic pulse-shape, which rises very rapidly due to the fast component, to trail off slowly. The fast component of scintillation is strongly correlated to particle mass (known as the ionization quenching effect); thus different incident particles

cause different pulse shapes which can be used for particle identification [21]. Any fluorescing compound, technically, can also be used as a scintillator, the useful scintillators, however, are those that comply with the aforementioned criteria [21].

### Cherenkov Detectors

As previously mentioned, Cherenkov radiation is a phenomenon that occurs when charged particles pass through a dielectric medium at a velocity that is greater than the local phase velocity of light. When any charged particle transverses thus, the local electromagnetic field of the medium becomes electrically polarized. Frank and Tamm were the first to describe the theory of this radiation with classical mechanics in 1937. Cherenkov cooperatively verified the results experimentally. The Cherenkov phenomenon will be discussed first followed by a cursory summary of Frank and Tamm's theory [30].

The Cherenkov effect is generally described by the analogy of a shockwave. Instead of propagating through air, a phenomenon very similar in characteristic shape and effect occurs when a charged particle passes through a dielectric substance at a velocity higher than the local phase velocity of light (in much the same way that an object traveling faster than the propagation speed of pressure waves in air will develop a sonic shockwave).

The qualitative description of this effect is based upon a description of the microscopic effects of a particles traverse of a dielectric media. Firstly, dielectric media are materials which do not conduct electricity (i.e. they have no free charge carriers), but their constituent *bound* charges can be polarized by an interacting electric field [62]. When a charged particle moves through such a medium, it carries with it a spherical electrical field which induces a polarity in the surrounding medium [30]. This is illustrated below in a plane coincident with the path vector of the moving particle:

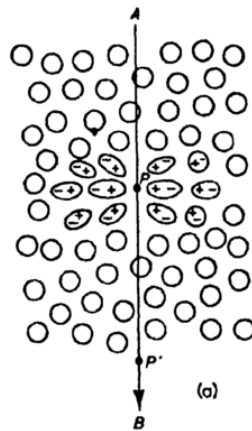


Image courtesy of Jelley (1958) [44]

Figure 2.15: Illustration of charged particle passing through a dielectric medium at relatively low velocity.

In this case, where the particle's velocity does not exceed the phase velocity of light within the medium, it is fairly easy to observe that there is a spherical symmetry of the polarization in the dielectric. This symmetry causes all net charge, when viewed from infinity, to be zero. However, when the particle's velocity is close to the local phase velocity, the dielectric bound dipoles (represented as blobs in Figure 2.15) begin to lag behind the particle in a characteristic conical shape [30]. This is illustrated below:

Without spherical symmetry in the polarization field any longer, it is evident that there is some net observable electrical field. When the bound dipoles relax into their unpolarized positions, the oscillation generates an electromagnetic wave. The defining characteristic of Cherenkov radiation is when the particle is traveling faster than a certain threshold velocity

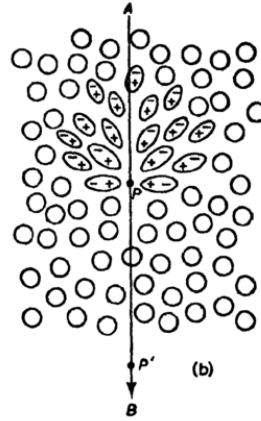


Image courtesy of Jelley (1958) [44]

Figure 2.16: Illustration of charged particle passing through a dielectric medium at relatively high velocity.

where the wavefronts that trail the particle near the apex of the cone begin to constructively interfere. This occurs when the particle in question exceeds the phase velocity of the dielectric medium [30].

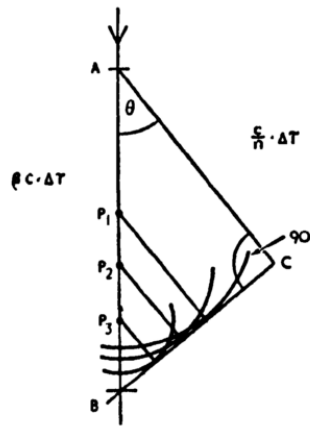


Image courtesy of Jelley (1958) [44]

Figure 2.17: Illustration of charged particle passing through a dielectric medium at the phase velocity of light within the medium

To be clear, there is no Cherenkov effect if the charged particle is traveling less than the threshold velocity. The empirical observations of the Cherenkov are ably described by a very simple relation:

$$\cos(\theta) = \frac{1}{\beta n} \quad (2.19)$$

Where  $\theta$  is the half angle of the "shockwave" cone,  $n$  is the refractive index of the medium, and  $\beta$  is the ratio of the particle's velocity to the speed of light:  $\beta = \frac{v_p}{c}$  [30]. The mathematics of the Cherenkov effect are discussed more in the Simulation chapter.

### Silicon Photo-multipliers

The basic operating principle of SiPMs is fundamentally similar to that of charged particle detection with semi-conductors discussed in the next section. An incident photon excites

an electron in the valence band of the semiconductor when it strikes, leaving an electron-hole pair. For energetic particles the magnitude of the charge induced is generally enough to provide a characterization of the particle in question with low amplification or none at all, however the fundamental concept of SiPMs is the detection of singular photons of relatively low energy. Thus, an additional signal amplification scheme is necessary.

Silicon Photomultipliers provide this amplification by inducing an electron cascade effect and channeling the ensuing charge through a diode to induce an output current [66].

More specifically, by applying a reverse voltage across a p-n junction (diode), an electric field is induced in the area of the detector where the photon creates an electron-hole pair. According to ?? this induces an acceleration of both the hole and the electron in opposite directions; corresponding to the opposite charges. The electron, of course, once a certain momentum has been imparted to it by the electric field, then begins to lose energy to the surrounding bound electrons according to Equation 2.11 (Bethe's Formula). Each subsequent electron-hole pair will subsequently be accelerated by the same externally sourced electric field, ionizing yet more electrons as they pass, resulting in a cascade of charge through the semiconductor. If this takes place with a diode in series (i.e. the p-n junction), then, just as in the case of charge transfer from a high energy particle to a similar junction, there is an appreciable current flow in one direction [66]. Such a device is known as a Silicon Photon Avalanche Photodiode (SPAD). A pulse is generated by limiting the amount of current traveling in a forward direction with a resistor in series; this creates a forward voltage according to Ohm's law ( $V = IR$ ), which reduces the perceived reverse voltage in the diode to below the break-down level; this is known as "quenching" [66]. SiPMs are simply a grid of a large number of microscopic SPADs. The characteristic shape of a SiPM pulse is illustrated below:

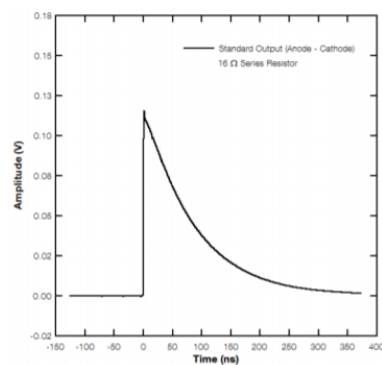


Image courtesy of SensL Technologies [66]

Figure 2.18: Characteristic pulse shape of a SiPM/SPAD when wired to only passive quenching circuitry

Better timing characteristics can be achieved with active circuitry designed to curtail the long decay tail evident in Figure 2.18 [66].

There are a number of relevant performance metrics that describe SiPMs including Photon Detection Efficiency (PDE), gain, response time (in conjunction with associated circuitry), and frequency response.

SiPMs, as previously mentioned, are an array of SPADS. This physically manifests as a checkerboard collection of microscopic squares etched into the semiconductor surface. There are, however, dark patches in-between SPAD squares that do not contribute to photon detection. Thus, quantum efficiency, the primary effectiveness metric for PMTs is not useful in describing the bulk SiPM response. SPADS can exhibit quantum efficiencies upwards of 80%, but generally exhibit overall PDE of closer to 40 %, making them comparable to PMTs in most cases [66]. This can be seen in the following graphic:

The PDE of SiPMs is inherently non-constant across different wavelengths. Most scintillators, and most Cherenkov radiation through conventional radiators ( $\eta \approx 1.5$ ) emit towards the blue



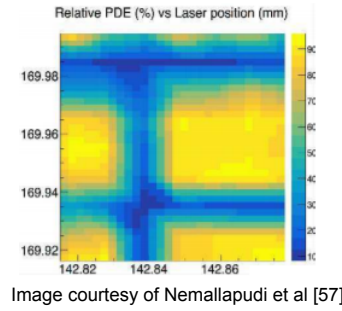


Figure 2.19: Differential PDE of the surface of a SiPM showing differences in Photon Detection Efficiency

end of the visual spectrum [21][44]. This is not exactly a natural coincidence, but caused by artificial selection of those scintillators and Cherenkov radiators most useful to human inquiry. Because of this, most SiPMs are optimized for a maximum PDE at somewhere around 420 nm [66][59]. A representative exemplar of this behavior is provided below[66]:

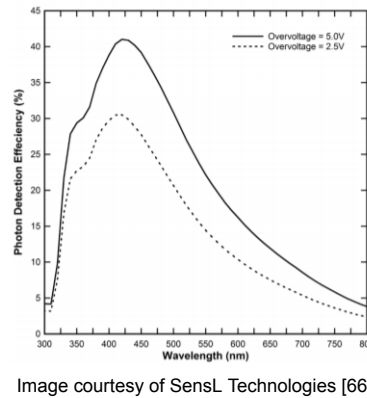


Figure 2.20: A characteristic example of the dependency of SiPM PDE on input frequency

This frequency response is characteristic of room-temperature behavior, and is a fairly average PDE for SiPMs across the two major manufacturers surveyed for this project[66] [59].

As a final note on SiPMs, there is not particularly meaningful outside the context of their associated circuitry. Most SiPMs are imbedded within a circuit that includes DC bias input, a signal discriminator, and an amplifier. This configuration, as described by Nemallapudi et al, offers an optimum performance in timing [57]. The conventional metric is known as Single-photon-time-resolution, and refers to the minimum time from photon incidence to discernible SiPM signal. Nemallapudi et al surveyed a number of commercially available SiPMs and reported a maximum response time of approximately 370 ps with a very low deviation approximately equal to 5 ps [57]. It is worth noting that utilizing a similar discriminator/amplification scheme could allow sufficiently fast response time with fast-scintillators or Cherenkov detectors to track time of flight for incident particles on a multi-layer hodoscope. This, indeed, proved to be a crucial piece of information in particle discrimination and will be discussed further in the Design chapter.

### 2.2.2. Semiconductor Detectors

Solid-state semi-conductor particle detectors work when a simple p-n junction is activated by the passage of an ion through the thickness of the junction. The low-band gap of semi-conductors (averaging a few eV for the most common Silicon variety) [38], makes ionization possible at very low energies. Ionized charge carriers (both electrons and electron holes) then transit to the cathode and anode of the junction, and generate a detectable current. This

phenomenon is illustrated below:

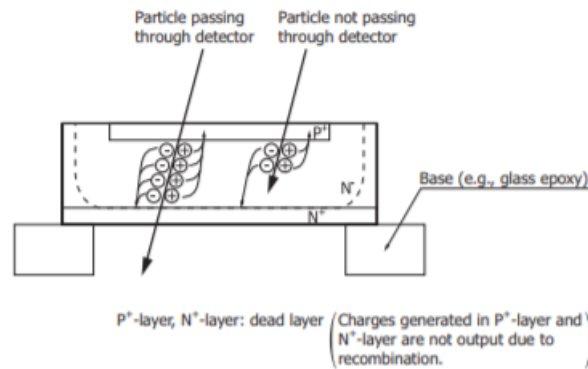


Image courtesy of Hamamatsu Photonics [38]

Figure 2.21: Single [ionizing] event effect detection of transiting charged particle radiation

These detectors are characterized by a relatively high molecular weight (and therefore stopping power), high granulation density, and a good energy resolution [54]. In other words, semiconductor particle detectors can fit a large number of pixels in a small space, and exhibit a much lower energy uncertainty than scintillators especially. Due to their low ionization energy, semiconductor detectors are commonly used for low to mid energy particle detections (ex. REPTile Instrument [64]), but present challenges for high energy particle detection.

The charge output of a particle detection event is close to proportional to the deposited energy in most cases [54]; the underlying detection mechanism is therefore best described as calorimetry. To measure the entire energy of a particle, both the rate of energy loss ( $\frac{dE}{dx}$ ) and the total extinction energy must be measured. This means that the particle must be stopped within the semiconductor junction itself [38]. For muons (or most other high energy particles) this obviously presents an essentially unassailable barrier to energy measurement [39]; they will not be stopped by anything short of a semiconductor a few meters thick in most cases. Thus, the particularly useful data that can be generated with this type of detector is energy deposition rate, positional information, and charge magnitude.

From the perspective of instrumentation specifically aimed at muons, this available data represents limited utility. Firstly, muon charge does not affect the penetrative range in matter [55]. Also, optical detectors (like SiPMs) also exist with excellent granularity down to, and below,  $1\text{mm}^2$  pixel size [65]. The rate of energy deposition remains a possibly interesting application, however. Simply put, a major defining characteristic of muons are the fact that they are simultaneously high energy but exhibit a very low energy deposition rate due to their weak interactions with matter. This poses a possible active filtration method whereby particles of similar energy (i.e. GCR primaries or secondary mesons etc.) could be easily discriminated from the target muon signal. Full evaluation this utility will likely be best accomplished during or after the principle design trade study (part of the thesis itself).

# Simulation

The fundamental core of the set of tools used to undertake this thesis project is the Monte Carlo Particle Transport code used to simulate all radiation effects upon the instrument. In this case, a code by the name of Geant4, developed and maintained by CERN, was chosen [13]. Geant4 is essentially a very in depth C++ library with which the user can conglomerate any number of the underlying objects or modules into a vast variety of applications. In this case, both the particle radiation simulation and the modeling of the instrument were undertaken in Geant4. It should be noted an application that was written using Geant4 C++ libraries, SPENVIS, was also used to poll CREME96 GCR data to develop spectrum inputs for GCR background particle sources. SPENVIS was created, and is maintained, by ESA [40].

## 3.1. Instrument Simulation

Geant4 provides support for complex geometry import via the creation of so-called "GDML" files [8]. There are parallel tools that can translate common 3D CAD file types into such input files. However, this functionality was not used to model the instrument. All surveyed instrument design options used rectangular prisms for their basic shape. This was partially done intentionally to simplify modeling, but this simplistic modeling paradigm nevertheless deviates only a very small amount from the design of detectors used for similar high energy particle studies, like CREAM [11]. The main reason that the models were implemented directly using Geant4 elementary volumetric shape libraries was because of the inherently greater flexibility for the variation of basic dimensional and material parameters. It is possible, for instance, to change no more than 5 lines of code within the Geant4-based parametric model and achieve a completely different geometry. This easy, and easily automated, geometric update flexibility was ultimately used for a parametric study of many potential final instrument designs where the major design themes (like detector type, system function, etc.) were kept the same, but parameters like overall length, the number of layers, and the aspect ratio of the frontal (square) width to the overall length, were changed methodically to converge upon a more optimal solution. The simulations undertaken to obtain metrics for comparison in this parametric study are described later on in this chapter.

### 3.1.1. SiPM Simulation

Because this instrument is constrained to a small satellite form factor, with the associated restrictive power constraints [75], there is effectively no alternative to the use of Silicon Photomultipliers (SiPMs) for very-low-light photon detection (the main alternative, Photomultiplying Tubes (PMT) require kilovolt-level power supplies [29]). It would, therefore, be necessary to subject any model of SiPM to space environment qualification tests. While such testing would almost certainly eliminate certain models of SiPM, it is beyond the scope of the study.

For this project, SiPMs were sourced from SENSIL inc. primarily because the company provides a great deal more data on their products than other surveyed manufacturers, but also because they offer a vastly simplified small-quantity purchase option that could prove advantageous for any future experimental developments made on this research topic.

The behavior of the SiPMs, used to detect either scintillation or Cherenkov photons, is critical to generate even a rough understanding of realistic instrument behavior. A large variety of physical parameters, design characteristics, and operational factors contribute to the efficiency of commercial SiPMs. For the sake of the project time-line, it was assumed that all of these parameters are invariant, or close to manufacturer-specified operating optimum, with the exception of the photon detection efficiency (PDE). This is primarily because the particles to which the instrument will be exposed, namely GCR primaries and resulting secondary particles like muons, are very high energy. Such particles yield comparatively high photon counts that are easily detectable, which obviates any need to expend analytical time on an SiPM trade off.

The SENSIL C-series SiPM was chosen due to favorable photon detection efficiencies in the 450-350nm wavelengths of light emitted by most organic scintillators [21], and characteristic of the most commonly emitted wavelengths of Cherenkov light [44]. The PDE for the SensIL C-Series is shown below, plotted for wavelengths in the visible light spectrum:

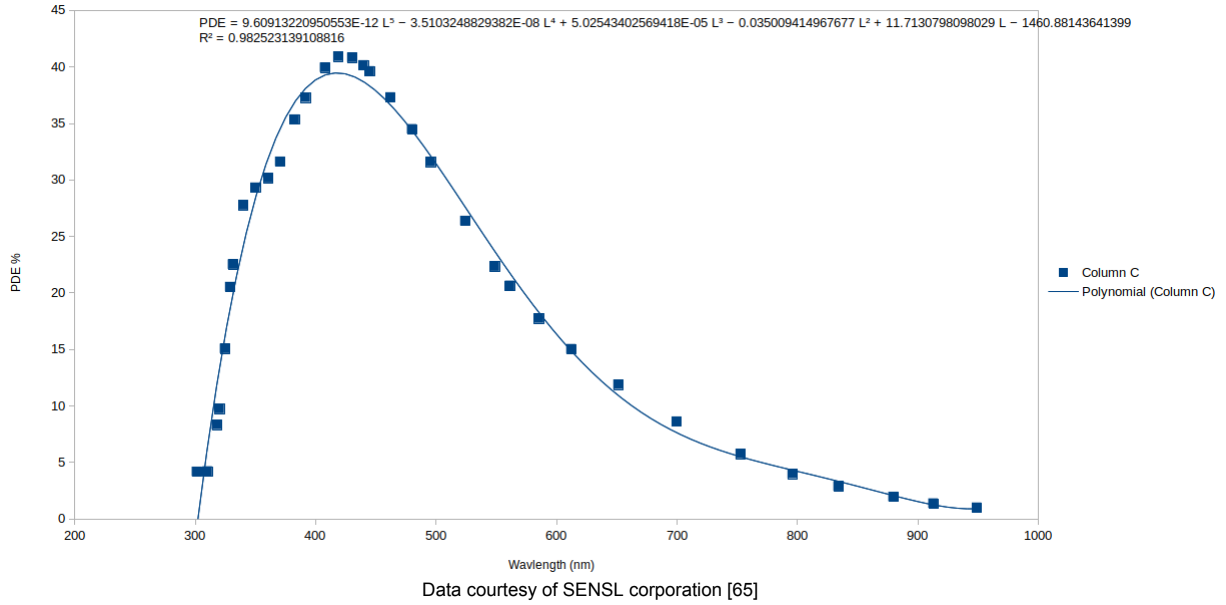


Figure 3.1: Photon Detection Efficiency for C-series SENSIL Silicon Photomultiplier

The blue points with square markers represent the PDE data series provided by SENSIL. For simulation purposes, the PDE was interpolated with a 5th degree polynomial using the least-squares interpolation algorithm built into Microsoft Excel 2010. This polynomial can be seen below:

$$\text{PDE} = 9.609E - 12\lambda^5 - 3.51032E - 8\lambda^4 + 5.0254E - 5\lambda^3 - 3.5009E - 2\lambda^2 + 11.71308\lambda - 1460.881 \quad (3.1)$$

Where  $\lambda$  is the wavelength in nanometers. The interpolation has a coefficient of determination ( $R^2$ ) of 0.9825, which corresponded to an overall average uncertainty of 8.04%. This error was largely due to a small secondary peak in the SENSIL PDE data at around 350nm that was not captured in the polynomial, but was deemed negligible in light of the fact that crosstalk and after-pulsing errors of the C-series SiPM ranged from 3-10% [65]. As neither of these physical phenomena were modeled, the overall error level from the polynomial model used

to simulate of the SiPM detector elements in Geant4 (i.e. excluding circuitry) remains about the same.

The implementation of this polynomial PDE model within Geant4 was based upon the behavior observed during scintillator and Cherenkov radiator calibrations discussed in a later section of this chapter. Specifically, particles were fired at either a monolithic block of scintillator material or a similarly monolithic Cherenkov radiator, and an internal physics module within Geant4 generated and propagated optical photons, according to the associated physical laws, within the volume of the respective block. The specifics of the radiative and optical mechanisms are discussed further in a later section. The purpose of this calibration was simultaneously to verify the proper function of Geant4's scintillation and Cherenkov radiation processes, and also to replace the extremely computationally expensive propagation of tens of thousands of optical photons generated in a single high-energy primary particle strike with a far more efficient empirical model of the number of recorded photon hits on the SiPMs. Ultimately, this took the form of an empirical function which took the deposition energy of the incident particle as an input argument and provided the total number of detected photons averaged over all of the SiPMs attached to the respective scintillator or Cherenkov radiator.

The SiPM PDE was folded into this total-photon count function by inserting the polynomial model into the scintillation and Cherenkov calibration scripts, written with Geant4; where it became part of the overall behavior of the empirical photon-count function which generated a final number of detected photons during simulations, based upon primary particle hit parameters. Within the calibration runs, the PDE was treated as the probability that one photon, of a certain energy, would be detected. The PDE is generally less than 50% because SiPMs consist of grid arrays of Single Photon Avalanche Photodiodes (SPADs), with dead space between the active areas of each microcell [66]. The detection efficiency of each SPAD is quite high even for singular photons, often on the order of 90% or more; thus the dominating factor in PDE is simply the probability of actually hitting an active SPAD area [57].

Thus, each optical photon hit upon the SiPM sensitive detector volumes was polled for its energy, then the energy was converted to wavelength with the following equation [36]:

$$E_{\text{photon}} = \frac{hc}{\lambda} = \frac{1.23984193}{\lambda(\mu\text{m})} \quad (3.2)$$

Where  $h$  is Planck's constant ( $1.23984193\text{eV}/\mu\text{m}$ ), and  $c$  is the speed of light. Equation 3.1 is then used to extract the PDE for the specific photon's energy. A pseudo random number generator, seeded by the time and date at the beginning of each particle hit event, was then used to produce a random number between 0 and 1 to six significant figures. If the number was less than or equal to the PDE, the photon interaction with the sensitive detector (SD) volume was recorded as a hit, discarded if not. The total processed photon count was then the sum of all the recorded hits. To validate this photon count model for use in future simulations that dispensed with Geant4's optical-photon transport modules for computational expediency, the photon count was divided by the total number of photons generated for each event and the result compared with the integral of the PDE function. The difference between the final photon-count function written in Geant4 and the published PDE was less than 1%.

### 3.1.2. Scintillation Simulation

As with the Cherenkov phenomenon, it is critical to understand how many photons are produced by transiting particles in scintillating detectors. Birks suggests a fairly simple semi-empirical model that should be sufficient for this review. Namely, the number of photons produced per any unit length is directly proportional to the scintillating efficiency,  $S$  [21]:

$$N_S = SK(\omega)C_s \int_0^x \left(\frac{dE}{dx}\right)dx \quad (3.3)$$

Where  $N_s$  is the number of photons emitted over a unit length  $x$ ,  $K(\omega)$  is a conversion factor to change between units of transferred energy to emitted photons,  $C_s$  is a correction factor for non-linearities that occur for higher ionization densities (generally occurring with heavier particles), and the integral is the total amount of energy transferred from particle to surrounding medium over a unit length  $x$ .

Birk suggests the following semi-empirical models for  $S$ , describing binary and ternary organic solutions respectively (which constitute most commonly used plastic or liquid scintillators) [21].

$$S_{binary} = P_\pi C_I \frac{E_{py}}{E_{1x}} f_{xy} q_e \quad (3.4a)$$

$$S_{ternary} = P_\pi C_I \frac{E_{pz}}{E_{1x}} f_{xy} f_{yz} q_e \quad (3.4b)$$

Where  $P_\pi$  is the percentage of energy transferred from the transiting particle to the pi orbitals of the scintillator molecules,  $C_I$  is the internal energy conversion efficiency detailing the transformation of excitation energy to electron energy (generally  $\approx \frac{2}{3}$  [21]),  $E_{p(n)}$  is the mean energy of scintillation photons emitted by solute (n),  $f_{xy}$  is the total quantum efficiency of transfer of excitation energy from solute Y to solute X, and  $q_e$  is the total quantum energy of fluorescence. In practice, it is generally easiest to derive these various terms experimentally, or to simply derive the scintillation efficiency itself without concentrating on its constituent factors [21]. One other term in Equation 3.3 remains,  $C_s$ , the correction factor for high ionization density particle interactions (i.e. heavy GCR ion nuclei like iron) where scintillation linearity breaks down. Birks presents (yet) another semi-empirical model for this non-linearity as follows [21]:

$$C_s = \frac{\frac{dL}{dx}}{1 + k_B \frac{dE}{dx}} \quad (3.5)$$

Where  $\frac{dL}{dx} = SC_s$  is the overall change in light yield (which can have many units including number of photons) per unit transit length,  $\frac{dE}{dx}$  is, of course, the particle energy loss per unit transit length, and  $k_B$  is known as "Birks' constant" and is an experimentally derived material constant particular to individual scintillators [21]. The scintillator used for this study was based upon Saint Gobain Crystals BC408 [6].

One further note to make upon organic scintillators is that, because their scintillation mechanism is inherently based upon single-molecule dynamics, they will continue to scintillate in different phases and solutions, unlike inorganic scintillators. Certain solutes, like polystyrene based plastics, can actually enhance energy transfer from transiting particles to scintillating molecules [21].

The behavior of Geant4's scintillation module, within the customized Physics List used for Cherenkov effect and Scintillation calibration [8], was tested within the scope of the parametric instrument model in some detail. The physics list itself was customized only in that a few extra modules were added to the default physics list to handle optical photon transport, which was otherwise excluded.

The number of photons generated by even one hit from a GCR proton of middling energy (for example 10GeV) can exceed tens of thousands per centimeter of scintillator traversed by the incoming particle. Both Birk's law [21], and the performance of the scintillation mechanism built into Geant4, yield this result. With increasing incident particle energy and flux rates, it rapidly becomes wildly computationally inefficient to track each individual photon generated

by scintillation. Scintillation response was, therefore, ultimately modeled by Birk's law instead in full detector simulations (vis. calibration simulations were far more limited in scope: one particle type/energy at a time was fired at just one type of detector).

The instrument, however, is neither a perfect detector of photons, nor are the external surfaces of the scintillator totally covered with detectors; far from it in fact. There are just 4 SiPMs placed in the center of the short side of each monolithic photon generating layer (in this case, scintillating layer) with a sensitive area of 5mmX5mm each. These monolithic photon-generating layers are modeled to exhibit a large probability of internal reflection when photons interact with volume boundaries, as if the block was covered in a reflective coating or covering like foil. This drastically increases the probability of photons striking the SiPMs, but at the relatively low numbers of photons generated, it was not clear whether the SiPMs would yield a uniform pulse response for off-center particle strikes. Therefore, several trials were made where one quadrant of the square scintillator block was subjected to protons fired one by one on a grid pattern encompassing the whole quadrant. Because the Geant4 scintillation mechanism itself is already well validated for a variety of particle species [13] [73], this was done only with protons for simplicity.

A number of such grid simulations were run over a logarithmic energy scale stretching evenly from  $10^0 - 10^4$  MeV. These first trials were run at a fairly low grid resolution of 4X4 impinging particles per quadrant to cut down on the run-time at higher particle energies (one 10GeV proton fired at the scintillator, for example, generates enough photon tracks to require approximately 60-100s of runtime on the ACER E5-575G-75MD laptop used for this particular part of the study with 8GB RAM, 4 cores, and multi-threading). A number of metrics were generated within the Geant4 model including: total number of photon trajectories per grid point, total number of hits to the SiPM sensitive detector volumes per grid point, the total number of processed SiPM hits per grid point, as well as the total number of hits and the number of processed hits for each individual SiPM. The resulting data can be seen plotted in Figure 3.2:

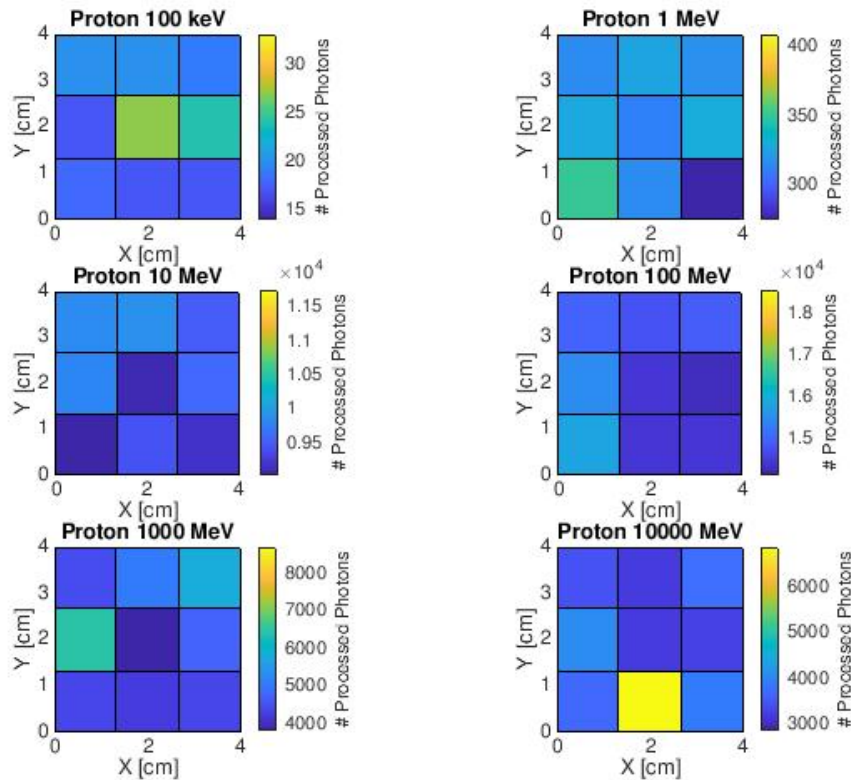


Figure 3.2: Colorimetric plots of total processed photon count for a range of incident proton energies fired at 1 quadrant of the total scintillator block on a 4X4cm grid subdivided by 4 nodes per side

The primary questions behind this sub-investigation were: Is the total SiPM response for a foil-wrapped monolithic scintillation counting block dependent on where the incident particle hits the scintillator volume? Secondly, is there a correlation between the impact coordinates and the magnitude of photon-count response for each individual SiPM?

The first question was evaluated by computing the standard deviation of the raw number of SiPM hits, and the total number of hits a real SiPM was expected to pick up (processed hits) for every grid point. The standard deviation of the photon count was taken to be equal to the absolute uncertainty of the count itself. This uncertainty varied little with incident particle energy. To quantify this low variance, the correlation coefficient between the energy and the uncertainty in photon count was computed. A semi-qualitative standard was adopted for final evaluation of correlation factors from a publication on the United States National Institute for Health database [53]. This was used because the semi-qualitative interpretation of correlation factors that it provides is the closest to a standard that was found in the (admittedly brief) part of the literature survey dedicated to this branch of statistics:

Table 3.1: Qualitative Categories of Correlation Coefficient Strength

Correlation Coefficient	Strength
0.0-0.3	negligible correlation
0.3-0.5	low correlation
0.5-0.7	moderate correlation
0.7-0.9	high correlation
0.9-1.0	very high correlation



The correlation between incident particle energy and the uncertainty in the photon count was  $-0.096$ ; very weak; the negative sign indicates that this slight correlation is inverse (i.e. when one variable increases the other decreases in some fashion). However, it is obvious, from the following plot, that there is some non-stochastic mechanism behind the behavior of the magnitude of the uncertainty in photon count.

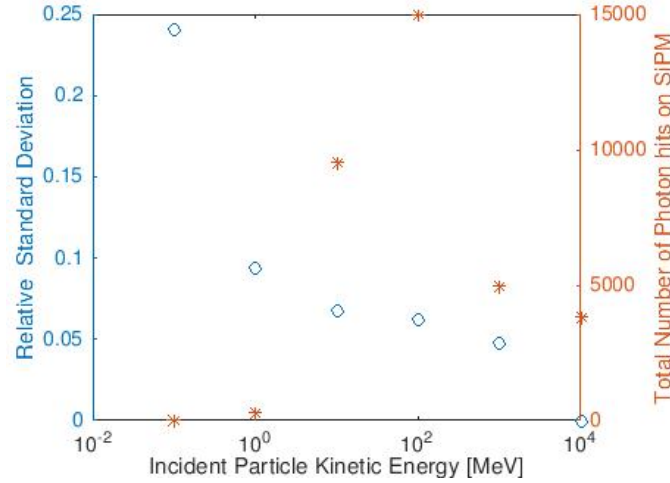
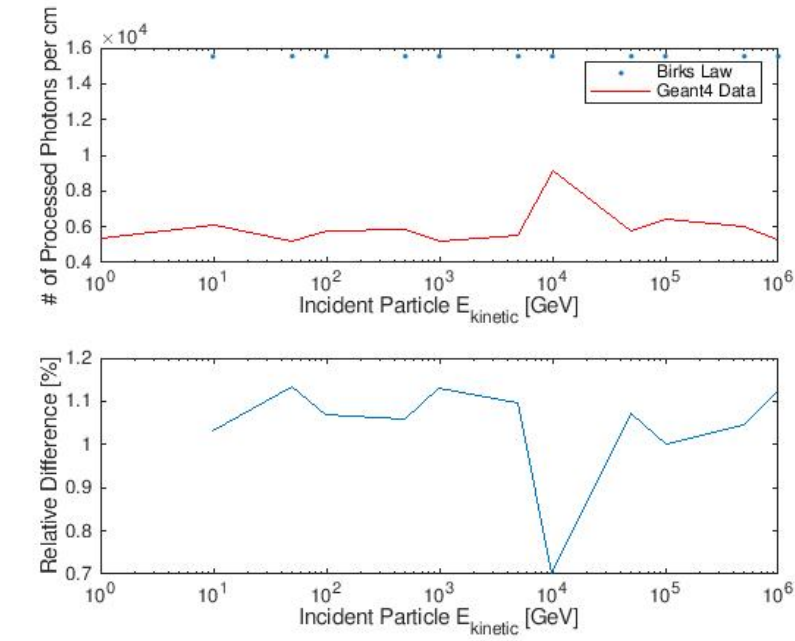


Figure 3.3: Relative magnitude of standard deviation in Scintillator Grid Calibration Runs

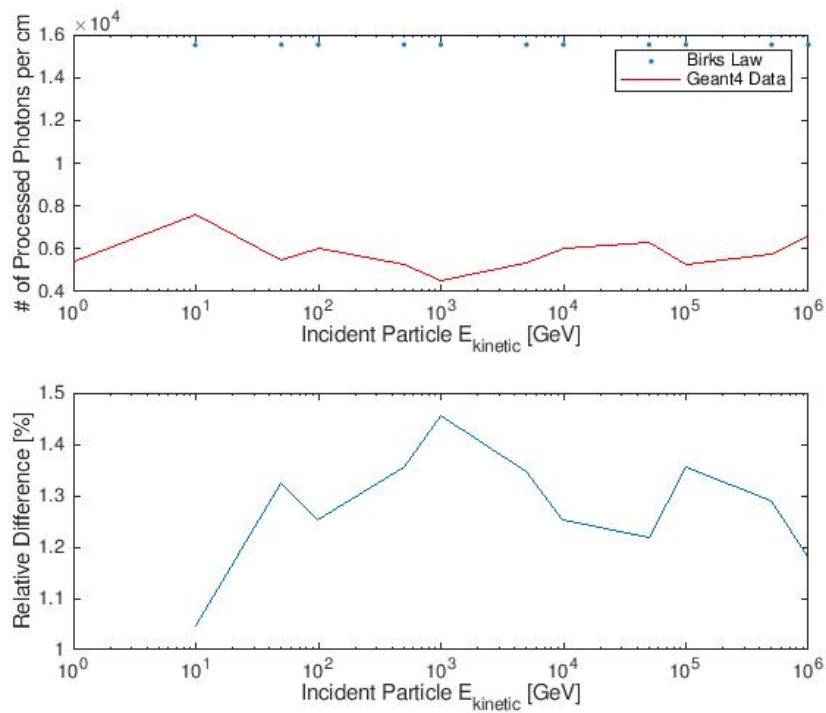
The most obvious non-stochastic mechanism would be that the magnitude of the relative standard deviation is a function of the population size it represents; in other words, larger numbers of photons should even out spikes in the probability density function caused by outliers, and lower the relative standard deviation as the distribution approaches a gaussian standard. To evaluate this hypothesis, the correlation was calculated between the total photon count and the standard deviation therein, and, as expected, a moderately strong correlation of  $-0.6641$  resulted.

Though this middling correlation may also hide other parameters that affect the overall count uncertainty, it is evident that the maximum uncertainty in the standard deviation is fairly low, averaging  $4.61\%$ . This allows a reasonable conclusion that the number of photon hits generated by an off-center strike is fairly independent of strike location on the scintillator. For completeness, this mean uncertainty was added to the overall signal uncertainty computations.

The average number of *processed* photons was  $63.17\%$  less than the prediction of Birk's law, with an uncertainty of  $4.17\%$  without the aforementioned outlier data-point caused by a nuclear interaction. The same was done for positive muons with a sensitivity of  $62.5\%$  less than the prediction of Birk's law, and an uncertainty of  $8.51\%$ . This is shown in Figure 3.4:



(a) Negative Muon Strike



(b) Positive Muon Strike

Figure 3.4: Sensitivity of simulated SiPMs to negative muon strike (left) and positive muon strike (right).

Finally, the same was done for protons yielding a sensitivity of -64.35% with an uncertainty of 4.83%. The data for these runs is plotted in Figure 3.5:

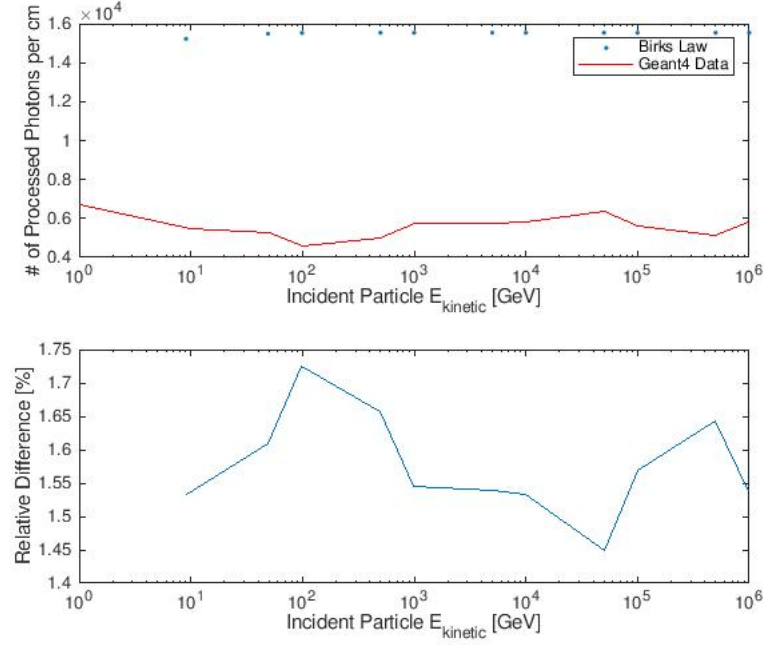


Figure 3.5: Sensitivity of simulated SiPMs to proton strike.

Ultimately, the sensitivities and uncertainties were averaged to yield a sensitivity of  $-0.6334$  and an uncertainty of  $\pm 5.8367\%$ . This sensitivity was used, in concert with the Birk's law model, to convert energy deposition to the number of processed scintillation photons for all further simulations involving scintillation.

Based upon the results in this section, it is reasonable to conclude that these fundamental building blocks of all further instrumentation studies are sound and physically reasonable. There are some uncertainties which add up to an approximately 11% total when added in quadrature.

### 3.1.3. Cherenkov Simulation

A relatively simple relationship between the number of Cherenkov photons emitted per unit pathlength over a given wavelength range is given below. This was taken from the Particle Data Group's publication on particle interaction with matter [55]:

$$\frac{d^2N}{dx d\lambda} = \frac{2\pi\alpha Z^2}{\lambda^2} \left(1 - \frac{1}{\beta^2 n^2}\right) \quad (3.6)$$

Where  $n$  is the refractive index, and is assumed to be constant over the wavelength ( $\lambda$ ) range where the SENSE SiPMs (C-series) are most effective:  $300\text{nm} < \lambda < 1000\text{nm}$  [65].  $N$  is the number of photons per incident charged particle,  $Z$  is the charge of said particle,  $\alpha$  is the fine structures constant, and  $\beta$  is the ratio of particle velocity to the speed of light.

Integrating this equation twice yields a useful expression for estimating the number of Cherenkov photons generated by a charged particle traversing a dielectric radiator block; which was ultimately used for simulations of the effect within the model itself for computational efficiency; again, this is opposed to the computational power needed to generate and track each individual photon, as discussed in the previous section on the verification of Scintillation simulation

physics.

$$\int_{\lambda_{IR}}^{\lambda_{UV}} \int_0^l \frac{d^2N}{dx d\lambda} = N = \int_{\lambda_{IR}}^{\lambda_{UV}} \int_0^l \frac{2\pi\alpha Z^2}{\lambda^2} \left(1 - \frac{1}{\beta^2 n^2}\right) dx d\lambda \quad (3.7a)$$

$$N = \int_{\lambda_{IR}}^{\lambda_{UV}} \frac{2\pi\alpha l Z^2}{\lambda^2} \left(1 - \frac{1}{\beta^2 n^2}\right) d\lambda \quad (3.7b)$$

$$N = 2\pi\alpha l Z^2 \left(1 - \frac{1}{\beta^2 n^2}\right) \left(\frac{1}{\lambda_{IR}} - \frac{1}{\lambda_{UV}}\right) \quad (3.7c)$$

$$N = 2\pi\alpha l Z^2 \sin^2(\theta) \left(\frac{1}{\lambda_{IR}} - \frac{1}{\lambda_{UV}}\right) \quad (3.7d)$$

Where  $l$  is the total length (or depth if you will) of the Cherenkov radiator, and  $\theta$  is the half angle of the Cherenkov "photon shock cone." This makes use of the fact that  $\cos(\theta) = \frac{1}{\beta n}$  [55].

A very similar study to that performed to calibrate the number of detected photons for the specific scintillator geometry was also performed for a similar Cherenkov counter. A number of high kinetic energy protons were fired at a model-standard 10x10x1cm monolithic borosilicate-glass Cherenkov radiator; with the strike arranged in a grid pattern over one quadrant of the radiator prism itself.

A phenomenon of note in the verification of the simulated Cherenkov effect: since the angles of photons with respect to the trajectory of the incident particle are not randomly aligned (as with scintillation), the incident protons were fired in at a very slight angle to avoid an internal reflection pattern of the type evident in the following figure:

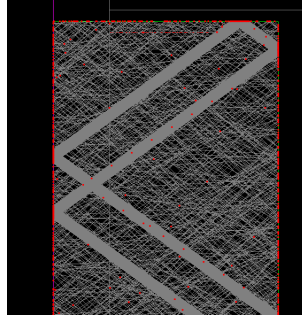


Figure 3.6: Regularity of Internal Reflection Trajectories within Cherenkov Radiator

This highly regular bounce pattern of photons reflecting within the Cherenkov radiator layer lead to about half the number of optical photons reaching each SiPM than for the fully-randomized scintillation photon trajectories. This represents the lower bound of the aforementioned geometry-specific calibration factor that was determined for each cherenkov or scintillator geometry used in a design study. The upper bound was achieved with fully random optical photon trajectories. Because of essentially unavoidable imperfections in the reflective surfaces of real-life Cherenkov or Scintillation layers, the upper-bound on the number of photons detected is almost certainly the number that would be observed in real life. The following figure (Figure 3.7) shows this much lower detected photon count observed for Cherenkov photons graphically:

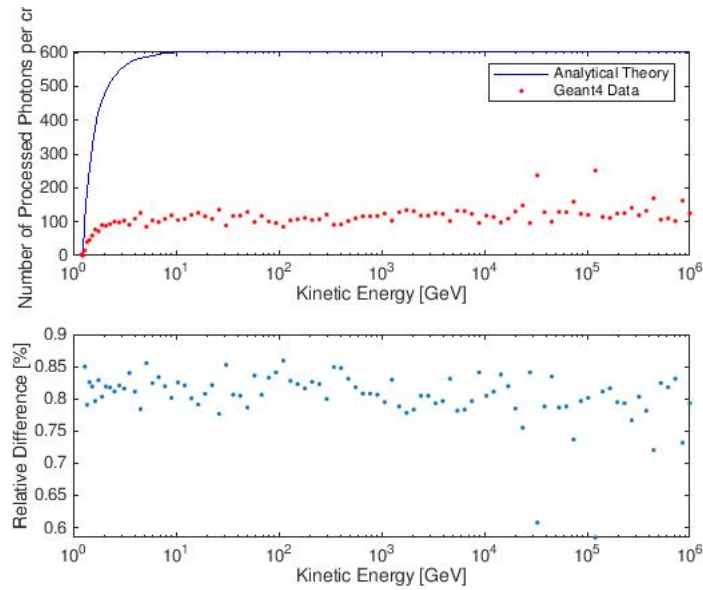


Figure 3.7: Sensitivity of simulated SiPMs to Cherenkov photons generated by a proton strike.

The same trial was undertaken for a number of different particle types. The constant detector-geometry-specific factors affecting the total photon counts are shown for each particle type. For unchanged geometry, these factors vary only marginally between different incident particle types:

Table 3.2: Cherenkov Calibration Sensitivities and Uncertainties

Particle	Sensitivity	Uncertainty
electron	0.1870	5.72%
proton	0.1958	4.04%
muon+	0.1924	4.39%
muon-	0.1994	6.57%
alpha	0.2300	3.99%
Average	0.2009	4.942%

It is evident, upon inspection that there is something of a deviation from the calibration results obtained for other particles when the trial was run with alpha particles. This is largely due to secondaries production, a result which is discussed further in the Verification chapter.

Finally, a grid-bombardment, similar to that performed in the scintillation calibration, was performed on the Cherenkov calibration model. It was possible, during the same 1.5 hour runtime, to simulate a much higher grid density for the Cherenkov grid calibration than for the Scintillation. This is simply because there are far fewer photons produced per incident particle per unit length by the Cherenkov effect than by scintillation; a fact that is borne out by the afore-detailed theory. The results of this grid-bombardment can be seen in Figure 3.8:

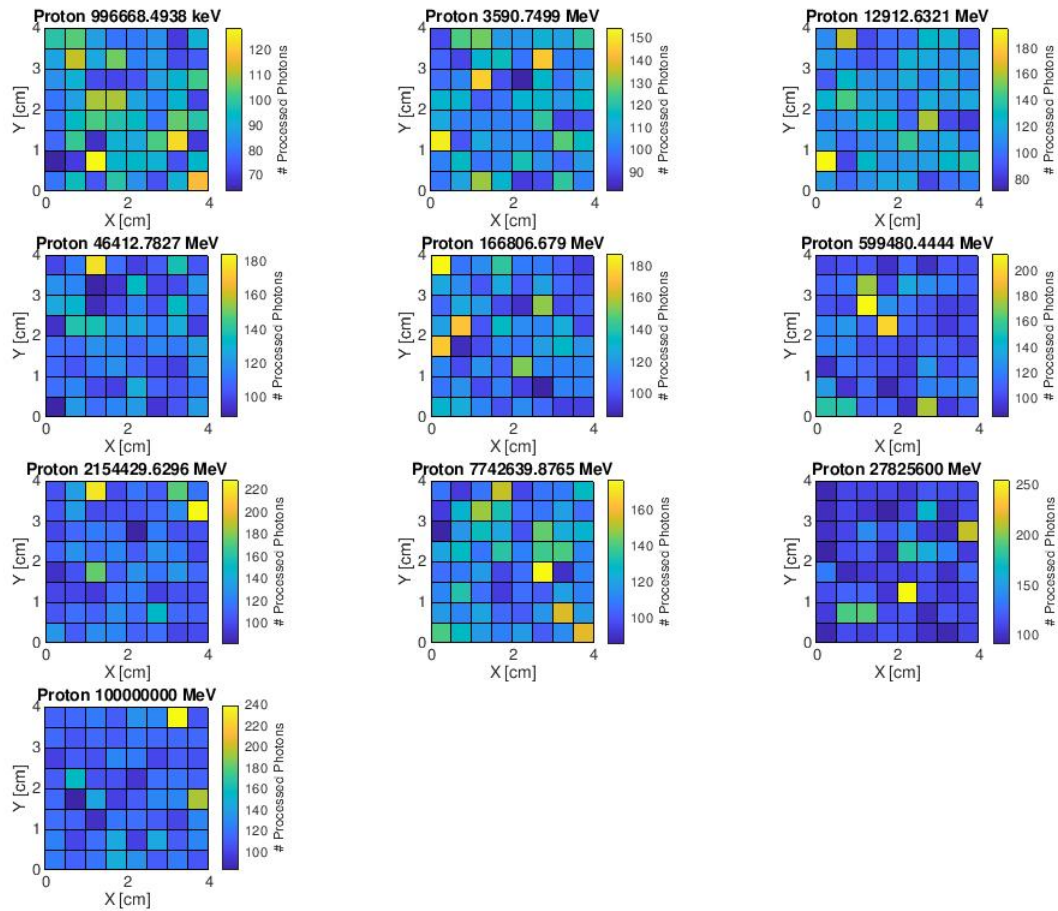


Figure 3.8: Colorimetric plots of total processed photon count for a range of incident proton energies fired at 1 quadrant of the total Cherenkov radiator block on a 4X4cm grid subdivided by 8 nodes per side

Again, as before, the uncertainty, or error, induced in the photon count output by off-center strikes was estimated by taking the standard deviation of all photons counts included within a single grid-run. Each such photon count is represented by one square in one of the grid plots in Figure 3.8. These uncertainties can be seen plotted in the following figure for each energy (one point in the following figure for each sub-gridplot in Figure 3.8). The uncertainties were normalized to the overall average value. The grid-averaged total number of photons for each energy was also plotted on the same axes for reference in Figure 3.8:

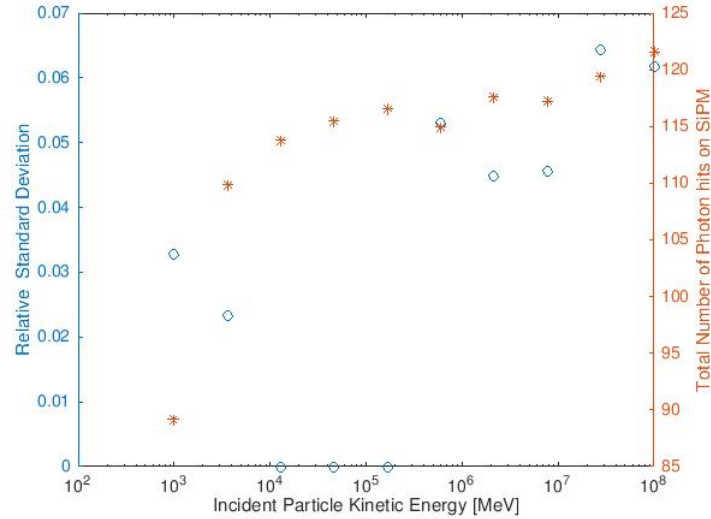


Figure 3.9: Relative magnitude of standard deviation in Cherenkov Grid Calibration Runs

It is evident that the average uncertainty in photon count is quite low at an average of approximately 5%. The uncertainty did grow marginally larger with higher incident particle energy (and therefore also photon count, plotted in orange), but the difference is minimal. The operating conclusion that can be drawn here is simply that the photon count is practically decoupled from how off center the incident strike was. This is a similar result to the grid-bombardment trial carried out on the scintillator layer, which is logical.

After the final, detail, trade study, in which the operational and material configuration (if not the dimensions) of the final parametric model was determined, it became evident that the monolithic Cherenkov radiator did not provide sufficient granularity (discussed further in the Design chapter). Thus, the monolithic design was subdivided into a dual layer of cross-laid "paddles," with the same borosilicate-glass material. The much higher SiPM-sensitive-area to glass-volume ratio of these paddles ensured that no such photon count calibration was necessary; the total number very nearly matched Cherenkov theory; though there was a fairly large deviation about this mean about the average photon count. In light of this much more efficient internal reflection, and much more consistent photon count, it was not necessary to run a full grid-bombardment, but the sensitivity of the total photon count to lateral displacement along the main axis of the paddle was tested with a pared-down line-bombardment instead of a grid bombardment. 100 protons of 10GeV were fired at the center of the paddle at evenly incremented axial displacements. The resulting photon count is shown in Figure 3.10 in red, plotted against analytical predictions:



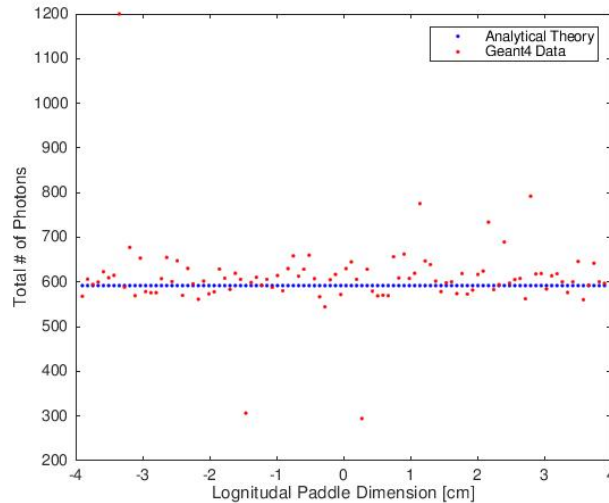


Figure 3.10: Total number of generated photons for a single Cherenkov Paddle subjected to 100 successive 10 GeV proton impacts ranged evenly along the longitudinal axis of the paddle.

The standard deviation of the line-bombardment calibration was  $\pm 14.14\%$ . This was introduced into the formula-based Cherenkov model by adding or subtracting a randomly generated deviation from the output of the Frank/Tamm formula.

The following figure shows the total number of *detected photons* for a similar line-run. This plot shows the incorporation of non-perfect SiPM modelling discussed in an earlier subsection of this chapter:

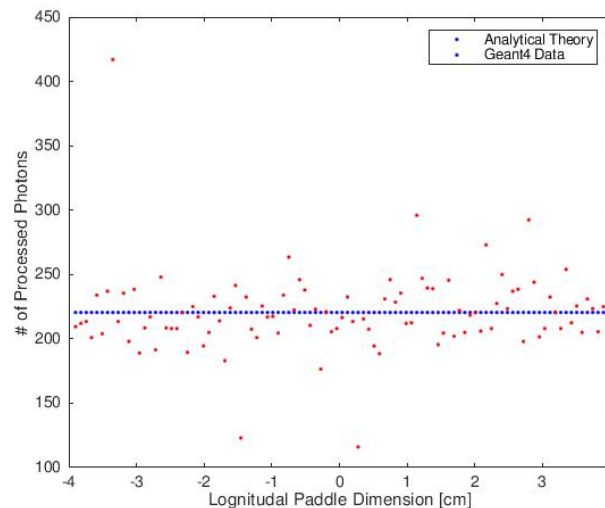


Figure 3.11: Total number of PROCESSED (vis. *detected*) photons for a single Cherenkov Paddle subjected to 100 successive 10 GeV proton impacts ranged evenly along the longitudinal axis of the paddle.

It is worth noting that the number of photons detected in a square Cherenkov radiator the same material for a "saturated" hit (maximum number of photons produced) was essentially the exact same as the number of photons produced for a long-thin paddle. This agrees with expectation because the length of the paddle (approximately 10cm) is much much less than the attenuation length for photons in borosilicate glass ( 480cm [4]).



## 3.2. Asteroid Simulation

### 3.2.1. Asteroid Model

#### Model Composition

As mentioned later, in the formal assumptions section, the asteroid 25143 Itokawa will be used as a proxy for all compositional and target definitions with the exception of shape, and possibly diameter. This asteroid is particularly good for compositional purposes because the Hayabusa mission returned a small sample of surface regolith that was subsequently intensively study for mineralogical and geological purposes [58]. Thus, the mineral (and therefore chemical) composition, as well as bulk density, of asteroid regolith used in simulations is well defined. The mineralogy reported by Noguchi et al for 25143 Itokawa regolith is tabulated below [58]:

Table 3.3: 25143 Itokawa Regolith Mineralogy

Mineral	% By Volume	Density [g/cc][46]
Olivine	64	3.4
Low-Ca Pyroxene (Pigeonite)	19	3.09
High-Ca Pyroxene (Augite)	3	3.09
Plagioclase (Labradorite)	11	2.62
Troilite	2	4.6
Kamacite	0.02	7.9
Taenite	0.2	8.0
Chromite	0.1	4.8
Ca Phosphates	0.01	3.14

Klein's "Handbook of Mineralogy" was referenced for mineral density, and mineral chemical composition [46]; both of which were used to translate the Itokawa mineralogy data provided by Noguchi into a chemical composition. The final information needed to make a custom regolith material in Geant4 was the bulk density of the regolith, which was calculated to be  $3.4 \text{ g/cm}^3$  [58].

The respective mass fractions of each *element* were computed using the following formula derived from simple first principals:

$$\rho_{fract}(i) = \sum_{j=1}^{\#min} (vol_j)(\rho_j) \left( \frac{M_i}{M_{min}(i)} \right) \quad (3.8a)$$

$$MF_{tot}(i) = \frac{\rho_{fract}(i)}{\sum_{i=1}^{\#el} \rho_{fract}(i)} \quad (3.8b)$$

Where  $MF_{tot}$  is the total mass fraction of element  $i$ , which is computed by summing the individual density contributions of element  $i$  to each of the constituent minerals  $j$  of the regolith, and dividing by the total such contribution by all elements. This method is based upon the elementary application of mixture stoichiometry that can be found in any basic chemistry or combustion text book. For reference, an open source text on mixture chemistry was consulted from Rice university [69]. The final elemental mass fractions can be seen in Table 3.4:

Table 3.4: 25143 Itokawa Regolith Elemental Mass Fractions

Element	Mass Fraction	Element	Mass Fraction
O	0.3565	Ti	0.0263
Fe	0.1926	S	0.0060
Mg	0.1104	H	0.0022
Si	0.0940	Ni	0.0011
K	0.0514	Co	0.0011
Na	0.0460	Cu	0.0010
Ca	0.0443	Cr	2.1015e-4
Mn	0.0337	V	2.0878e-4
Al	0.0329	P	1.0110e-4

It should be noted that the bulk density of 25143 Itokawa is estimated in the same paper as  $3.1 \text{ g/cm}^3$ , indicating a larger porosity throughout the interior of the asteroid[58]. Because no data yet exists directly related to the internal composition of any type of asteroid, it is assumed that the spherical volume of the asteroid interior can be modeled as a solid of the same chemical composition as the regolith, with a lower density to account for the greater porosity expected of a rubble-pile type asteroid like 25143 Itokawa.

This modeling of the interior of the asteroid as a non-porous solid with the same density of what is strongly presumed to be a highly porous solid in real life, is justifiable from the microscopic perspective of particle transport because the ultimate basis of Geant4 scattering cross sections is the probability of encountering a stationary nucleus of a particular type based upon the mass fraction of said molecule type [33]. Furthermore, if the porosity dimension of rubble-pile asteroids is fairly small, an assumption which agrees with current theory [15], then the differing effects of transiting vacuum-pocketed areas would average out over the much larger distance the muon would traverse through the entire asteroid.

### Model Shape

A few primary constraints were used to decide upon the shape of the asteroid proxy inserted into the Geant4 simulation for evaluation of backscatter, and, ultimately, instrument performance. By far the biggest constraint was the relative lack of computational power available. So, while there are .STL files available in the public domain for asteroids like 25143 Itokawa [32], the computational load of running particle transport studies on a three dimensional volume with 3,145,728 facets was deemed too high to merit the attempt. Thus, a leaf was taken out of the aforementioned 2014 white paper written by Prettyman et al [61], where the asteroid proxy was simply modeled as two concentric spheres of differing density. For this project it was decided to increase the complexity a bit in order to at least attempt to approximate the structural configuration of a rubble-pile asteroid. Thus, the final asteroid model was spherical with a uniform 3m-thick surface layer with the composition and density of 25143 Itokawa regolith discussed in the previous section. The thickness of 3m was decided partly as a guess of a reasonable regolith thickness (once again, there is very little data available with which that guess could be improved into a semi-accurate estimate), but mostly because 3m of regolith proved enough to stop virtually all secondary particles generated by GCR primary impacts on the surface *except* for the elusive muon, a panoply of neutrinos, and the odd very-very high energy heavy-nucleus primary. This does not constitute "cherry-picking" the data because muons ultimately destined to be transmitted through the bulk of the asteroid will almost inevitably hit this detector. The only exception would be extremely high-incidence angle muons which would not provide a good opportunity to deduce interior structure in any case, having only skimmed the very surface. Thus, a sensitive detector surface placed directly underneath this 3m regolith layer could detect all of the muons generated by cosmic ray impact.

As aforementioned the bulk of the interior of the asteroid was modeled with the same chem-

ical composition as the regolith layer for lack of any data on internal composition, but with the differing bulk density of Itokawa presented in the same paper from Noguchi et al [58]. The primary difference from Prettyman's model was the insertion of a few spherical inclusions of varying size and density in the asteroid model in the interest of perhaps being able to process muon-counts in the final static simulation into rough pictures of the asteroid interior. Because there is no data whatsoever that constrains the size, shape, or composition of such inclusions currently available, these inclusions were included solely on the chance that simulation data processing may be able to yield basic tomographic results. As a result, it was deemed more important to include a variety of inclusion compositions and densities instead of attempting to more accurately represent hereto-forward unknown natural constructs. No fewer than three inclusions were included in the asteroid model using pure materials of elements selected first for their density difference, second for their presence in the original 25143 Itokawa mineralogy [58]: These materials include lower density inclusions matching the chemical composition and density of the aforementioned regolith, mid-density inclusions of troilite, and high-density inclusions of taenite.

Finally, the diameter of the asteroid model, which was originally intended to be constrained by the average bulk diameter of 25143 Itokawa, was instead set to be 100m. The reasons for this change are described in the next section. This asteroid model (with supplementary backscatter sensitive detector volumes) can be seen in Figure 3.12. The inclusions are the colored spheres seen within the asteroid volume. Close inspection will show the just-barely visible 3m-thick regolith layer just under the surface.

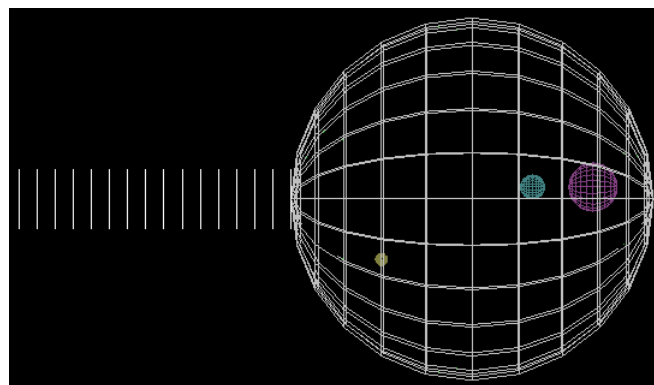


Figure 3.12: 100m Asteroid Model

### 3.2.2. Asteroid Radiation Environment Simulation

The ultimate goal of this project was to insert the final instrument design into as realistic a simulation as possible to attempt to assess its hopefully correspondingly realistic performance. The major simulation constraint, as almost inevitably appears in any computer simulation of any type, was the availability of computation power and time. This has been mentioned before, and it is worth mentioning again. This thesis was performed exclusively on an Acer Aspire E15 laptop with an intel i7-7500U, 2.7GHz processor and 8GB of RAM. Server time on 9th floor of the TU Delft Aerospace faculty was requested, but for one reason or another, never materialized. It must be said that this turned out to be both curse and blessing. Curse in that such computational limitations drastically curtail the raw scope of the simulations that can be run, but blessing in that one was obliged to devise creative ways to achieve similar results with lesser computational expense. As it happens, this need to MacGyver and jury-rig yielded some of the more critical insights of this thesis. Regardless, this relatively low computer-power budget yielded some very rigid constraints that shaped much of the simulation paradigm used herein.

### Simulation Normalization

Firstly, and arguably most importantly for this section on asteroid modeling, one is obliged to deal with the spectre of simulation normalization, which is fundamentally critical to correctly extracting useful results from any simulation that needs to relate the number of injected particle to time. Basically, this is every result gathered in the calibration simulations of the asteroid environment. As a useful exemplar, and the ultimate basis of normalization for all particle sources discussed in the Asteroid section of this chapter, the normalization of GCR primaries will be discussed in this subsection.

SPENVIS, and ultimately the CREME96 model, which were used to generate general particle source macros used to simulate all GCR primary particle spectra, offer the option to handle normalization within the macro itself [40]. This is perfectly acceptable if one uses only the spectra described in the macro itself. Regrettably, it was necessary to build particle sources not only derived from such GCR primary spectra (i.e. a muon-only source derived from the muon-production resulting from GCR-primary bombardment of an asteroid), but also to combine other particle sources with the GCRs. To be blunt, the documentation of SPENVIS is not robust enough to allow easy manipulation of internal normalization, so it was decided to normalize particle sources *retroactively*. This is possible because the internal normalization of the GCR spectra generated by SPENVIS can still be used for both the species proportions, and the energy proportions.

The SPENVIS macros consist of a number of separate particle sources that define their energy spectra with a pointwise energy histogram generated from the CREME96 model. There is one such source for every particle species. Each source (and therefore each particle specie) has a different "intensity" which theoretically corresponds to a real-life differential particle flux ( $I_N$  in this project's nomenclature), but the mechanism of such correspondence is unclear. Thus, the source intensities within this macro were considered relative, used only to determine the percentage of each particle species that would be injected.

The energy spectra themselves, are essentially a discrete number of points corresponding to the probability density function (PDF) of energy distributions. Practically, this presented itself as a series of PDF (histogram) coordinate pairs with the first coordinate representing a particle energy in MeV (bin edge for the histogram) and the second coordinate representing the corresponding count rate (non-normalized intensity). By multiplying the two, or integrating the smooth PDF, one could get the probability that a particle of that energy would be injected. This is represented in the following equation [43]:

$$\int_{E_0}^{E_1} PDF(E) dE = probability \quad (3.9)$$

The in-source normalization factor generated by SPENVIS is simply the value by which, if multiplied by the integral in Equation 3.9 evaluated from  $-\infty$  to  $+\infty$ , would result in a value of 1. In other words, the normalization factor transforms the integrals of the PDF into terms of % probability. This is reflected below [43]:

$$NF = \left[ \int_{-\infty}^{+\infty} PDF(E) dE \right]^{-1} \quad (3.10)$$

The in-source normalization is straightforward and easy to interpret with the above equations, but the normalization between particle species sources is considerably less clear. However, because, as aforementioned, the normalization produced by SPENVIS does take care of both the relative abundance of particle species, and the relative abundance of different kinetic energy levels within those species-sources, one needs only to be able to relate the number of particles injected to some timescale.

Because all particle sources discussed in this section (the Asteroid section), are ultimately derived from the GCR spectra, the time-scaling of each of these sources can also be derived

from that of GCR. To do this, one must take a closer look at the overall differential flux of the GCR primary particles:

The maximum differential flux for low-energy protons, as published by Geisser and the Particle Data Group independently [34][56], is approximately  $1488 \text{ m}^{-2}\text{sr}^{-2}\text{s}^{-2}\text{GeV}^{-1}$ . This is only for the most abundant energy and particle species: protons at 0.2624 MeV [56]. However, even if all of the remaining maximum fluxes for each heavier particle species was added to this maximum flux for protons, the total would be about the same; the next highest maximum flux is that of He nuclei, and it is three orders of magnitude lower than that of protons. Thus, the proton flux is used to normalize the SPENVIS GCR macro timescale. It is once again reiterated that the maximum differential flux is sufficient to determine the timescale because the energy proportions of each GCR primary species are handled by SPENVIS. That is, if one knows the maximum count rate of any species, it is thereafter possible to determine the count-rate of all the other species from this one datum. The ultimate goal is to determine a bare count-rate for all GCR primaries for a spherical particle source.

This obliges one, first, to remove energy dependence from the differential flux presented above. This was done by simply normalizing the flux to the corresponding energy as presented by the PDG [56]. This yielded a rate of  $390.460 \text{ m}^{-2}\text{sr}^{-2}\text{s}^{-2}$ . For a spherical particle source of the type discussed, characterized by a total solid angle of  $4\pi$  steradians, and a surface area equal to  $4\pi r^2$ , it is possible to get the count rate per square meter per second by multiplying by the full-sphere solid angle; this results in a rate of  $4906.550 \text{ m}^{-2}\text{sr}^{-2}$ . Finally, the overall count-rate of particles striking the surface of the 100m asteroid model can be determined by multiplying this last number by the asteroid surface area. This results in a total of  $1.387296\text{E}+9$  GCR primaries hitting the asteroid surface every second.

This hit rate, obviously, increases with the square of the radius of the spherical particle source. Thus, the 100m diameter asteroid model was a compromise between attempting to approach the average bulk radius of 25143 Itokawa, and having a small enough model that it would be possible to generate a statistically significant amount of data in a reasonable amount of time. Admittedly, the compromise was quite heavily on the side of a computationally efficient model, but in comparison to a fairly similar study performed by Prettyman et al in 2014, this asteroid model falls between the two radii they used (50m and 800m)[61]. It goes without saying that even one second of simulation is far beyond the computational budget of this project at 1.39 billion particles per second, with or without server time. As it happens, it was possible to simulate approximately 1 million GCR primary impacts every 3 hours. 1 million injected GCR primaries corresponds to around 6.6316 milliseconds of bombardment.

### Backscatter Characterization

The asteroid model was bombarded by a spherical particle source using GCR primary energy spectra and species distributions, random injection timing, random injection coordinates, and random injection angles following a cosine distribution. The spherical particle source was concentric to the asteroid model itself, and extended 1m above the surface.

Though it was very time-intensive, this GCR bombardment was critical for two primary functions: characterizing the backscatter, and generating the best estimate possible for the number of muons generated in the Asteroid's regolith layer that might eventually transit the entire asteroid and be detectable on the opposite side. This latter piece of information was used to create another spherical particle source with a shape identical to the original GCR source, but injecting only muons characterized by the differential flux observed by the under-regolith sensitive detector volume. Ultimately, there was time for an accumulation of bombardment data representing over 9 million injected GCR primaries (and 30 hours of total run-time). The implications for both the regolith and backscatter characterization are discussed in the following subsections.

Though the shape of hadronic and EM showers caused by GCR primaries is generally conical, with the vast majority of the secondary particle momentum vectors pointing in the same gen-

eral direction as that of the primary with small dispersion, there is still a smaller probability of some secondary particles rebounding in more or less the opposite direction as impact, this is known as backscatter [34]. A hypothesis was made with respect to backscatter quite early in the thesis: Namely, it was supposed that if the instrument's field of view was fully occulted by the asteroid it was targeting, the asteroid itself would block all GCR primaries that would impact the instrument from that solid angle. Thus, the only particles that would hit the detector face on would come from the asteroid surface; backscatter, and crucially, muons that had transited all the way through the asteroid. The active shielding algorithm designed to filter all of the simulated data generated by the instrument and distinguish muons, is quite simplistic and able only to coarsely filter the data. The reasons for not spending more time to improve this algorithm are discussed further in the Design chapter, but one critical justification for doing so is linked to the above hypothesis: namely that in the umbra of the asteroid, the instrument wouldn't *have* to filter out many extraneous particle signals; there would be only the transiting muons and backscatter of a relatively low flux and energy.

Obviously, it was necessary to characterize the expected backscatter off of the asteroid model described in the previous section, not only to test said hypothesis, but to gather backscatter data for a backscatter particle source in the final, static, integrated simulations. To this end, the asteroid model described in the previous section was subjected to bombardment by the GCR primary spectrum generated by SPENVIS [40], and a series of sensitive volume detectors were placed at regular intervals along a normal line extending from the asteroid model surface outward. The basic configuration of this simulation can be seen in the following figure. The basic set-up is the previously seen 100m asteroid model with spherical inclusions with a number of virtual (massless) 20mX20m square detector surfaces included to characterize both muon flux and backscatter flux at a number of altitudes:

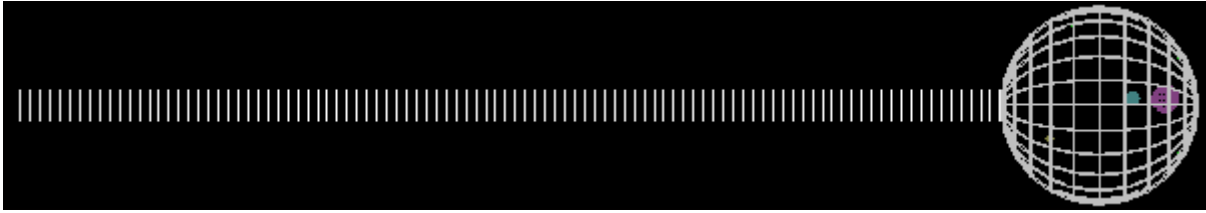


Figure 3.13: Simulation set up for backscatter characterization

The particle source used was as described in the previous subsection, and a great deal of backscatter was generated. From the particle hit data gathered for each of the 100, 50mX50mX1cm sensitive detector volumes, a backscatter radiation source consisting of a 2mX2m square surface placed directly between of the instrument emplacement and the asteroid model was created. The large number of backscatter detectors that can be seen in Figure 3.13 allowed the particle injection conditions of this backscatter source to be parameterized by the distance between the instrument and the surface of the asteroid model. This, in turn, was part of the overall plan to run a number of final static simulations at differing altitudes to attempt to ascertain an optimum instrument altitude.

For the purposes of presenting the results of this backscatter characterization in this report, it was deemed more expedient and concise to generate the conventional metric of differential flux parameterized by altitude above the asteroid model surface. With the goal of transforming the raw hit data into differential flux with the aforementioned units of  $m^{-2}sr^{-2}s^{-2}GeV^{-1}$ , the particle energy and count rate were pulled straight from the results. These were normalized to the area of each of the backscatter-detectors (50mX50m), and the total simulated time for 9.2 million injected particles (2.58932ms). To complete the conversion one normalizes to the average solid-angle distribution of the incident particles. This is reflected in the following equation:

$$\phi_N = \frac{mean(count_N)}{mean(E_0)A_{SD}t_{run}\Omega} \quad (3.11)$$

Where  $\phi_N$  is the differential flux for a particular particle,  $count_N$  is the particle count for the same particle species,  $E_0$ , we recall, is the incident energy for the particle,  $A_{SD}$  is the flux area of the sensitive detector volume in question,  $t_{run}$  is the simulated time (not to be confused with the simulation runtime), and  $\Omega$  is the mean solid angle that can be "seen" by the detector in question. In this case, the backscatter detectors were modeled, essentially, as rectangular surfaces; they can, therefore, "see" one half of the celestial sphere, so  $\Omega = 2\pi$  steradians for all altitudes.

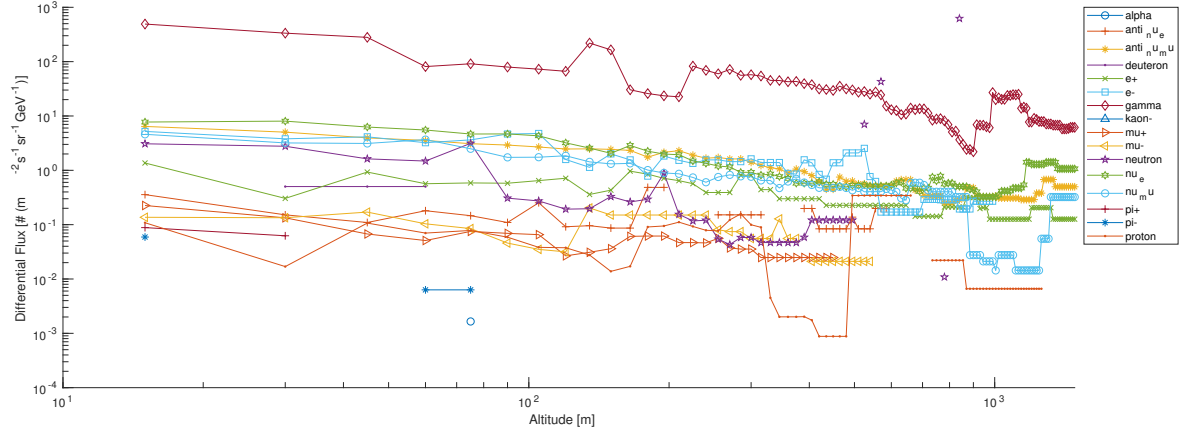


Figure 3.14: Differential flux for backscatter particles as a function of distance from asteroid model surface

Because the final detector scheme selected makes use of the Cherenov effect and the charge-deposition effect in semi-conductor devices (PSDs), it was deemed unnecessary to retain any non-charged particles like neutrons, neutrinos, and gamma rays. The thus-simplified plot of the differential flux can be seen plotted below:

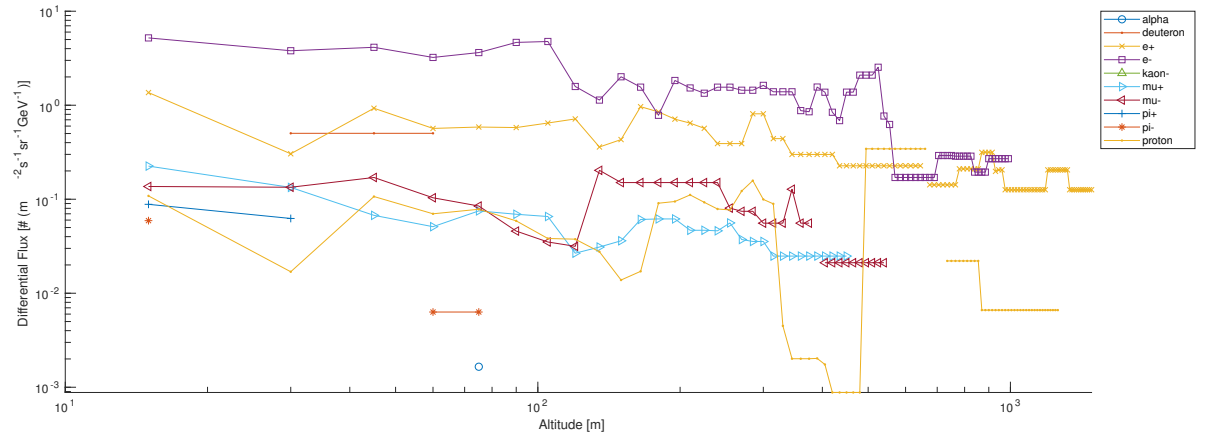


Figure 3.15: Differential flux for charged backscatter particles as a function of distance from asteroid model surface

The final step in this particular analysis was to evaluate the hypothesis that any particle radiation from the surface of the asteroid would be either easily discarded, low-energy, backscatter, or transiting muons. To clarify this evaluation, the mean kinetic energy of each particle species is plotted below as a function of altitude:

By and large, Figure 3.16 confirms this hypothesis. While there was one alpha particle event

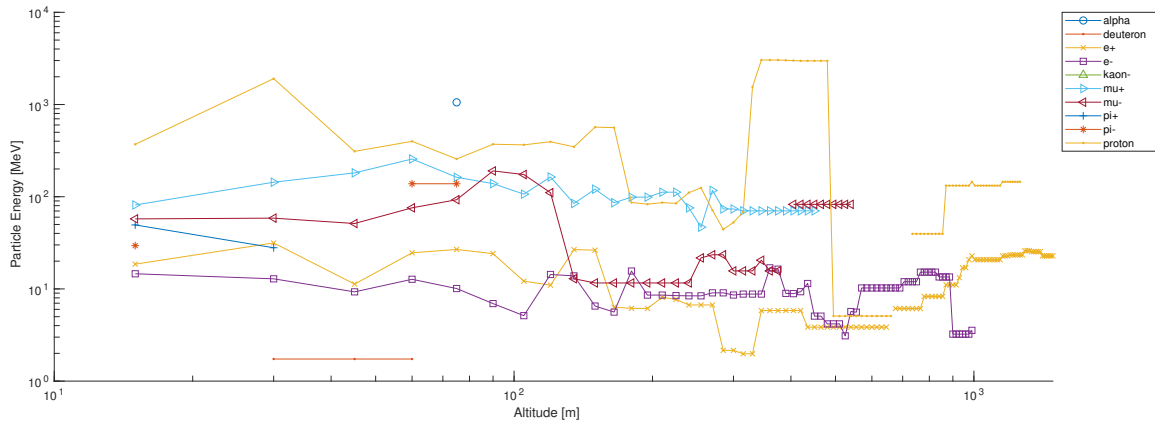


Figure 3.16: Mean kinetic energy of each charged particle species parameterized by altitude from the asteroid surface

of around 6 GeV, and a number of protons averaging a little over 1 GeV, the vast majority of the detected particles (70%) were under 300 MeV, and would therefore not cause a Cherenkov pulse in the borosilicate paddles. A few peculiarities are worth addressing in this figure, however. Firstly, the alpha particle event is singular. This is purely a function of the oft-mentioned limitations on computational time. If more injected GCR primaries were possible, it is probable that more alpha particles would be evident in these results. However, none of these particle fluxes were used as inputs to further simulations, so any uncertainty caused by statistical insignificance in the relative abundance of outlier particles like the pions and alpha particles of Figure 3.16 does not propagate through the rest of the report; this is used primarily as a means of testing the asteroid-as-GCR-shield hypothesis mentioned in the Design chapter. Secondly, there are some large discontinuities in this data. This is partly caused by the aforementioned relatively low overall particle counts, but is also most likely caused by a difference in the most probable production angle of certain particles and particle decay chains. That is: a proton may be produced as a direct secondary in a hadronic shower, or may result from some further particle decay or interaction that changes the angular distribution. As the altitude increases, the virtual detectors used act like a collimator, excluding high-angle particles. This collimation most likely causes certain particle dispersions characteristic of a particular particle generation path to be blocked. However, the shape was not investigated in further detail for much the same reason that the few-point particle outliers were not: any uncertainty in the shape was not propagated further. The overall mean of the relative abundances of the various charged particle species can be seen in Figure 3.17:



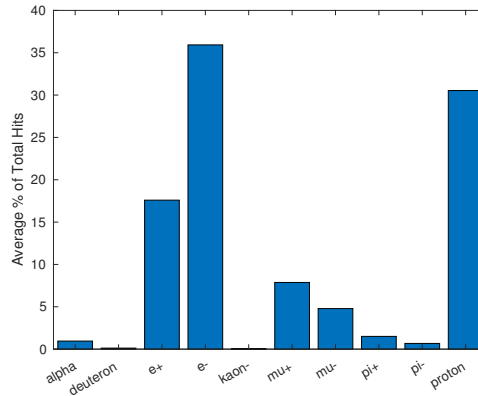


Figure 3.17: Relative abundance of charged particle species averaged over all altitudes

While all particles captured in this backscatter characterization study will be used in their respective abundances for the final integrated simulations, the very small proportion of alpha particles can be neglected in evaluating the aforementioned hypothesis. Only the muon and proton signals cause some worry at face value. However, the highest energy muon does not exceed 400MeV, and would therefore be rejected because it will not trigger a Cherenkov response. This leaves only the proton signal. Again, however, this signal has a very small flux relative to the proton/electron/muon beam used to simulate and analyze instrument response in the final parametric study, and is of relatively small average kinetic energy compared to most GCR primaries and the muons of interest, regardless. The effect, if any, of this proton signal will be quantified in the MIDP and MDE muon-identification performance metrics of the final integrated simulations.

One final note to make is that the results of this backscatter study, particularly the relative abundances shown in Figure 3.17, verify the choice, and even the relative proportions of most particles used in the test-beam used to perform the geometric parametric study (results described in detail in the Design chapter). For the primary geometric study, the test beam assumed that protons and electrons would represent approximately 30-50% each of the total proportion, with muons representing 10-20%. It is, indeed, a bit surprising that the relative abundance of particle species in the backscatter spectrum is even within the realm of similarity to this arbitrarily chosen test-beam composition; let alone a fairly good match. Chronologically, there was not a good way to perform the above relative abundance analysis before the geometric parameter study, which explains the choice to select an arbitrary test beam composition based solely upon probable species present in such a radiation environment, and to set the relative abundances arbitrarily. It is a good sign, however you look at it though, that this choice was retroactively validated by more detailed simulation results even if it was something approaching dumb luck.

### Muon Production in Regolith

As mentioned previously, it is not computationally possible to perform a fully realistic simulation of the muography scenario. Therefore, the most important part of said scenario, namely the muons, were split away from the GCR primaries impacting the surface of the asteroid, and a new spherical source of the same basic dimensions was created that injected only muons into the asteroid interior. To do so, it was necessary to determine the differential flux of muons produced by GCRs impacting the asteroid surface. This data was collected simultaneously with the backscatter data used in the previous section.

A spherical-shell sensitive detector volume of negligible thickness was placed concentric to the asteroid model itself under about 3m of regolith material. This placement was done to ensure that the majority of the non-muon secondaries generated by GCR impact in the regolith had time to dissipate, thus ensuring that the dominant signal at the sensitive detector was muons of sufficient energy to transit the bulk of the asteroid (and neutrinos, of course).

Even with this relatively large number of primaries, the number of muons detected at the SD was remarkably low. In fact, appreciably less than 100 muons were detected over the whole simulation. It was originally uncertain whether this was enough to yield statistical significance. However, as detailed in the Verification and Validation chapter, the differential flux results obtained from this scant dataset yield a fairly remarkably good match to the results published in the oft-mentioned white paper by Prettyman et al [61]. Therefore, in keeping of the limited quality and validity of data that was anticipated in the Introduction of this thesis, this minor validation was deemed of sufficient quality to yield results from which decent *qualitative* conclusions could be drawn. In other words, in keeping with the nature and scope of a feasibility study. They would *not* have been deemed statistically significant enough to move forward if not for said validation. These results are plotted below:

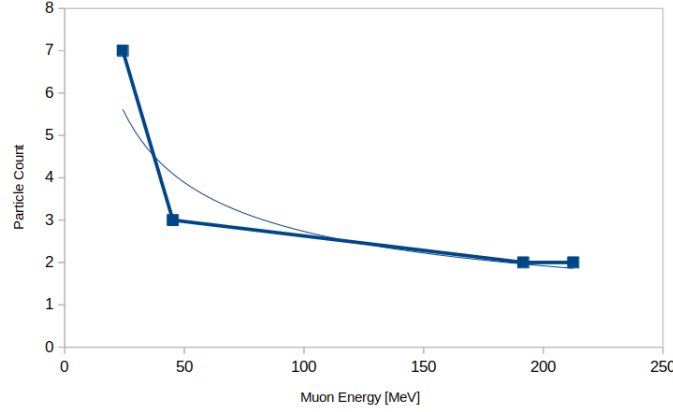


Figure 3.18: Count of all muons generated by GCR primary bombardment at a depth of 3m beneath regolith

Because the total-count-curve shown in Figure 3.18 does not have data points at most higher energies, the built-in interpolator within MS Excel 2010 was used to generate a curve fit using a power-law model that is quite commonly observed for particle energy spectra [33]. This interpolation can be seen below:

$$CR = 28.449787E^{-0.5087117} \quad (3.12)$$

The coefficient of determination ( $R^2$ ) for this interpolation was 0.856. This indicates only a fair interpolation, but was deemed acceptable for the low number of data points available.

From this point, it was only necessary to generate a probability density function (PDF) that a muon would fall within a certain energy range, and the differential flux, to populate the user-defined energy spectrum histogram in an addendum to the previously mentioned SPENVIS particle-source macros. A procedure very similar to that used in the subsection included on normalization included earlier in this chapter, was then used to generate an overall count-rate and differential flux. The total count rate for muons generated in the regolith of a 100m asteroid of a composition similar to that of 25143 Itokawa was 95.068 particles per second. This corresponds to total differential flux (summed over all energies) of  $1.30261E-3 m^{-2}s^{-1}sr^{-1}GeV^{-1}$ .

### Effects of Regolith-muons

After gathering the necessary data to build a muon-only spherical particle source with which to inject transiting muons into the asteroid model, it was deemed wise to test the source in interaction with the asteroid. It was originally assumed that this muons-only source would be much much faster than GCR primary bombardment because of the far lower count-rates. Unfortunately what, indeed, turned out to be low muon count rates compared to GCR primary rates, were a double edged sword. The low differential flux meant that a very large number of muons had to be injected before a particular area (for instance, of an instrument) on the opposite side was struck by a transmitted muon. Unfortunately, this coupled with a far-higher secondary generation rate as the muons were transported through the interior of the asteroid, and still used up far too much computation time. A computation rate of about 5.5 primary injections per second was achieved. This was far too slow. A simulation compromise was reached: all of the secondary particles generated by muons transiting the asteroid volume were killed before they had a chance to propagate. This preserved the targeted effects of the muon, but drastically improved simulation rate to around 67 primary injections per second. It is important to note that this compromise removes a potential background-noise source by removing the muon-generated secondary particles that were close enough to the surface to possibly be released into space. However, a first-order analytical comparison can be derived by comparing the maximum GCR primary backscatter flux ( $5.202 \text{ m}^{-2}\text{s}^{-1}\text{sr}^{-1}\text{GeV}^{-1}$ ) and the muon flux ( $1.30261\text{E-}3 \text{ m}^{-2}\text{s}^{-1}\text{sr}^{-1}\text{GeV}^{-1}$ ). Furthermore, the number of relevant secondaries produced is quite small because it must occur from an event in the upper few meters of regolith as the muon exits. Considering this, and the fact that the respective fluxes are separated by 3 orders of magnitude it is reasonable to neglect the contribution of the muon-backscatter to the overall backscatter signal.

Thereafter, it was deemed useful to conduct a similar study to that investigating the differential flux of backscatter as it changed with respect to altitude. The same model was used, as can be seen in Figure 3.13, but it produced such low muon fluxes at altitudes higher than approximately 100m that the model was modified to investigate only those altitudes less than 100m in greater detail. Thus, a planar sensitive detector of 10X10m was placed at 1m intervals between 0m and 100m of altitude. Using the methods very similar to those detailed in the previous subsection on normalization, the average fluence, in muons per square meter, was computed for all of these altitudes. The differential flux and the count rate can be seen plotted below:

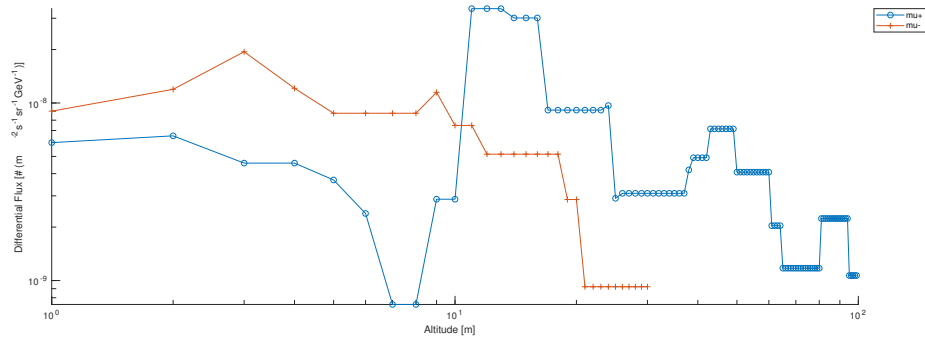


Figure 3.19: Differential flux of all muons transmitted through the bulk of the asteroid model parameterized by altitude

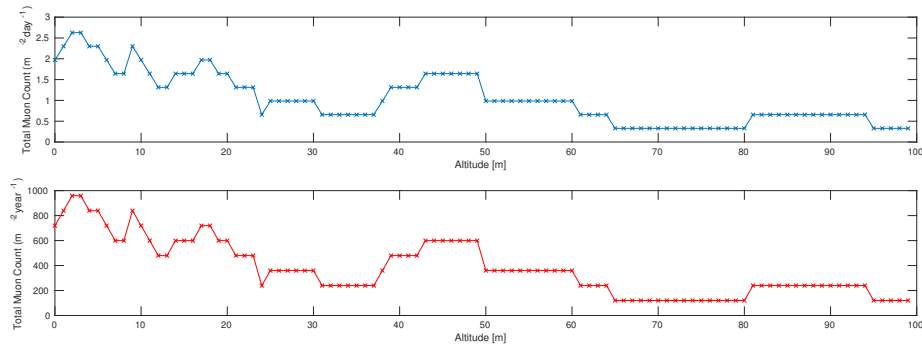


Figure 3.20: Count Rate of all muons transmitted through the bulk of the asteroid model parameterized by altitude

Though it is discussed in greater detail in the Verification and Validation chapter, it is necessary to point out that the muon count rate in Figure 3.20 matches that presented by Prettyman et al within about  $\pm 75\%$ , which, in and of itself, is quite remarkable for two different models using different simulation packages and boundary conditions (Prettyman et al based their muon source, at least in part, on scaled atmospheric muon-flux data), but the difference is most likely largely attributable to differences in density used in the two models. 75% may seem like a very large discrepancy, but the error was expected to be at least an order of magnitude greater due to simulation package and asteroid-model chemistry differences. Furthermore, Figure 3.18 yielded raw muon production rates that fell within the error-bars of those presented in Prettyman et al; again, any differences are likely due to different simulated regolith/asteroid densities.

## 4.1. Assumptions

A number of assumptions were made during the course of this thesis project to limit the scope and serve as constraints on the design itself. They are presented as follows, arranged in categorical order.

### 4.1.1. Mission

A bare minimum of mission planning was necessary to better constrain the boundary conditions surrounding any potential design. These are mostly with respect to the target asteroid itself, and the flight and attitude controls that are relevant to the proper functioning of the instrument.

Table 4.1: Mission Assumptions

#	Category	Sub-categories		Date	Assumption
1.0.0.0	Mission	Asteroid	Shape	1-Mar-2018	Surface density and shape of targeted asteroid will be known.
1.1.1.0	Mission	Flight	Orbit	1-Mar-2018	Trajectory will be a closed orbit of asteroid, no flybys.
1.1.2.0	Mission	Flight	Attitude	24-April-2018	Instrument will always point in the nadir direction.
1.1.3.0	Mission	Flight	Attitude	24-April-2018	Nadir will be defined as the nadir of a sphere circumscribing the central body.
1.2.0.0	Mission	General		3-May-2018	Instrument will have minimum of 6 months operational lifetime.

The first assumption in this category (1.0.0.0), regarding the foreknowledge of much of the Asteroid's shape and surface characteristics, is a necessary input to geological muon tomography [61]. Specifically, the output of muon tomography is generally the energy, count-rate, and trajectory of transiting muons; by working backwards with the relevant matter/particle interaction models like Bethe Bloch or radiative loss theories that begin to dominate the behavior of muons in matter at high energies, it is possible to calculate the average density along the path of the muon through the intervening rock [45]. Without knowing this path-length, however, it is obviously impossible to estimate the average density. Because this information lies outside the scope of the thesis, it is assumed that topographical data of the

target asteroid is already available or can be easily collected in the initial phase of the mission itself.

It is further assumed (in 1.1.1.0) that the spacecraft carrying the instrument will fly in a closed orbit around the Asteroid. This is mainly based upon the relatively low expected differential flux of GCR primaries [56], and the fact that a brief flyby would not allow sufficient time to detect enough of the sparse muons to be useful for tomography.

The assumptions regarding the pointing of the instrument (1.1.2.0) and the definition of the nadir (1.1.3.0) are simply based upon the fact that any hodoscope has a functional field of view, much like almost any directional instrument, and that pointing the centroid of this field of view at the centroid of the target asteroid (vis. along the nadir vector) is simply the most effective way to ensure that as much of the asteroid remains in view as possible thereby maximizing the chance that transiting muons from the asteroid surface will be detected. The choice of a more or less fixed nadir definition (as opposed to one which more accurately took into account the shape irregularities of most smaller asteroids) is simply because no more complex definition is needed to keep the asteroid firmly in the middle of the instrument's field of view.

Finally, (in 1.2.0.0) a lifetime of 6 months was chosen as a bare minimum based upon Prettyman et al's assessment that muographic integration times may exceed weeks or months [61]. Coupled with the fact that orbital insertion around such irregular bodies is a complex process (ex. the Rosetta Mission), 6 months was deemed a fair estimate of the bare minimum time needed to collect any useful data.

#### 4.1.2. Physics and Simulation

The following table presents all assumptions relating to the boundary conditions and approximations necessary for particle radiation simulations using Geant4:

Table 4.2: Physics and Simulation Assumptions

#	Category	Sub-categories	Date	Assumption
2.0.0.0	Particle Physics	Muon	24-April-2018	Likelihood of muon decay within detector is negligible regardless of detector geometry.
2.1.0.0	Particle Physics	Simultaneity	14-Sept-2018	No 2 primary particles from the ambient radiation environment are likely to hit within the established minimum time resolution.
3.0.0.0	Simulation	Approximations	20-June-2018	Assume perfect internal reflection within Cherenkov Radiators and/or Scintillators.
3.1.0.0	Simulation	Convention	21-June-2018	The right hand rule will be used for all determinations of the sign of rotations or rotary values. I.e. where necessary, counter-clockwise is positive.
3.2.0.0	Simulation	Verification	26-July-2018	Verification results for the most common, low-mass GCR primary particle types, implies verification for less common, high-mass GCR nuclei.

First off, an assumption (2.0.0.0) is made that, if a muon enters a detector, it will also exit without decaying. This is based upon two practical considerations: the range of a muon, even after transiting a large swath of asteroid, is far greater than the length it would transit in a detector, and it is far simpler to simply throw out any such unlikely data point instead

of expending effort on the unlikely eventuality.

The next assumption (2.1.0.0) is perhaps the most critical one with respect to the basic active shielding algorithm designed for the purpose of this project. It simply states that the very small likelihood of *primary* particles transiting the detector in the correct direction simultaneously is negligible. There are, definitely, phenomena that could result in such simultaneity, not the least of which is a hadronic shower occurring upstream of the detector. Indeed, Prettyman et al cite such dual-hits as a possible criterion for muon identification since they are often produced via pair production [61]. However, such shower events almost inevitably involve the particles produced to diverge in space. The vast magnitude of space, coupled with the very small target of any instrument configuration studied in this project, render the chances of dual hits like this negligible. Assuming non-simultaneity like this also allows one to fairly easily identify secondary particles created by hadronic or EM shower events occurring *after* the primary particles have reached the detector.

Looking more closely at the instrumentation within the detector itself, transparent, photon-producing, elements are found in almost all particle detectors, either space-borne or terrestrial, aimed at studying high energy particles [54]. It is merely assumed (in 3.0.0.0) that photons will reflect perfectly with no appreciable losses within any such transparent elements, because it is far easier to model in Geant4. Indeed, this was verified in the context of the simulation platform itself inasmuch as turning on the computationally-expensive, but more realistic, imperfect surface parameters that more closely reflect the true performance of foil-wrapped transparent blocks. The difference between photon counts was small and showed no consistency between trials; indicating that any effect of imperfect vs. perfect internal reflection is less than the other uncertainties in the simulation itself.

The final assumption (3.2.0.0) that requires treatment here is the assumption that single-particle verifications done for primary particles of lower mass is easily extrapolated to the expected results for particles of higher mass. While very high energy, high mass, GCR primaries may yield unforeseen effects due to the creation of exotic short-lived intermediary particles, they are very rare, and, critically, do not change the effects of either scintillators or the Cherenkov effect. It was, therefore, not deemed necessary to calibrate for these particles, though it is very important to note that they are included in the spectra of GCR primaries included as background radiation.

### 4.1.3. Detector Design

#### Detector Architecture

The primary purpose of the assumptions that relate to the architecture of the detector itself is to constrain the number of variables that would otherwise have to be taken into account in design trade offs.

Table 4.3: Detector Architecture Assumptions

#	Category	Sub-categories		Date	Assumption
4.1.0.0	Spacecraft Design	Detector	Architecture	24-April-2018	No more than 10 stacks will be used in the hodoscope.
4.1.0.1	Spacecraft Design	Detector	Architecture	24-April-2018	There will be no less than 2 SiPMs used per optical detector element.
4.1.0.2	Spacecraft Design	Detector	Architecture	1-May-2018	Instrument mass will not exceed 200 kg for use in a small-sat bus configuration.
4.1.0.3	Spacecraft Design	Detector	Architecture	2-May-2018	Assume that all ancillary electronics and support equipment/materials per hodoscope stack do not differ between stacks.
4.1.0.4	Spacecraft Design	Detector	Architecture	7-May-2018	Assume that both spacecraft position and attitude data are gathered by instrumentation in the spacecraft bus (i.e. outside the scope of this project)
4.1.6.0	Spacecraft Design	Detector	General	25-July-2018	Refractive index of all transparent materials is assumed to be constant between 1000nm and 300nm wavelength.

With respect to simplifying assumption 4.1.0.0: many instruments aimed at collecting data about high energy particles have a large number of different layers in a more or less hodoscopic configuration. However, in surveying existing instruments during the course of the literature study, especially those used in aerospace applications, none had an excess of 10 layers. As a representative example, high altitude balloon-based CREAM instrument, has exactly 10 layers [11]. This instrument, in particular, was seen as one of the closest analogs to the application of this thesis, and was seen as a good benchmark for the instrument architecture, including the number of instrumented layers.

The number of SiPMs used for optical sensing schemes (4.1.0.1) is based purely upon good systems engineering practices which strongly indicate redundancy of this nature. In the end, most optical elements, like Cherenkov paddles, use 2 SiPMs.

At this pre-preliminary design phase of the overall design process, constraining the mass is extremely difficult. It was deemed most expedient therefore to simply set a maximum mass beyond which any detector design would be considered immediately unfeasible (in assumption 4.1.0.2). This was originally based upon a CubeSat architecture, but simulation results eventually indicated that the more passive shielding between stacks, the better. Ultimately this translates into instruments that are considerably larger than any standard CubeSat form factor. It was therefore decided to broaden the scope of the project a bit and include the possibility of small satellite configurations as well as micro and nano satellite buses. While the categorization of the different size classes is vague at best, the order of magnitude of a few hundred kilograms seemed reasonable as an upper limit, and 200 kg was chosen as an estimated mean value for primary payloads of satellites in this class. No formal study was done to arrive at this number.

The next assumption (4.1.0.3) regarding the uniformity of instrumentation and electronics used in each hodoscope stack is primarily based around the architecture of the parametric model built using Geant4. It turns out that in exchange for having the ability to change a few key parameters like length, number of stacks, etc. one is obliged to accept that each stack must be identical. This assumption is essentially a reflection of this modeling idiosyncrasy, and acknowledges that results may differ *slightly* for real instruments with small variances between different stacks in the hodoscope.

The next assumption (4.1.0.4), specifically regarding the data available from the spacecraft



bus itself, is perhaps the most important architectural assumption. In essence, one assumes that the instrument would be integrated with a pre-existing spacecraft bus of appropriate size that has all of the generally available payload support functionalities pre-designed and manufactured. This assumption is made because using valuable project time to design or consider anything but the broadest non-instrument spacecraft characteristics would be beyond the scope of the project. It is possible to buy an 'off-the-shelf' spacecraft bus, or to have a subcontractor take care of the entire process of designing a bus around the instrument; so such design tasks are not considered in this thesis.

Finally, it is assumed (in 4.1.6.0) that the optical elements used, either scintillators or Cherenkov radiators, are transparent to the wavelengths of photons that are most likely generated by their respective physical processes. It turns out this is a decent approximation for both the commercial scintillators chosen for investigation and the borosilicate glass used for Cherenkov instrumentation [6][4].

### Photon-detecting Elements

Particle detection methods relying on the generation of optical photons with particle hits play an important role in almost every potential instrument design surveyed through the course of this project. Several assumptions make simulation of the photon responses of these elements feasible:

Table 4.4: Photon Detecting Sensor Assumptions

#	Category	Sub-categories		Date	Assumption
4.1.1.0	Spacecraft Design	Detector	Cherenkov Radiator	28-June-2018	Cherenkov radiators will be made of borosilicate glass. Specifically: SCHOTT N-BK7.
4.1.1.1	Spacecraft Design	Detector	Optical Element	14-Sept-2018	Any optical element with dimensions less than 1 meter will exhibit no appreciable diminution of photon count compared to radiators of smaller dimensions.
4.1.4.0	Spacecraft Design	Detector	Scintillator	3-May-2018	Scintillators are made of a polystyrene base.
4.1.4.1	Spacecraft Design	Detector	Scintillator	3-May-2018	Scintillators will make use of PVT organic scintillator molecules.
4.1.4.2	Spacecraft Design	Detector	Scintillator	17-July-2018	Polystyrene will be used for material properties of scintillators where data is not available for PVT.
4.1.5.1	Spacecraft Design	Detector	SiPM	3-May-2018	SensL Inc. Designs shall be used for all SiPM modelling.
4.1.5.4	Spacecraft Design	Detector	SiPM	3-May-2018	Dimensions reported in SensL documentation for individual SiPMs are considered conservative and will be used without further addition of tolerances.
4.1.5.5	Spacecraft Design	Detector	SiPM	16-July-2018	SensL Inc. C-series SiPMs shall be used for all purposes requiring high-gain photon detection.
4.1.5.6	Spacecraft Design	Detector	SiPM	21-June-2018	Assume that contact between SiPM and optical elements is polished and coated with optical grease (this provides surface conditions for optical photon simulation in Geant4).

Borosilicate glass was chosen for the Cherenkov radiators (in 4.1.1.0) because it has a relatively similar refractive index to the acrylic or lexan plastics surveyed [4], and suffers little or

no material degradation under intense particle radiation, unlike virtually any polymer. This assumption however is not overwhelmingly firm. A plastic with a similar refractive index would also yield acceptable performance as a Cherenkov radiator, and would likely not degrade before the mandated bare minimum of 6 months. This is mentioned so that any future work that may be carried out on this subject is not tied to the choice for using borosilicate glass if a lighter material is indicated.

The next assumption (4.1.1.1) is essentially based around the fact that it is possible to simulate the more complex photon-transport behavior with many of the intricacies of the real world with Geant4, but that these intricacies do not appear to cause enough of a difference to justify their large computational expense. Simpler semi-empirical models were ultimately used to model the photon outputs of optical elements (both Cherenkov radiation and scintillation photons). These model were verified as described in the verification chapter, and the difference between Monte Carlo photon transport (at great computational expense) and the vastly faster empirical models was never more than a few percent.

The next 3 assumptions (4.1.4.0, 4.1.4.1, & 4.1.4.2) merely reflect the ready commercial availability of PVT based scintillators in a polystyrene matrix for instance from Eljen Technology or Saint Gobain Crystals [7] [6]. The real clincher, however, was the relatively high quality and availability of material and performance data from these aforementioned distributors. Where one cannot validate the performance of the instrument design, as in this project, the quality of the data used to simulate becomes the first priority in selection.

In a similar way, the next assumptions (4.1.5.1, 4.1.5.4, & 4.1.5.5) call out a particular manufacturer for the Silicon Photo-multipliers used for this project, SensL Inc. for two major reasons: they have excellent product performance data, and they have the single best system for purchasing small quantities of their detector elements for research purposes of any of the dozens of suppliers surveyed over the broader course of this project. The next two assumptions merely fill in inevitable gaps in the data that SensL provides.

Finally, during verification/calibration, optical sensor elements like scintillators and Cherenkov radiators were simulated with a full optical-photon transport simulation as aforementioned. This assumption (4.1.5.6) was only used during that phase, and constrains the optical boundary conditions surrounding the interface between the SiPM and the optical material it is aimed at.

### **Electronics and Semiconductor Elements**

While most of the electronics and support systems are covered by an earlier assumption to the effect that the entire spacecraft bus can be ordered retroactively once the instrument is designed, some specific electronics etc. are non-standard and relate specifically to the instrument itself:

Table 4.5: Electronics and Semiconductors Assumptions

#	Category	Sub-categories		Date	Assumption
4.1.2.0	Spacecraft Design	Detector	Electronics	2-May-2018	All relatively small IC chips will be assumed to have the mass and properties of silicon.
4.1.2.1	Spacecraft Design	Detector	Electronics	14-Sept-2018	Spacecraft electronics will be capable of yielding a minimum timing resolution of no more than 100ps.
4.1.2.2	Spacecraft Design	Detector	Electronics	14-Sept-2018	Effect of radiation disruption and damage on spacecraft electronics can be neglected
4.1.2.3	Spacecraft Design	Detector	Electronics	14-Sept-2018	Effect of temperature variations upon nominal performance of spacecraft electronics can be neglected
4.1.3.0	Spacecraft Design	Detector	PSD	2-May-2018	A custom 10X10mm PSD chip is manufacturable
4.1.3.1	Spacecraft Design	Detector	PSD	2-May-2018	The PSD chip mentioned in assumption 4.1.3.0 will have outer dimensions of 10.5X10.5X1mm with 0.5mm diameter pins.
4.1.3.2	Spacecraft Design	Detector	PSD	2-May-2018	A 2D array of the PSD chips mentioned in assumption 4.1.3.0 is manufacturable with 0.5mm spacing between the individual PSDs.

Within the detector, any element that interacts with the particles of interest was simulated. This includes the silicon chips of integrated circuit elements like the PSD arrays and any other ancillary electronics. As mentioned in the first assumption (4.1.2.0) these elements were modeled as solid, pure, silicon. Using the densest material commonly found in any IC chip is very conservative, but the thicknesses of the IC-chip analogs used in Geant4 is less than 0.25cm, and is therefore not a significant contributor to passive shielding.

The next assumption (4.1.2.1) regarding timing is perhaps the most critical constraint in the active shielding algorithm developed to filter out extraneous hits on the detector. 100ps resolution is extremely good performance by current standards, and while it has been demonstrated in the laboratory, such timing performance is still cutting edge [14]. To be clear, such timing is largely independent of the local spacecraft clock; commercially available space-rated computer clocks do not operate fast enough to provide this 100ps timing resolution. Therefore, an independent parallel timing circuit would be used to track the inter-stack triggering times at the 100ps level; this circuitry is assumed to closely resemble the NINO discriminator described by Anghinolfi et al [14].

Next, it is assumed (in 4.1.2.2) that the effect of permanent radiation damage and transient Single Event Effects outside the PSD arrays could be considered negligible. This is partially because tracking radiation damage is outside the scope of the thesis as discussed in the Introduction chapter, but mostly because there are few components used in spaceflight that have better flight heritage, or a higher TRL, than computer elements. As discussed in the Background chapter, the radiation environment in the Asteroid Belt is likely no worse than that for which most Earth-based space-rated computers are designed. Indeed, without the trapped radiation belts, and with a much lower overall flux of solar particles due to the larger distance from the Sun, it better in some ways.

The next assumption (4.1.2.3) is a simplifying one, pure and simple, that relates to a later assumption (4.2.4.0) on the thermal management of the spacecraft (namely that it is outside the scope of this thesis). The justification for this is simply that the thermal behavior of satellites is a non-trivial computational task, and the behavior of electronic components

in varying temperatures has often not been fully modeled, and requires physical testing to establish. Testing is not part of this thesis, and never was.

The remaining 3 assumptions (4.1.3.0, 4.1.3.1 & 4.1.3.2) regarding the geometry of the Position Sensing Detector were made in the absence of available data from industry regarding the manufacturability of custom PSD arrays. The dimensions and tolerances, however, are vastly greater than tolerances achieved on a regular basis for microelectronics, and are therefore assumed to be reasonable if passed to a subcontracted manufacturer.

#### 4.1.4. Spacecraft Design

This final list of assumptions, while similar in theme to the list of assumptions surrounding Detector Architecture is distinct in that these are aimed at the spacecraft system level instead of the instrument subsystem level.

Table 4.6: Spacecraft Design Assumptions

#	Category	Sub-categories		Date	Assumption
4.2.0.0	Spacecraft Design	General	Coordinate Systems	26-April-2018	XZ plane in coordinate system 1 defined as the side along which all standard CubeSat computer I/O pins are placed.
4.2.4.0	Spacecraft Design	General	Bus Systems	7-May-2018	Assume that no active heating or cooling elements are needed within the instrument itself.
4.3.0.0	Spacecraft Design	Shielding		24-April-2018	Shielding will have the same layering composition regardless of varying of other design parameters.
4.3.1.0	Spacecraft Design	Shielding		7-May-2018	Assume that shield mechanical failure or chemical degradation is negligible for the lifetime of the instrument (i.e. disregard).
4.3.2.0	Spacecraft Design	Shielding		14-Sept-2018	External shielding of sufficient thickness to stop high energy GCR primaries or muons is prohibitively massive. Therefore assume that external shielding configuration is of low priority and will remain sufficient only to stop low energy particles from solar wind, nuclear decay in Asteroid regolith, or low energy backscatter from Asteroid.
4.4.0.0	General Methodology	Preliminary Trade-off		4-May-2018	Assume approximately 10% error in mass estimates.

The initial assumption (4.2.0.0) regarding coordinate systems is simply based around the default coordinate frame used by Geant4. This was done purely for modeling convenience. Luckily, this reference frame is quite similar to vehicle-centered reference frames very commonly used in orbital applications.

It is, thereafter, assumed (in 4.2.4.0) that the instrument will require no active heating or cooling *internal to its volume*. There is a large amount of active electronics embedded within the instrument that will have exacting thermal requirements, but they are bonded to large, relatively decent, glass thermal conductors. Thus, as the instrument itself serves as a large heat sink, if the entire instrument volume is well insulated, and able to accept any heat inputs from outside its volume from the bus heaters, it is assumed that this is sufficient for thermal regulation in the cold space of the Asteroid belt. It should be noted that though

the above mentioned justification may be valid, there is no way to tell without very detailed thermal analyses that are beyond the scope of this project.

The next three assumptions (4.3.0.0, 4.3.1.0, & 4.3.2.0) regard the external shielding that surrounds the entire volume of the detector. The effect of the assumptions is firstly that the composition of this external shielding is not important enough to simulate in trade studies. This is simply because the particles of interest are extremely high energy and are not going to be stopped by anything less than dozens of centimeters of metallic shielding, let alone the less than 1cm that fits within the space allocated for shielding. The next assumption states that no mechanical or chemical degradation failures are expected. This is because all external shielding is aluminum, which does not degrade appreciably under particle radiation on the timescale of the required instrument lifetime [74].

The final assumption (4.4.0.0) regarding the error in mass estimates is merely an artifact of the difficulty in estimating uncertainty in mass modeling. Coupled with the fact that mass estimates were evaluated only in the preliminary trade study, it seemed reasonable to simply treat the mass estimate errors with a factor of safety, in this case of 1.1.

## 4.2. Requirements

Though, as mentioned several times throughout this report, this is not a formal design synthesis exercise, there are some basic requirements that can be formulated at such a preliminary stage. The following requirements are complementary to some of the assumptions made, but most are simply based upon standard practices from the NASA Systems Engineering Manual [67], and standard suggestions published in Wertz' SMAD [75]. No formal requirements-generation process was undertaken. Rather, a more real-life method was used. Where, in the process of undertaking modeling, simulation, or analytical tasks, should a useful potential requirement become obvious, it was included in the list of potential requirements, and thereafter audited several times to ensure that the original logic remained valid and useful. This informality was deemed valid for the low level of detail possible in Pre-preliminary design activities, like a Feasibility study. The method, in fact, was partially based upon the author's seven months of internship work with the systems engineering group of Sierra Nevada Corporation's Dream Chaser Spacecraft project.

A note on nomenclature: Throughout the documentation of mission requirements, the primary hodoscopic particle detector intended to collect data for muon tomography will be referred to simply as "the instrument." No other secondary payloads are explicitly covered in these requirements; though there would almost inevitably be more on a real trans-lunar mission.

### 1. Spacecraft Bus

- (a) Spacecraft bus shall be able to withstand no less than 2 years on station (not including all preceding transit time).
  - i. Active electronics within the Spacecraft bus will be rated for no less than full mission duration under established deep space radiation conditions
  - ii. All other components within the Spacecraft bus must be able to withstand no less than full mission duration under LEO radiation conditions and maintain nominal functionality.
  - iii. Spacecraft bus must be able to withstand no less than full mission duration under the worst thermal conditions expected during mission execution.
- (b) Spacecraft bus must provide sufficient internal regulation to comply with associated mission survival requirements, for both Spacecraft bus subsystems and the Instrument subsystems.

- (c) Spacecraft bus must provide sufficient power to the Instrument for it to operate in continuous data collection mode for no less than 90% of time on station.
- (d) Spacecraft bus must provide sufficient communication capability to transmit raw instrument data, and/or bus data, back to a ground station on Earth during any mission phase.
  - i. Communication system shall be designed to be able to communicate, at any mission phase, with a ground station capable of 70dB signal amplification. This receiver gain is based upon the capabilities of NASA's Deep Space Network.
  - ii. Communications system shall be designed to be able to transmit all instrument or bus data with a backlog of no more than one sidereal day at any given time during the mission.

## 2. Instrument

- (a) Instrument shall be able to successfully differentiate between muons and other radiation sources found in the mission environment.
- (b) Instrument shall be able to withstand no less than full mission duration on station (including all preceding transit time).
  - i. Active electronics within the instrument will be rated for no less than full mission duration under LEO radiation conditions.
  - ii. All other components within the Instrument must be able to withstand no less than full mission duration under LEO radiation conditions and maintain nominal functionality.
- (c) Instrument system shall exhibit maximum possible fault tolerance.
  - i. All fault intolerant subsystems and interfaces will be made redundant by design if possible

## 3. Mission

- (a) Mission boundary conditions will be based upon transit from Earth to the Asteroid Belt.
  - i. The outermost orbital radius around the Sun will be no more than 5 AUs.
  - ii. The innermost orbital radius around the Sun will be no less than 3 AUs.
- (b) Spacecraft shall comply with the launch compatibility requirements provided by the launch provider (currently NASA Launch Services Program)
- (c) Where not otherwise specified, spacecraft shall be compliant with NASA design standards in the NTSS system [9].

### 4.3. Preliminary Design Trade Studies

The primary purpose of the preliminary design trade studies was to systematically eliminate as many design variables as possible from the necessity of future consideration. In other words, the purpose of this study was to rationally narrow down the field of designs that were obliged to be subjected to simulations as much as possible.

#### 4.3.1. High Level Trade Study

Starting with the information gathered in the literature study that preceded this thesis project, one of the largest tasks of this initial trade study was simply to compile a list of potential detection techniques. Because it was explicitly treated in the literature study, only the results of that original survey will be reported here:

Cherenkov detectors including both counters and ring-imaging Cherenkov detectors (RICH), scintillators, and semi-conductor based position sensors were narrowed down as the detection options that should be investigated further [41].

The first step of the initial design trade study performed was simple combinatorics for the detection techniques just mentioned; namely, it was desired to eliminate any combinations of techniques that did not provide sufficient data to meet instrument requirements. The initial combinatorics are summarized in the following figure:





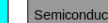
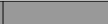












Design		Key
1	NON FUNCTIONAL <sup>1</sup>   	Scintillator
		Cherenkov
2	NON FUNCTIONAL <sup>2</sup>   	Semiconductor
3	NON FUNCTIONAL <sup>3</sup>   	
4	  	
5	NON FUNCTIONAL <sup>1</sup>   	
6	  	
7	  	
NOTE: Relative magnitude of color bars are meaningless in this table; only combinations matter.		
1. Neither the semiconductor/scintillator design provide good characterization of velocity		
2. Pure Cherenkov design doesn't provide info on E, dE/dx, or M		
3. The purely semiconductor design is rated not functional because it likely does not offer any possibility of information about particle identification		

Figure 4.1: Graphical representation of possible combinations of detection schemes, and initial round of design combination eliminations.

As is clearly shown in this graphic, of the 7 permutations of differing detection scheme combinations, only three were eventually passed to the next level of discrimination. It should be noted that the primary evaluation criteria, as noted in the graphic itself, are based in the type of data that the instrumentation combination could collect. These data types are summarized in the following figure, which was generated from data collected in the literature study [41]:

	Velocity	Energy	dE/dx	Trajectory	Charge	Mass
Scintillating Counter	Yes <sup>1</sup>	Partial <sup>2</sup>	Partial <sup>3</sup>	No	No	No
Scintillating Fiber	Yes <sup>1</sup>	Partial <sup>2</sup>	Partial <sup>3</sup>	Yes	No	No
Cherenkov Threshold Counter	Yes	Partial <sup>4</sup>	No	No	Yes	No
Cherenkov Ring Imager	Yes	Partial <sup>4</sup>	No	Yes	Yes	No
Semiconductor	Yes <sup>1</sup>	No	No	Yes	Yes	No
Scintillating fiber + Cherenkov counter	Yes	Partial <sup>5</sup>	Partial <sup>3</sup>	Yes	No	No
Scintillating Fiber + Semiconductor	Yes <sup>1</sup>	No	Yes	Yes	Yes	No
Cherenkov Counter + Semiconductor	Yes	Yes	Yes	Yes	Yes	No
Cherenkov counter + Scintillating counter + Semiconductor	Yes	Yes	Yes	Yes	Yes	No
1. With 2+ detectors and TOF measurement						
2. Light output ~ proportional to energy BELOW a certain energy threshold around 1-10 GeV						
3. Birks Law provides a means of computing dE/dx below the energy threshold mentioned in 2						
4. Particles below a certain E are excluded						
5. Velocity from cherenkov, weak dE/dx characterization from scintillator.						

Figure 4.2: Tabular survey of the types of characterizing particle data that can be directly gathered or indirectly extrapolated from the various detection schemes

Scrutiny of the above figure reveals one of the critical problems that has persisted throughout the entirety of this project: namely that the collection of particle data at very high energies is difficult, especially with smaller detector geometries without the mass budget to include lead layers as would be more commonly found in a calorimetry instrument like CREAM [11]. Muons of sufficient energy to transit larger swathes of rock are almost exclusively above 1 GeV in energy [61]. Galactic cosmic ray primaries are also very commonly in excess of 1 GeV [17]. Both Cherenkov radiation and Scintillation display a plateau in the number of photons they generate relative to the kinetic energy of the incident particle. Particles above this energy no longer cause any increase in photon count. See the verification chapter to observe this effect treated graphically. This saturation effect makes it difficult to collect enough unique data about very high energy transiting particles in the detector to effectively discriminate.

Thus, the most useful conclusions derived from this initial trade study were ancillary to the elimination of detection schemes; namely that a combination of data types (columns in Figure 4.2) was necessary for any particle filtering algorithm. Specifically, it was determined that the most likely combination of data types that would prove definitive would be any two of: particle kinetic energy + velocity, energy losses (dE/dx), or mass, or a combination of velocity, energy losses, and charge. Ideally the former combination would be available, because it yields the strongest definitive identification parameters. These data needs were used to undertake the preliminary elimination of possible detection schemes in Figure 4.1.

It should be noted that the conclusions of this study were updated with retrospectively gathered information and results generated in the intervening time, but that these updates do not include the deletion of conclusions that were later disproved. For instance, as has probably been evident in reading this report so far, some of the data types in Figure 4.2 turned out to be uncollectable by any of the detector schemes tried (dE/dx, kinetic energy, and particle mass have turned out to be beyond the reach of any of the instrument designs surveyed). However, it was deemed that the design narrative proceeded most logically if organized in a more chronological manner whereby information and trade study results are still included even if they are outdated because they offer valuable procedural information.



### 4.3.2. Mid Level Trade Study

#### Modeling

The mid-level trade study, implemented at a level of detail much greater than that of the initial trade study, in addition to providing further design eliminations, resulted in the identification of several critical design parameters that were later used in the detailed final trade study. This is because at least some of the metrics against which the design options were evaluated were based on parametric models of the instrument design itself. It is, therefore, perhaps useful to note that this was the stage of the design where instrument modeling began in earnest. From a procedural perspective, this trade study was intended to narrow the design down to the point where essentially everything BUT particle radiation and simulation parameters had already been fixed. Thus, the final trade study could focus solely on simulated detector performance characteristics.

The entire spacecraft and instrument were modeled based upon functional flow block diagram (FFBD) standards from the NASA Systems Engineering Handbook [67]. The first model generated was a functional diagram describing the context of the spacecraft and instrument interface. This model diagram was used as the primary interface control document, used where it was necessary to derive boundary conditions that may be changed or provided by the spacecraft bus.

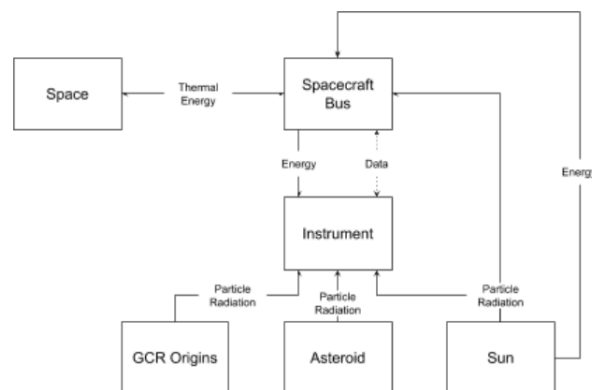


Figure 4.3: Model of instrument in the context of both environment and the associated spacecraft bus

The functional model for the spacecraft bus itself was derived from a basic, generic, bus model similar to those discussed in the Space Systems Engineering course offered in the 2016-2017 academic year at TU Delft. The bus model reflects the associated assumptions and requirements:

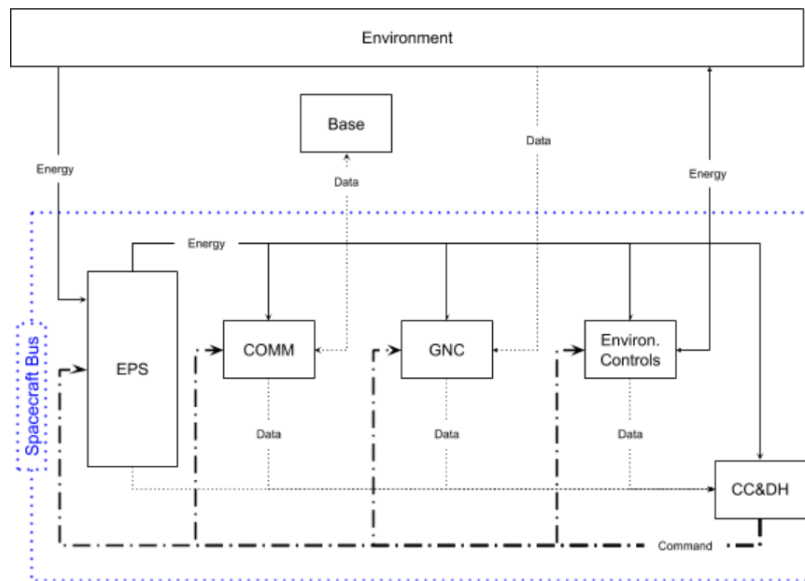


Figure 4.4: Generic Spacecraft bus model used to constrain boundary conditions affected by, or determined by, the support bus associated with the instrument

The three major detection schemes resulting from the first, high level trade study were further subdivided into combinations of practical technologies. The categorical subdivisions are tabulated below; each one represents one instrument model that was evaluated in the mid-level trade study.

It should be noted that an additional variable was added for the mid-level trade study analysis: number of stacks. It is further necessary to point out that simulation results intervening between the mid level trade off and the final trade off served to constrain the number of stacks in a definitive way that was not possible at the time of execution for the mid-level trade off study. The number of stacks, therefore was *not* eliminated as a variable in this trade study as was originally thought. The number of stacks was treated again in the final design trade study. However, the original results are included in this section as before, in the interest of fully documenting the design-narrative of this feasibility study.

Table 4.7: Mid-level Trade off Design Options

Option #	Detection Scheme	# Stacks
1A	SC + CC + PSD	2
1B	CC + PSD	2
1C	CC + SFP	2
2A	SC + CC + PSD	3
2B	CC + PSD	3
2C	CC + SFP	3
3A	RICH + PSD	2
3B	RICH + SFP	2

The design options in the above table were modeled using the same FFBD technique used for the spacecraft bus above. For option category 1 and option category 2, the functional diagrams are combined because the only difference is the number of stacks:

The following instrument design options make use of a ring imaging Cherenkov detector architecture. These detectors have a few advantages over simple monolithic Cherenkov radiators or a grid of "paddles". They are able to capture information on the photon "shock-cone" characteristic of the Cherenkov effect, and thereby can gather high quality information on particle velocity independent of timing.

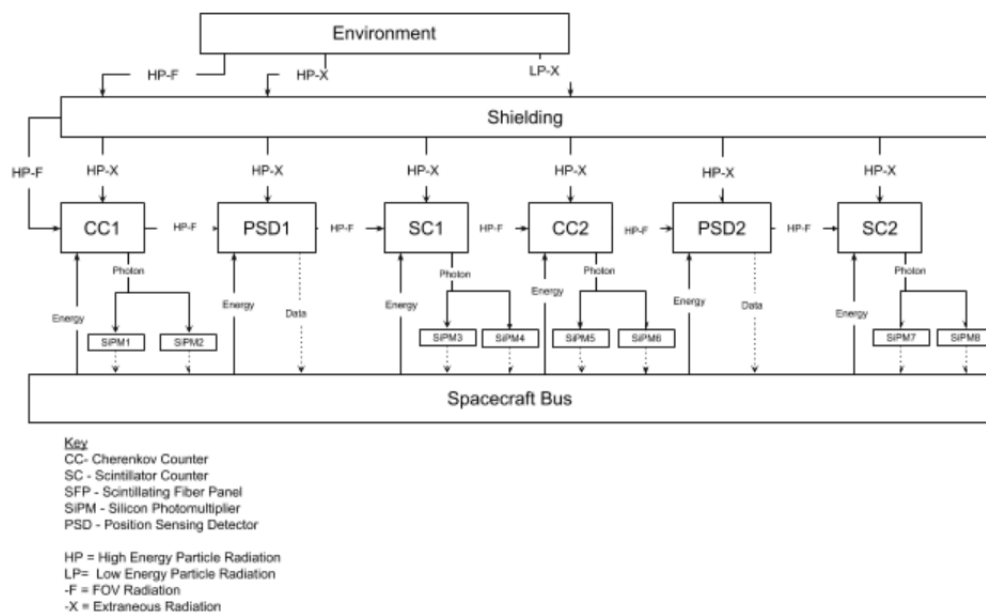


Figure 4.5: Functional model for options 1A and 2A: A hodoscopic instrument using a combination of monolithic Scintillator, monolithic Cherenkov, and semi-conductor PSD detectors

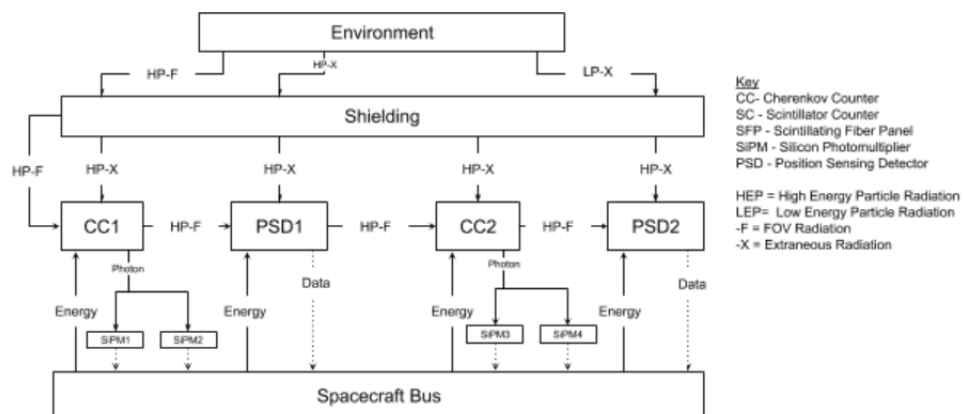


Figure 4.6: Functional model for options 1B and 2B: A hodoscopic instrument using a combination of monolithic Cherenkov and semi-conductor PSD detectors

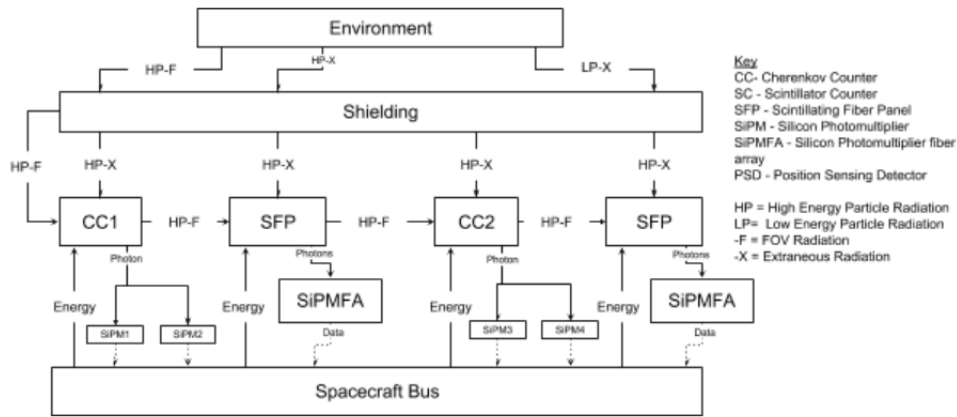


Figure 4.7: Functional model for options 1C and 2C: A hodoscopic instrument using a combination of monolithic Cherenkov and scintillating fiber panels

It is worth noting, in retrospect, that the simulation of a RICH-based detector would likely be computationally very expensive using the existing Geant4 framework. This is because such models would be obliged to track optical photons in a way that the final baseline simulation models do not (see simulation chapter for information on the calibration of semi-empirical photon generation models for both scintillation and Cherenkov effect). Furthermore, the practical reality of constructing such an instrument present significant challenges; not the least of which are the optics itself, which are effectively absent in the purely stack-based instrument designs. However, despite all of these facts, a miniaturization of such an instrument has never been attempted before, and may, indeed, prove to be the only type of instrument surveyed that has the possibility to function with a CubeSat form factor and mass budget.

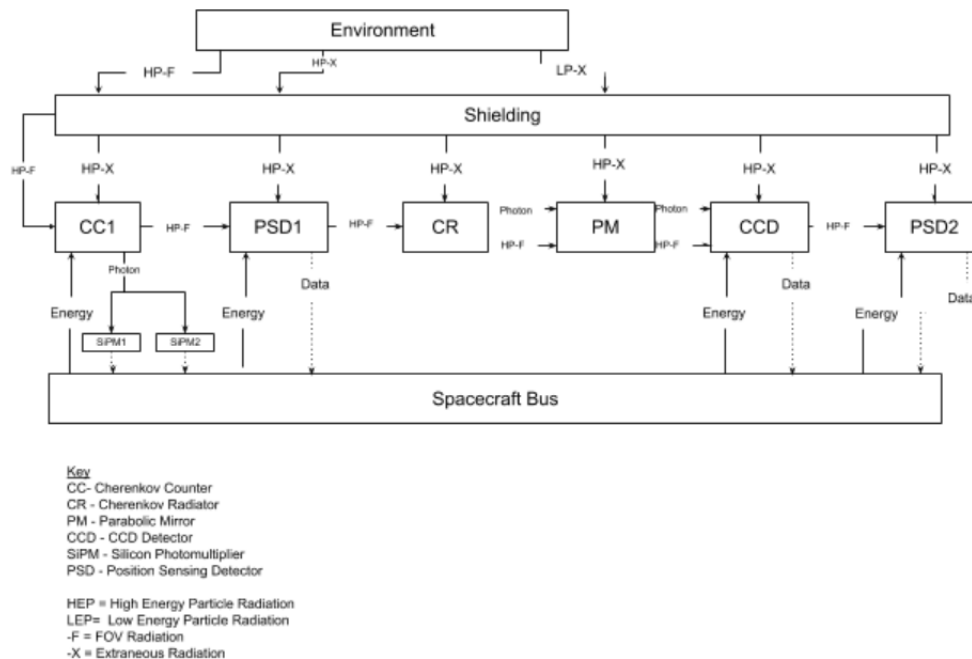


Figure 4.8: Functional model for option 3A: A hodoscopic instrument using a combination of RICH and PSD

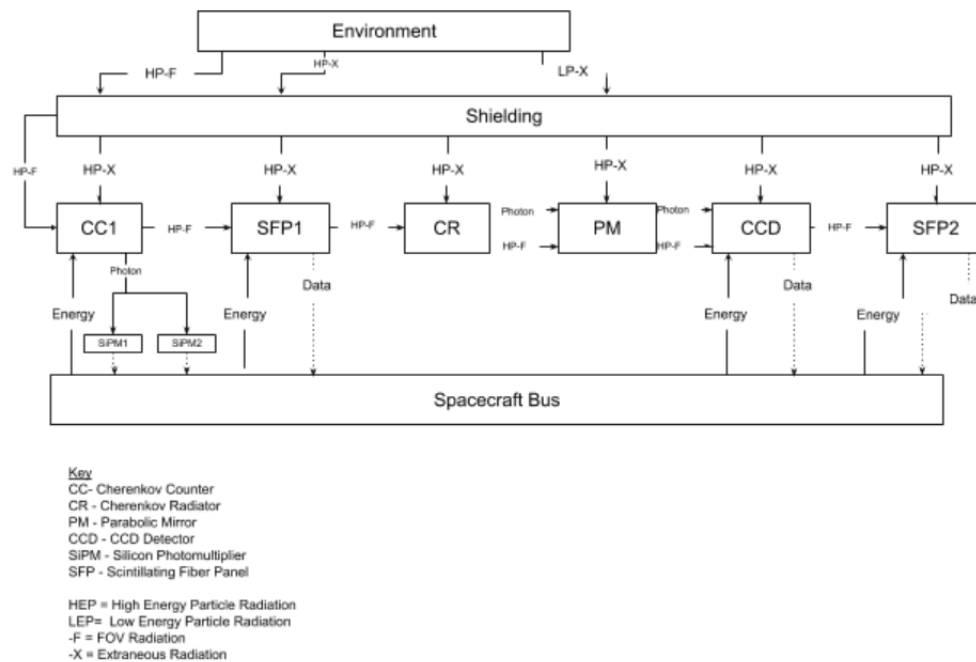


Figure 4.9: Functional model for option 3B: A hodoscopic instrument using a combination of RICH and scintillating fiber panels

## Evaluation

The designs detailed in the previous subsection were evaluated based upon a number of performance characteristics that do *not* include detector performance or other metrics that depend upon radiation analyses. Those were reserved for the final trade study. A list of the evaluation parameters is tabulated below:

Table 4.8: Mid Level Trade off Evaluation Criteria

#	Evaluation Criterion	Unit
1	# Stacks	
2	Total Volume	CubeSat Volume Unit
3	Estimated Mass	g
4	# SiPMs	
5	# Active Sorting Channels	
6	# Independent Detection Methods	
7	# Fault Intolerant Paths	
8	# Sensor Pins (raw number)	
9	# Custom Detector Components	
10	# Custom Subsystems	

These criteria were chosen to minimize the amount of qualitative assessment inherent in the final trade off method, and were ultimately derived from requirement 2C (fault tolerance), and requirements 3B and 3C (compliance with NASA technical standards / guidelines). Remaining *functional* requirements all deal either with mission planning, which as been assumed to be largely outside the scope of this project, or with behavior that can only be measured with simulations. The latter such requirements are treated in the final design trade off.

Of the two requirements from which the evaluation parameters were derived, fault tolerance was by far the more important. This is, generally, because without simulation results, it is somewhat difficult to compare the effectiveness of different sensor physics beyond the coarse assessment initially done in the high level trade study. Where design options do not directly

present obvious differences in detection performance at this stage (functional blocks in FFBD model diagrams), they do present an opportunity to develop subsystem level fault tolerance (from the interfaces between blocks in the FFBD model diagrams). The remaining parameters (mass, volume, # Independent Detection Methods, # Custom Detector Components / Subsystems) are based upon parameters common to most evaluations of most space-borne instruments as outlined by the NASA Systems Engineering Handbook [67]. They are counted as less important because mass and volume, in particular, are parameters that are extremely difficult to accurately predict so early in the design process.

There are a number of methods for analyzing fault tolerance, most requiring an extremely detailed functional model and validated understanding of real-world behavior. Neither of these are particularly useful in a feasibility study which benefits most from a breadth of possible design options, and less from the extreme depth of modeling for each potential option. It simply does not make sense to expend a great deal of effort on designing a host detailed instruments to be evaluated at such an early phase. Thus, a compromise was reached, and the functional models generated for each of the options were used to compile the total number of fault intolerant functional paths. A path (designated by a line with an arrow in the FFBDs above) was considered fault intolerant if, when compromised, it totally disrupts the underlying function of the detector, which is simply: to detect muons. This level of qualitative fault tolerance analysis would obviously not stand up to the rigors of industry standard, but provides an excellent metric for both how difficult a design would be to develop, and, qualitatively, how likely it is to break down after launch. In essence, design options with a large number of fault intolerant paths are considered worse than those with a small number.

However, in part because of the qualitative nature of much of this analysis, a method known as Analytical Hierarchy Process was used to evaluate the options [63]. This method, not detailed here, is essentially the same as a Pugh Matrix except the criterion weighting factors are rendered less subjective by basing them on a simple user ranking of criterion importance in numerical order. This does not remove the subjectivity of ranking one criterion more important than another, but it does remove the subjectivity of arbitrarily choosing a weighting factor to quantify that ranking. The AHP matrix used to determine these weighting factors is included in the appendices, the methodology is that originally published by Saaty when the AHP method was invented [63]. The results of the subsequent Pugh-style trade-off analysis using the AHP criterion weighting factors can be seen in the following figure:

		Design																								
Criterion	Weight Factor	1A			1B			1C			2A			2B			2C			3A			3C			
		Crit.	NORM	Score	Crit.	NORM	Score	Crit.	NORM	Score	Crit.	NORM	Score	Crit.	NORM	Score	Crit.	NORM	Score	Crit.	NORM	Score	Crit.	NORM	Score	
Total Instrument Volume	#Stacks	0.11	2.00	0.67	0.07	2.00	0.67	0.07	2.00	0.67	0.07	3.00	1.00	0.11	3.00	1.00	0.11	3.00	1.00	0.11	2.00	0.67	0.07	2.00	0.67	0.07
	Estimated Mass	0.16	1.50	0.75	0.12	1.00	0.50	0.08	1.25	0.63	0.10	1.75	0.88	0.14	1.50	0.75	0.12	2.00	1.00	0.16	1.25	0.63	0.10	1.75	0.88	0.14
	# SIPMs*	0.25	612.00	0.54	0.13	460.00	0.41	0.10	752.00	0.67	0.16	920.00	0.81	0.20	690.00	0.61	0.15	1130.00	1.00	0.25	682.00	0.60	0.15	1031.00	0.91	0.23
# Active Sorting Channels**	# SIPMs*	0.03	8.00	0.67	0.02	4.00	0.33	0.01	4.00	0.33	0.01	12.00	1.00	0.03	6.00	0.50	0.01	6.00	0.50	0.01	2.00	0.17	0.00	2.00	0.17	0.00
	# Active Sorting Channels**	0.07	3.00	0.33	0.02	2.00	0.50	0.03	2.00	0.50	0.03	3.00	0.33	0.02	2.00	0.50	0.03	2.00	0.50	0.03	3.00	0.33	0.02	3.00	0.33	0.02
	# Independent detection methods***	0.10	3.00	0.33	0.03	1.00	1.00	0.10	1.00	1.00	0.10	2.00	0.50	0.05	1.00	1.00	0.10	1.00	1.00	0.10	2.00	0.50	0.05	2.00	0.50	0.05
	# Fault Intolerant Paths	0.11	3.00	1.00	0.11	3.00	1.00	0.11	3.00	1.00	0.11	2.00	0.67	0.07	2.00	0.67	0.07	2.00	0.67	0.07	2.00	0.67	0.07	2.00	0.67	0.07
	# Sensor Pins (Raw number) ****	0.03	1056.00	0.22	0.01	1048.00	0.22	0.01	3224.00	0.67	0.02	1608.00	0.33	0.01	1572.00	0.33	0.01	4836.00	1.00	0.03	1046.00	0.22	0.01	3222.00	0.67	0.02
	# Custom Detector Components	0.06	0.00	0.00	0.00	0.00	0.00	0.00	1.00	0.50	0.03	0.00	0.00	0.00	0.00	0.00	0.00	1.00	0.50	0.03	1.00	0.50	0.03	2.00	1.00	0.06
	# Custom Subsystems	0.08	1.00	0.50	0.04	1.00	0.50	0.04	1.00	0.50	0.04	1.00	0.50	0.04	1.00	0.50	0.04	1.00	0.50	0.04	2.00	1.00	0.08	2.00	1.00	0.08
	Total Score				0.56			0.55			0.69			0.68			0.65			0.85			0.59			0.76
	* Assume 2 SIPMs per detector/for redundancy see assumption 6.0																									
** +1 for every detector capable of independently determining particle V or dE/dx or E or M																										
*** Each different physical phenomenon or set of physical phenomena that can be used to accurately discriminate muons (i.e A+B+C with A+B and B+C being 2 independent detection methods																										
**** Number of pins of each individual sensor component (i.e. these will need to be wired together in various data collection buses to accommodate the large number of pins																										

\* Assume 2 SIPMs per counter for redundancy see assumption 6.0

\*\* +1 for every detector capable of independently determining particle V or dE/dx or E or M

\*\*\* Each different physical phenomenon or set of physical phenomena that can be used to accurately discriminate muons (i.e. A+B+C with A+B and B+C being 2 independent detection methods)

\*\*\*\* Number of pins of each individual sensor component (i.e. these will need to be wired together in various data collection buses to accommodate the large number of pins).

NOTE: This AHP is based upon the lowest possible score being desirable. Thus normalizations were performed to ensure that the relative merit of each score yielded an appropriately low or high score.

Key  
Less is better  
More is better

Figure 4.10: Results of the AHP/Pugh trade off study using non-particle radiation parameters

Three of the evaluated design options were relatively close in their performance in this design trade study: 1A, 1B and 3A. The first two performed well because of the inherent simplicity of their design, and the relative robustness of the Cherenkov Counter + PSD combination in particular. The remaining option, a RICH detector, was a bit of a surprise, but reflects the uniquely high quality data that such a detector produces compared with simple stacked or gridded monolithic detector elements.

It is necessary to point out a few key points here, in retrospect, and with relation to the re-

mainder of the project. Firstly, while many of the evaluation criteria included in Table 4.8 were later revealed to be less relevant, or, occasionally, irrelevant, the most important criteria remain sound. Namely the evaluation of fault tolerance, and the robustness of the data generated by the instrumentation schemes evaluated against their value in an active shielding algorithm. Thus, though factors like mass, volume, and number of stacks were eventually thrown out as critical criteria for this feasibility study due to the discovery of new data or the reevaluation of old results in light of new results, one of the three designs chosen: 1B, eventually became the baseline of the final design selected in the ultimate trade study. In brief, new data has rendered a fair portion of the evaluation criteria used for this mid-level trade off irrelevant, but the strongest evaluation criteria remain valid, and the overall result of this trade off wound up being forward-selected in later study.

### 4.3.3. Implication of Initial Simulation Results

As mentioned in the previous subsection, there were a number of results that arose during the intervening time between the mid-level trade off study and the final trade off study as a natural byproduct of Geant4 model development, verification, and calibration activities. These results are, regrettably, not particularly systematic in nature, and do not fit well into classical design progression, but they did prove critical in the evolution of the instrument.

Firstly, design 1A, including Cherenkov Counter, Scintillation Counter, and PSD, was eliminated. This was by the simple expediency of scintillators proving to be computationally expensive to simulate, rife with far greater uncertainty in simulation results than Cherenkov simulations, and of inherently limited value at higher particle energies due to the aforementioned saturation of the scintillation effect at high kinetic energies of incident particles.

Ultimately, it must be pointed out that scintillators were eliminated based upon an unvalidated simulation result (though the underlying physics of the simulation were *verified*). This is a recurring theme that dogs this entire thesis: the lack of experimental data in instrument design. Therefore, though it was necessary to eliminate scintillators from the list of design options to be evaluated in the final study, this does *not* necessarily indicate that any future work on this project should avoid the investigation of scintillators. This elimination came down to a practical need to simplify a simulation complexity.

Next, design 3A, including a RICH detector and PSD, was eliminated for very similar reasons. It became necessary to model the optics of such a design. These instruments most often utilize a parabolic mirror of some description to reflect the characteristic rings that result as a Cherenkov photon cone strikes some arbitrary optical plane [27]. It turns out that implementing a parabolic mirror in Geant4 is quite complex, requiring a GDML interface. Implementing a spherical mirror is much easier, but then introduces the difficult-to-quantify error of spherical aberrations. Neither option was acceptable; the first because GDML is preclusive to the type of parametric study utilized in the final design trade off, and the second because correcting for spherical aberrations in the custom optics of a custom instrument could easily represent a thesis project on its own. Furthermore, if such a detector was used, it would be obliged to use full optical photon simulations. As mentioned in the Simulation chapter, using such an option increases the number of particles that must be modeled and tracked by at least two orders of magnitude. This would cause memory overflow in any simulation of even mild complexity even for less-complicated geometries than a RICH detector.

However, as aforementioned, RICH detectors offer unique data gathering opportunities because they are sensitive to not just photon counts but to the geometric data of the photon cone itself. The results of the final parametric study indicate that, though design 1B can prove at least acceptably capable of detecting muons, it cannot very well do so in a small CubeSat format. Thus, the RICH detector could very possibly remain the best option for very small instruments. It has also, at least as of the time of the submission of the literature study that preceded this report, never been attempted before [41].

Thereafter, the next major development was an upgrade in Model 1B: changing the monolithic

Cherenkov radiators into a grid of "paddles". This is best illustrated by the blue-lined volumes in the following image of the baseline parametric model used for part of the final design trade study:

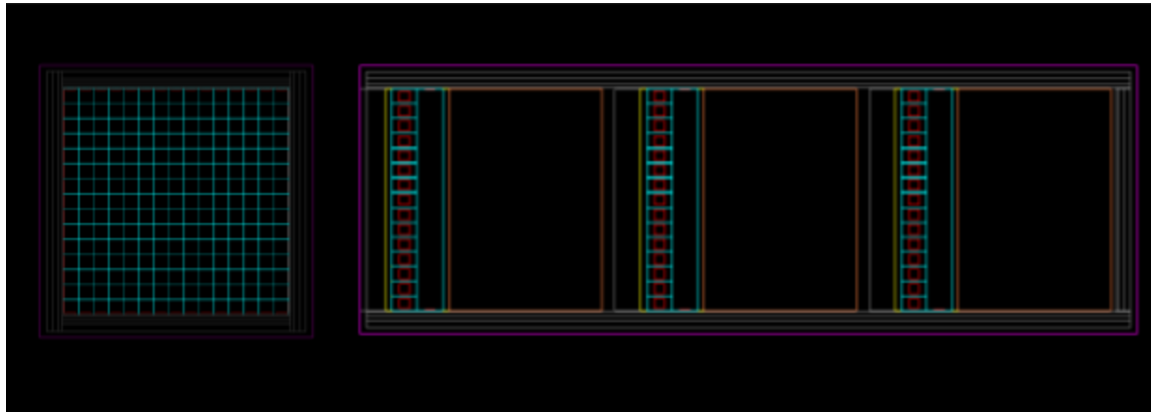


Figure 4.11: Cherenkov Paddle Grid Configuration

This increased "resolution" in the Cherenkov counter data turned out to be necessary because monolithic counters yielded extremely confused photon counts whenever struck by more than one particle in a hadronic or EM cascade. Results presented in both the Simulation and Verification chapters show that, on average, no fewer than 10% of the incoming GCR primary particles of at least 1 GeV induced hadronic showers through the instrument, and it was far more common for higher energy primaries. By breaking the monolithic Cherenkov radiator up into a grid, it was possible to discriminate between a far higher proportion of the simultaneous hits on one hodoscope plane subjected to a hadronic or EM shower. It is, of course, still possible that more than one particle in a cascade could hit a pair of paddles (combining to form a "grid" element) but far less likely. In practice, increasing the resolution of the Cherenkov layers from 1 to 225 "pixels", in combination with the aforementioned array of PSDs included in every layer, allows fairly good filtering of all but the primary trajectory with the existing active shielding algorithm. More quantitative details on that will be provided in the section devoted to the final trade study.

Finally, a fairly simple change was made to the PSD arrays. As detailed in the assumptions list, an array of approximately 9X9 PSD "pixels" of approximately 10X10mm will be used to capture high accuracy geometric data of particle strikes on each stack plane. The Cherenkov paddle grids, by comparison, yield only very coarse strike-coordinates with an error upwards of an order of magnitude higher than PSDs. It was found that two such PSD arrays per stack, effectively sandwiching the Cherenkov paddle grid layer, provided a larger amount of strike coordinate data, thereby allowing better elimination of secondary particles with a large angular deviation from the path of the primary.



## 4.4. Final Design Trade Study

### 4.4.1. Active Shielding Algorithm

The active shielding algorithm is arguably one of the most important elements of a successful detector under these conditions. Specifically, when searching for high-energy particles, it is necessary to be able to distinguish them from the equally high energy background radiation of Galactic Cosmic Rays that is ubiquitous throughout the solar system (and, presumably, galaxy). The active shielding algorithm implemented here, essentially a data-filtration method, is very basic. As will be discussed in the immediately following sub-sections, this basic algorithm still managed to achieve an ID rate of about 72% for the high energy muons that are the target of this project, but this margin could, undoubtedly, be improved. It is, perhaps, useful to reiterate the fact that, in the very narrow microcosm of the application detailed in this thesis, namely of an instrument orbiting an Asteroid in close proximity, this 72% ID rate is acceptable. That is because the ID rate was computed in a worst-case-scenario simulation with a far higher level of background noise in the field of view of the instrument than turned out to be realistically expected. For further details on the details of this particular boundary condition, see the Simulation chapter section on Asteroid Environment.

This basic active shielding algorithm makes use of principally geometric analyses of incoming particle trajectories. To successfully pass this filter, an incoming particle must:

1. Pass through all sensitive planes
2. Produce a clean hit in the foremost PSD plane (i.e. have generated no secondary particles before striking the first PSD plane).
3. Pass through the instrument from front to back. In effect, this implies that the incoming particle must be within the field of view of the instrument as determined by the aspect ratio.
4. Have a trajectory that is mostly linear
5. Yield a Cherenkov photon count in at least one layer that is above saturation (the material of the Cherenkov radiators was partly chosen so that the photon saturation point for photon count corresponded to most of the particles of interest at energies greater than about 1 GeV)

Basic indeed, but unfortunately, one of the reasons that no more sophisticated algorithm was developed was because the evaluation of even these simple criteria with the available data turned out to be complex.

### Raw Data Pre-processing

It is necessary to start by mentioning that the raw data output by Geant4, hereafter referred to as "omniscient" data, records every particle event in any sensitive detector volume in the entire instrument model. It would be trivial to detect muons using this data because Geant4 also directly provides the particle identity. Thus, it was necessary to process the raw data from Geant4 into a form that at least approximates what real instrument raw-data might look like. This final simulated "instrument raw data" takes the form of a data array where each row corresponds to an event timestamp, and each column corresponds to the respective detector volumes where the primary data collected by said detector volumes is inserted into the cell. It is important to note that the rawest form of instrument data would take the form of sensor voltages. This level of simulation was deemed not worth the effort because it would be based on published values of sensor performance, and any prototype would have to undergo testing regardless of what prior simulations had been performed; most likely not even using any such direct voltage simulation results.

The primary task of this raw-data processing was to take the highly unordered timestamps of the raw Geant4 data, bin them into discrete events, and then within each binned event, bin all events yet again using the minimum timing resolution of 100ps mentioned in the assumption

section earlier in this chapter. This means that if two particle events (for instance, a pair production event) in the raw Geant4 data occurred close enough together in time that the time difference was less than the minimum timing resolution, any photon results would be added together, and any position results would be kept separate. This was accomplished by a somewhat customized application of MatLab's built in histogram and discretize functions.

#### Algorithm: Direction Check

The first two listed checks in the active shielding algorithm, listed above, namely ensuring that all three sensitive planes were, indeed, activated in the correct order in any candidate particle event, was, perhaps, the simplest. Using the aforementioned processed "raw data," each clumped particle event was checked over firstly to ensure that all three planes had been activated, and secondly to for direction.

At face value, this direction check was merely a matter of ensuring that the particles in any event were activated in the correct sequence, from fore to aft. Given the non-simultaneity assumption mentioned in the previous section on Assumptions, where it is assumed that simultaneous particle events (that is events that are indistinguishable within a 100ps timing resolution), are rare enough to be negligible, this would have been straightforward except for the very high probability of secondary production for such high energy incident particles.

To discriminate between primary and secondary, this algorithm relies heavily upon the foremost PSD plane's timing capacity. By simple geometric principles, the probability of secondary production increases with the amount of material that must be traversed by the incident particle. Thus, the foremost PSD plane is the most likely to be hit *only* by the primary and none of its secondaries. Thus, the evaluation of hit timing was referenced upon this plane's time stamp. If there was some kind of particle event on the succeeding planes at a regular interval (i.e. the time of flight between plane 1 and plane 2 was roughly equal to that between plane 2 and plane 3), the particle event was passed through to the next step.

#### Algorithm: Linearity Check

The next check was for linearity. This is based upon the fact that muons have the lowest scattering cross section of most of the charged particles that were recorded in any simulation involving the detector. They are, therefore, least likely to be deflected. While this does not, by any means, indicate that a proton or an alpha particle couldn't traverse the instrument volume undeflected, this check was also necessary because, without the ability to determine the point at which deflection occurred, non-linear results introduce an unacceptable level of uncertainty into the hodoscopic measurement of incidence angle.

Both electromagnetic and hadronic showers are largely characterized by a cone shape where most secondaries travel in much the same direction as the primary with little divergence. While this cone is, by no means, perfect, the primary particle trajectory, where it does not decay or become deflected, remains close to the center of said "cone"; this information was derived from Geisser's discourse on the shape of air showers [34]. Thus, starting from a clean hit on the foremost PSD plane, all of the XYZ coordinates of hits in following, PSD planes were used as points in a 3D Orthogonal Distance Regression. That is to say, the first likely primary hit was then checked against all subsequent hits for linearity. The algorithm used was adapted from an ACS paper on the subject [60]. It is briefly outlined here:

1. Arrange all points into a  $N \times 3$  matrix,  $A$ , with  $X$ ,  $Y$  and  $Z$  coordinates in each of the three columns
2. Generate a vector of means for  $X$ ,  $Y$  and  $Z$
3. Subtract each overall coordinate mean from each of the respective  $X$ ,  $Y$  and  $Z$  values in the original matrix,  $A$ .
4. Perform Singular Value Decomposition on this new subtracted matrix (note this was simply accomplished by using a built-in function in MatLab: "svd")

5. The resulting vector is the direction of the orthogonal regression line.

The coefficient of determination ( $R^2$ ) of the fit was determined by taking the average of the diagonal of the covariance matrix also generated by singular value decomposition. This metric was used to assess linearity and throw out deflected or "dirty" hits with a number of secondary-hit-points that threw the inversion residual out of whack. The minimum  $R^2$  value was chosen to be 0.8. In a pre-check before the parametric studies performed in the final trade analysis (detailed in the next section), this linearity value was varied between 0.6 and 1.0. The value of 0.8 was the best compromise between eliminating too many hits, and not serving any "filtering" value at all. It provided, in other words, the local optimum of the muon detection efficiencies for each of the aforementioned values tried. It must be noted that this check was performed with a perfectly orthogonal test beam incidence angle, and a 25% muon proportion.

It must, further, be noted that this metric is inherently based upon choosing the lesser of evils (i.e. the  $R^2$  value that throws out the least good hit candidates).

#### **Algorithm: Photon Check**

The final major check in this "particle filtration" algorithm was to ensure that the particles had a charge, and, if muons, were of sufficient energy to have transited the asteroid. This was based upon a useful muon range of 1-1000+ GeV proposed by Prettyman et al [61]. This was very easily accomplished. As mentioned in the Simulation and Verification & Validation chapters, the Cherenkov effect exhibits plateau in the number of photons generated past which all higher energies still produce much the same photon count. This "saturation" level is dependent upon the refractive index of the material in question, and was part of the reason that borosilicate glass was chosen for the Cherenkov radiators. More detail on the physics of this effect can be found in the Background and Simulation chapters.

Ultimately, if the particle had sufficient kinetic energy (above 1-5 GeV, depending on incidence angle) to saturate *all* of the Cherenkov grid layers that it passed through, it was accepted.

#### **Algorithm: Testing**

As mentioned before, Geant4 provides all of the data that hits any sensitive detector volume upon request. This omniscient data was used first to check that the raw-data pre-processing did not throw out any particle events that it should not have, and second to provide an high-level empirical assessment of the performance of the active shielding algorithm itself.

This latter point is critical: by checking the number of positive muon identifications thrown by the shielding algorithm against the number that Geant4 actually injected, it is possible to define a metric that will be called hereafter the "Muon Identification Probability" (MIDP). This is simply the ratio of positive muon hits given by the algorithm process compared to the number of hits that actually happened. This metric is, in essence, the probability that a positively recorded hit is, in fact, a muon. It varies depending upon a number of design parameters. Several of the most readily changeable (with respect to real life design constraints) were varied in two parametric studies described in the following section. This metric is important because it allows empirical assessment of the behavior of the shielding algorithm. That is, it allowed a backwards approach where, instead of struggling with very complicated signal processing and detector physics, it was possible to make a trial algorithm and simply skip straight to the end metric of its performance. This was, in fact done, in an informal way with a few separate candidate shielding algorithms. Part of the reason that the very basic shielding algorithm described above was chosen was because the other, more complicated, candidate algorithms simply didn't work at all; which is also the reason they were not included in this report. Realistically, it came down to a matter of triage; move forward with a basic algorithm with relatively low performance, or use up the remaining available time with trying to tweak a more sophisticated algorithm. Ultimately, considering

the oft-mentioned happy circumstance where the asteroid itself shields the instrument's field of view from high energy GCR primary particles, thereby drastically increasing the natural probability that any high-energy particle detected is a transmitted muon, it was deemed unnecessary to work with a more sophisticated algorithm for this project. It is strongly suggested (in more detail in the recommendations section) that any future work include a more sophisticated shielding algorithm.

It is necessary, in closing, to mention one more metric that ultimately came in handy during the following parametric studies: namely the Muon Detection Efficiency (MDE). This is a very similar metric to the MIDP, but is distinct in that instead of measuring the proportion of correctly identified muons, it measures the number of muon hits that were thrown out (thereby not impacting the MIDP, but increasing any tomographic integration time a great deal). The MDE was simply a ratio of the number of hits to pass through the shielding algorithm to the total number of muon hits recorded by Geant4.

#### 4.4.2. Parametric Study on Boundary Conditions

The following graphic shows a colorimetric representation of the muon detection efficiency as parameterized by a series of non-zero azimuth and elevation angles. It is critical to note that this is for a low proportion of Muons in the test beam (only 2.5% total were muons, half + half -).

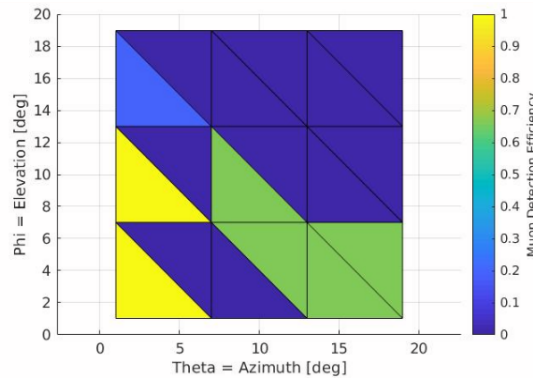


Figure 4.12: Effect on Muon Detection Efficiency of altering instrument elevation and azimuth angles with respect to bulk direction of incident particles

This was, in effect, surveying the results of altering the major axis of the instrument with respect to the test particle beam. It is obvious from the bounds of the plot that ONLY one quadrant in the azimuth/elevation grid plane was tested. This was because the instrument exhibits bi-planar symmetry about both the XY and YZ plane; thus, for example, the same behavior is expected for an azimuth of 15 degrees, elevation 10 degrees as for all three: azimuth -15 degrees, elevation 10 degrees, azimuth -15 degrees, elevation -10 degrees, and azimuth 15 degrees, elevation -10 degrees.

The bounds of the plot were chosen based upon the field of view of the baseline instrument, namely 18.43 degrees. The baseline instrument was the result of the preliminary trade study, and consists of 3 hodoscope stacks in a 3U cubesat configuration with silicon PSD and gridded cherenkov paddles at each stack. This baseline design can be seen in Figure 4.11.

Returning to Figure 4.12, the plot uses delaunay triangulation and a built-in interpolator in MatLab to generate such a colorimetric plot; the datapoints occur for every square grid-line. The coarse mesh obviates any particularly detailed analyses; but a few qualitative conclusions are possible:

Firstly, it is evident that, when ONLY the azimuth OR the elevation is increased, the instrument still performs relatively well in the total number of muons detected (proportional to the

total number of clean hits). When both the azimuth and elevation are increased, the detection probability goes down.

Secondly: another way to look at this situation is to consider the instrument fixed and the incidence angle of incoming particles to be varying. In this case, the above figure gives a first look at field-of-view performance. This was originally estimated to be 18.43 degrees based upon the geometry of the baseline design (seen above) and first principles of optics; but it is apparently a more complicated function in reality. Again, time constraints precluded any more detailed investigation of this phenomenon because it edges outside the scope of the thesis. The major qualitative conclusion that can be drawn is that the instrument (with this active shielding algorithm) works best when pointed straight at the particle source (vis. When pointed along the nadir vector intersecting the target asteroid). The major justification for NOT investigating this particular phenomenon in greater detail is simply that such pointing requirements, in both Earth-centered and deep space missions, have been routinely met for decades. They are well within the realm of plausible operational requirements.

The following figure shows the same study performed with a different metric: the Muon Identification Probability:

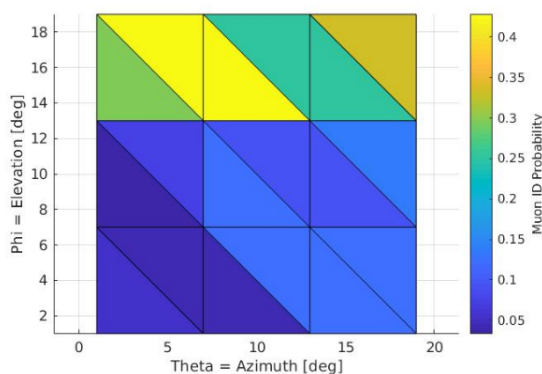


Figure 4.13: Effect on Muon ID Probability of altering instrument elevation and azimuth angles with respect to bulk direction of incident particles

This graphic shows the probability that, if a clean hit is successfully selected by the active shielding algorithm, it is a muon. Again, this is for low proportions of muons (2.5% of the total test beam). This is a somewhat confusing figure; it shows a nearly opposite response to the detection efficiency previously. However, the muon detection efficiency and this probability are not coupled. This shows that, in effect, if a high-angle particle passes through the detector and successfully passes through the active shielding algorithm, it is quite likely to be a muon. This makes sense when the fact is considered that, especially at very fringes of the field of view, the path length traversed through shielding is appreciably greater. All particles are more likely to undergo a nuclear interaction and suffer deflection beyond the tolerance for track linearity, or are more likely to trigger an EM cascade that confuses the event signal enough that it is obliged to be thrown out by the current active shielding algorithm. Muons, with a far smaller scattering cross section, are naturally less likely to be thus affected, and are therefore proportionally more likely to be detected at high incidence angles.

The following figure shows the results of a repeat of the angle-effect study but with a higher proportion of muons included in the test beam (25% instead of 2.5%).

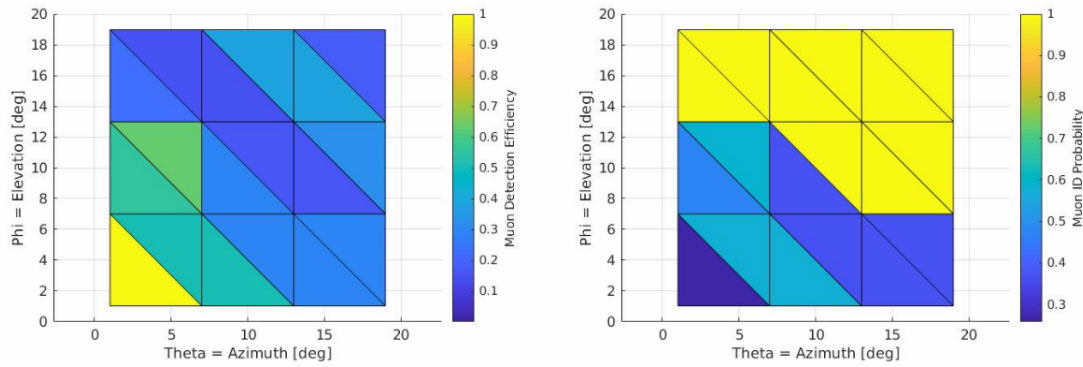


Figure 4.14: Effect on Muon Detection Efficiency AND Muon ID Probability of altering instrument elevation and azimuth angles with respect to bulk direction of incident particles. This run used a higher proportion of muons, 25%

This figure shows the same exact plots of Muon Detection Efficiency and Muon ID Probability as presented before except that the proportion of muons in the test beam was increased to 25%. The same overall decrease in muon detection efficiency at larger incidence angles was observed, but the effect was drastically less.

Again, a similar trend in the muon ID probability; it is notable that the effect observed in the low muon proportion beam earlier is much pronounced with a higher proportion. However, because the muon ID probability is simply the ratio of the total number of muons that struck at least some Sensitive Detector Volume within the instrument to the number of clean hits recorded, the increase is attributable to a simple bump in the numerator of said ratio.

One further trial was run with the highest proportion of muons in the beam yet: 250%. The results of this trial are shown below:

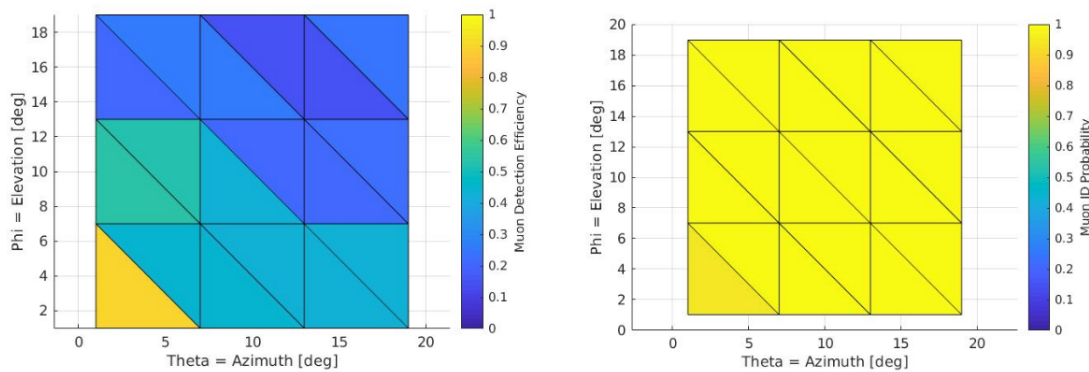


Figure 4.15: Effect on Muon Detection Efficiency AND Muon ID Probability of altering instrument elevation and azimuth angles with respect to bulk direction of incident particles. This run used a yet higher proportion of muons, 250%

And finally, we see that the muon detection efficiency changes very little when the proportion of muons in the test beam is increased from 25% to 250%. This, in and of itself, is a useful qualitative conclusion; it is expected that a fairly high proportion of the particles incident upon the instrument FROM the asteroid surface will be muons, if at a very slow count rate. Thus, this indicates that, while the active shielding algorithm + Baseline model are less effective for low proportions of muons in the incident beam, at higher proportions there is little difference.

Again, for completeness, the muon ID probability is show; this is somewhat trivial at such high levels of muons, however. (i.e. most of the particles injected were muons; so the probability of clean hits being muons is very high everywhere).

#### 4.4.3. Parametric Study on Geometric Configuration

The geometry parametric study was intended as a sort of informal optimization exercise. Indeed, the only practical difference between this study and a formal optimization algorithm is that the final evaluation of all options was left to be primarily qualitative; though based mostly upon numerical data generated during the parametric study itself. This method of qualitative optimization was for two reasons: Firstly because the simulations run to generate data for this study are, by their very nature, unvalidated (though their mechanisms were verified; see chapter on verification), and secondly, because the mesh into which the parameters was broken was very coarse. The latter was principally constrained by the sheer magnitude of the data files generated: even the coarse mesh required over 40 separate simulations and resulted in nearly 5 gigabytes of data. Finer meshes would, of course, cause these figures to increase geometrically. Thus, the use of a less formal, qualitative, assessment of the optima presented by this study was deemed to be the best fit for such a feasibility study.

Each simulation model was subjected simultaneously to an encompassing spherical particle source that injected particles with the energy and species spectra of Galactic Cosmic Ray primaries as generated by SPENVIS, which in turn uses the CREME96 model (CITE). Secondly, a 5 cm radius circular surface beam particle source composed of 37.5% protons, 37.5% electrons, and 25% muons (12.5%  $\mu^+$  and 12.5%  $\mu^-$ ) with energies ranging linearly between 1-10000 GeV, and a 5 degree symmetrical cosine angular distribution, was fired at the forward end of the instrument along its major axis from approximately 60 centimeters distance. The composition of this second beam was arbitrary in all respects except the particles species and the relative muon concentration. The species were chosen because the mix of muons, protons, and electrons was expected to be the most difficult for the active shielding algorithm to differentiate, and the mix of muons was substantially enriched from what was expected to be found in nature to decrease the number of particles that had to be fired for each evaluation. The linear energy spectrum for the beam was approximated from the first two data points in the proton GCR primary energy spectrum. It was deemed sufficient to use such a crude energy spectrum because it represented all of the most likely incident particle energies, and subjects the instrument to an ultra-high energy particle environment that is worse than anything it is even remotely likely to experience. The beam is, in other words, designed to be the worst case scenario; if the instrument can successfully handle such a simulation, nature should be far less demanding. The probability of firing was split evenly between the two particles sources (spherical and beam).

The objective functions, if you will, of this informal optimization study were twofold: the muon detection efficiency and the muon identification probability. The muon detection efficiency consists of the ratio of the number of recorded instrument hits that turned out to be caused by a muon to the total number of muons injected. In essence, this metric tracks the percentage of injected muons that the detector (and current active shielding algorithm) successfully recorded. Higher is obviously better for this metric. The second, arguably more important, metric is the muon identification probability. This metric consists of the ratio of the total number of muons injected to the total number of hits recorded. This is the probability that a filtered, recorded, hit is a muon. Ideally, this detector would record only muons; therefore, the higher the muon ID probability, the better.

This second metric, the muon ID probability, is important for another reason. It was decided, much in keeping with the theme of this feasibility-study-thesis, that the quality of the simulation data precludes the expenditure of a great deal of time and effort on highly complicated filtering algorithms. In essence, if we can't say with certainty that the *detail* level behavior of the instrument will exactly match the simulations (because the study is unvalidated), then it is foolish to expend effort building an active shielding algorithm that relies upon such levels of detail. The algorithm used, therefore, simply filters out all hits that do not pass through all layers, in the correct direction, with a enough linearity that fitting all hit points to a line with Orthogonal Point Regression yields a squared covariance ( $R^2$  value) greater than 0.8, with sufficient energy to saturate the borosilicate Cherenkov paddles (i.e. generate around 220+ photons / cm, which roughly corresponds to ions of charge = 1e of greater than 1 GeV).

Therefore, this higher level parametric study also provides the probability that any hit which passes through this relatively simple active shielding algorithm with the associated instrument geometry is, in fact, a muon. In other words, one can identify any hit successfully passing through the active shielding algorithm as a muon with a chance of accuracy equal to the muon ID probability.

Both metrics were investigated independently, and then were combined in a few objective functions designed to point in the general direction of a more global optimum design.

Having discussed the boundary conditions and the primary simulation output metrics, it only remains to discuss the actual parameters that were used as independent variables in the previously mentioned objective functions. Three major parameters of the instrument design were chosen: the overall length, the number of stacks in the hodoscope, and the aspect ratio of width / length. These parameters were chosen based upon the previously completed literature survey of all existing particle detectors that have a relatively similar function: measuring very high energy particles. Most of the instruments surveyed used a hodoscopic design with varying numbers of layers, varying depth, and varying frontal area. Otherwise, the designs were remarkably similar except for minor differences in passive shielding configurations, and sensor design. It was decided to forego a parametric study varying instrument type etc. for two reasons: it would have demanded the construction of a new active shielding algorithm for each instrument configuration, and the sensor composition was already constrained in the initial design trade study. It was decided to forego a parametric study involving different shielding materials because of the most commonly used particle radiation shielding materials: concrete, water, lead, aluminum, and polymers, only aluminum and polymers had a prayer of simultaneously falling within restrictive launch-mass budgets and had at least some flight heritage and associated literature.

Thus, one instrument model was constructed for every feasible combination of these three parameters. There were some combinations, usually involving small instrument dimensions and large numbers of stacks, that were not geometrically feasible. Finally, the parametric study consisted of subjecting each such model to the aforementioned particle radiation bombardment and thereafter computing the MDE and MIDP during post processing completed with MatLab.

It was deemed most effective to generate colorimetric graphics evaluating the various parameters of the "objective function(s)", and the two primary such graphics for the MDE and MIDP respectively can be seen in Figure 4.16:



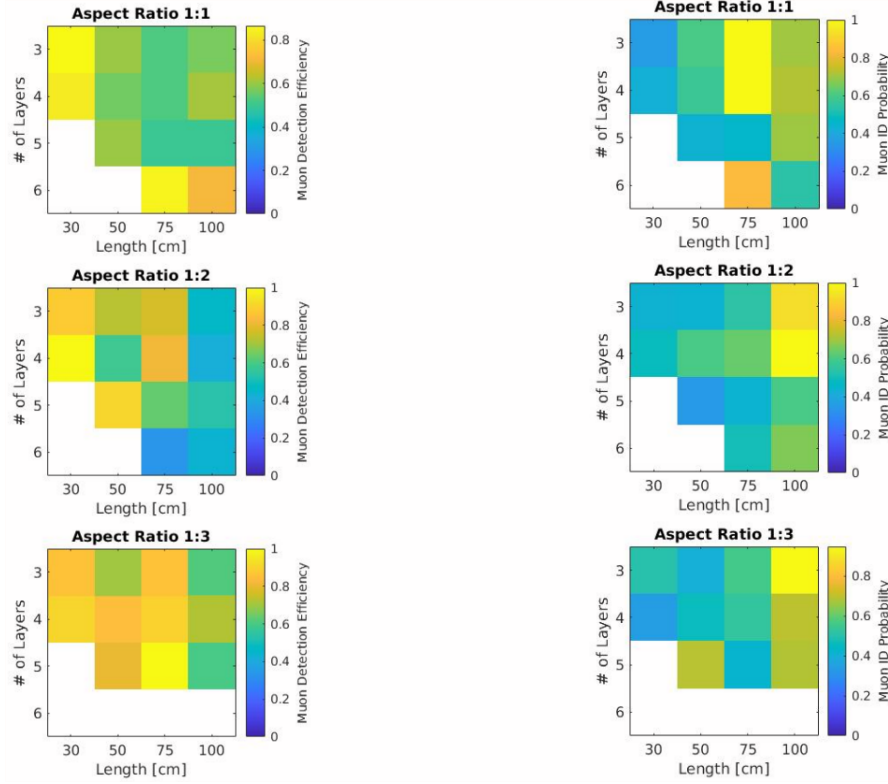


Figure 4.16: Effect on Muon Detection Efficiency AND Muon ID Probability of altering instrument geometric parameters

In both cases, the color scale was chosen such that the highest value of the MDE or MIDP respectively shows up as bright yellow. White squares represent the aforementioned geometrically unfeasible options. In the left pane showing the muon detection efficiency, it appears that there is a better detection efficiency in all 3 aspect ratios for smaller instruments with fewer stacks, and the worst performance for larger instruments with fewer stacks. The former, in retrospect, is most likely because the large length, low number of stacks combination greatly increases the proportion of shielding in the particle path, subsequently increasing its likelihood of deflection or total dissolution in an EM or hadronic shower. Also, it appears in general that a higher aspect ratio yields a higher muon detection efficiency. This makes sense because all secondaries with a large radial velocity component (i.e. velocity perpendicular to the major axis of the instrument) have a much higher probability of exiting the instrument rather than interacting further with internal sensors.

The Muon Identification Probability, again arguably the more important of the two metrics, showed a more pronounced trend. The instruments that most consistently yielded high ID probabilities (i.e. those which are best at actually detecting muons with the existing basic active shielding algorithm), were those with large length and fewer stacks. This upper right hand “cornering” effect was increased by more elongated aspect ratios. This makes sense for similar reasons mentioned before in the discussion of the MDE: long instruments with few stacks tend to have a much higher proportion of passive shielding to filter out particles like protons or electrons which are much more likely to interact with matter and produce secondaries, with fewer instrumented stacks to be saturated by the self-same secondaries.

It is worth mentioning here that there at least a few detector geometries that, when combined with the active shielding algorithm appear to very effectively filter out all non-muon signals. Had this *not* been the case (i.e. all geometries had very low muon ID probabilities), it would have been necessary to go back to the drawing board to find a geometry/algorithm combination that was more successful in positively identifying muons. As it stands, however, there are a few options that present positive ID probabilities in excess of 90%.

As aforementioned, it was deemed beneficial to attempt to find something approaching a global optimum instrument configuration by combining both the MDE and the MIDP into one objective function. This was done twice, and plots similar to the previously included colorimetric graphics were generated for each independent objective function:

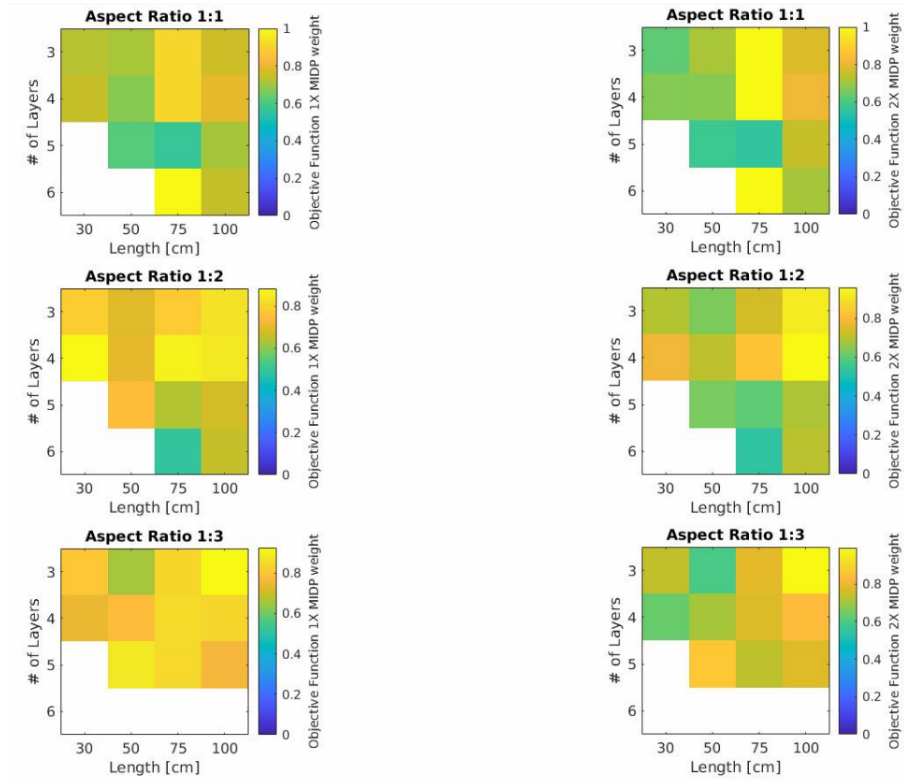


Figure 4.17: Informal optimization of MDE and MIDP using a combined objective function

Both of the scenarios detailed above used a very simple combined objective function as follows:

$$obj_n = \frac{w_1 MDE_n + w_2 MIDP_n}{w_1 \max(MDE) + w_2 \max(MIDP)} \quad (4.1)$$

Essentially, the MDE and MIDP vectors were added together and normalized to the maximum of the resultant summed vector. Differing weights were added to each metric to account for the relative importance of each. The plot in the left pane above represents, colorimetrically, the computed value of the objective function shown above with  $w_1 = 1$  and  $w_2 = 1$  respectively. This was done primarily for reference because in reality, the MIDP is the more important metric. To this end, the second, right hand, pane shows the result of the objective function for which  $w_1 = 1$  and  $w_2 = 2$ . It must be noted that the decision to rate MIDP as twice as important as MDE was subjective, but based upon the logical requirements of design: finding a detector geometry/algorithm combination that was capable of detecting muons moves the project far closer to achieving the original design goals implied by the research questions.

A few clear local optima present themselves in the right pane of the above figure, namely instruments with:

1. an aspect ratio of 1:1 with 6 layers and a 75 cm length
2. an aspect ratio of 1:2 with 4 layers and a 100 cm length
3. an aspect ratio of 1:3 with 3 layers and a 100 cm length.

These three candidates have muon identification probability values of 0.833, 1.00, and 0.9474 respectively. The 1:1 aspect ratio candidate was eliminated because it would obviously have both the highest volume and mass, and also has the lowest MIDP of the three selected candidates. It was decided that the remaining two candidates would benefit from another round of simulation with a larger particle count to generate MDE and MIDP values with a larger Monte Carlo population behind them, hopefully smoothing out the effects of any outlier particles etc.

These two models were subjected to a simulation with identical boundary conditions as before except the beam particle source was moved back from 60 to 100cm from the center of mass of the instrument, out in front, and the radius of the circular beam particle source was increased from 5cm to 15cm. Finally, the simulation was conducted ten times with 500 particles per run instead of 300. These modifications do, to some extent, render *direct* comparison with the previous results difficult, but it was thought that the advantage of determining if the MDE / MIDP results were a one time fluke caused by a serendipitous set of boundary conditions in the original study or not outweighed the disadvantage of changing the particle source. The results were as follows:

1. AR 1:2, 4 layers, 100 cm Length: MDE = 0.5974 (18.04%), MIDP = 0.6629 (8.71%)
2. AR 1:3, 3 layers, 100 cm Length: MDE = 0.739 (9.84%), MIDP = 0.7126 (18.39%)

The drop in both MDE and MIDP was fairly drastic. The standard deviations of each metric across all 10 trials is shown in parentheses above. The large standard deviation of the 3 layer, 1:3 aspect ratio simulation shows that the original run was reasonably consistent, merely on the higher side of the standard distribution, well within 2 sigma. This is not the case for the 4 layer 1:2 aspect ratio model. For this, the original run is more than 5 times the standard deviation from the mean. The explanation arose from the difference in particle source. In both cases with the 1:3 aspect ratio, a far higher proportion of the frontal area was bombarded with primaries than with the 1:2 model. When the 1:2 model in the new trial was bombarded on a far higher proportion of its frontal area, the overall MDE and MIDP decreased. Because the “all-encompassing” radiation model is far closer to reality (as opposed to a focused beam that strikes only a small proportion of the instrument’s active area), it was decided that the original results of this parametric study were not valid. It was decided to re-run the study taking care to ensure that every single instrument model was bombarded by a beam source that fully engulfed the active frontal area of the instrument.

For the second run, it was also noticed that the number of hits for an instrument of smaller frontal area is proportionally less. Therefore, the total number of injected particles was scaled inversely to the frontal area of the detector model to try to ensure that the number of incident particles is uniform in addition to the uniform total occultation of the detector’s frontal area. The minimum number of particles injected was 1000 for the 100cm 1:1 AR simulations. All other models were bombarded by a greater number of particles inversely proportional to their frontal area.

The two combined objective functions used before were re-computed using the updated parametric study results:

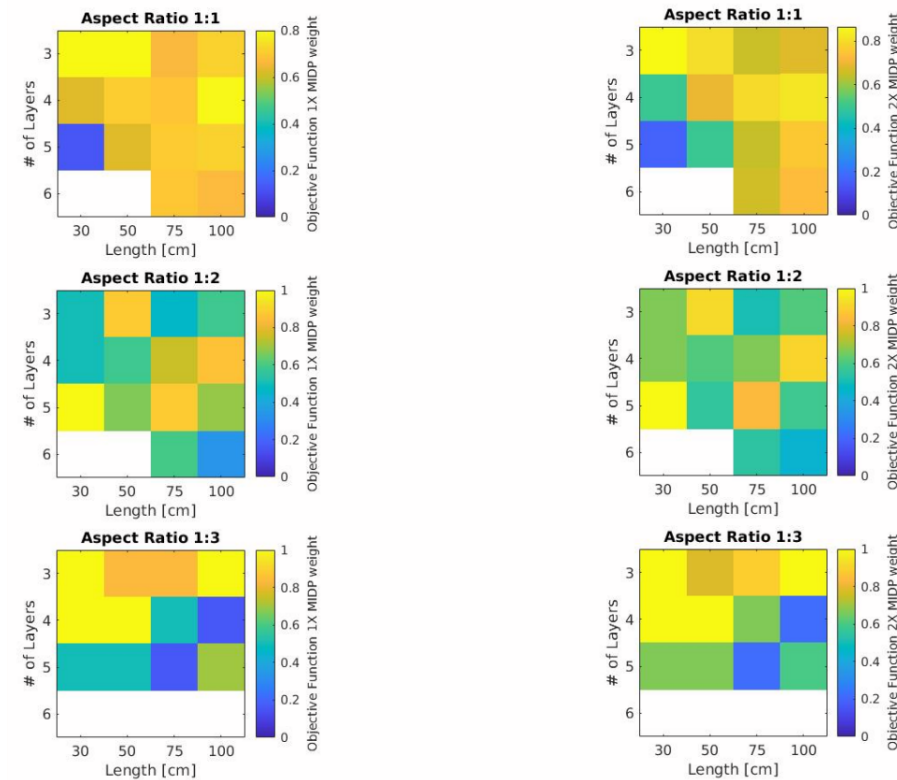


Figure 4.18: Informal optimization of MDE and MIDP using a combined objective function - rerun.

It is noteworthy that the previous trends in MDE are not evident in the new results. However, the MIDP tends to show similar results; in particular, the same 2 local optima as before are evident in the right-hand pane (weighted to favor the MIDP in the objective function). The 1:3 aspect ratio, 3 layer, 100 cm model, and the 1:2, 4 layer, 100 cm model both appear to good advantage (if not the best) in this updated study.

Because the underlying goal of the instrument is to achieve consistency across a range of foreseeable particle radiation boundary conditions, the fact that these two models, in particular, perform well also under these new boundary conditions is highly in their favor. Thus, though they do not represent the full local optimum, their recurring good performance was considered sufficient to choose these two models as the winners of this second parametric study once again.

Both were subjected to a similar round of more intensive bombardment to evaluate their MDE and MIDP performance in more detail. This time, each model was bombarded by 1000 primaries (spread across both beam and spherical particle sources) in ten separate trials:

1. AR 1:2, 4 layers, 100 cm Length: MDE = 0.670 (25.4%), MIDP = 0.6389 (16.46%)
2. AR 1:3, 3 layers, 100 cm Length: MDE = 0.6913 (17.60%), MIDP = 0.7147 (19.04%)

The metrics for both models changed relatively little with the updated particle radiation boundary conditions. The MDE for model 1 increased by 12.15% (within 1 sigma, using standard deviations from either run), while its MIDP decreased by 3.62%, (well within 1 sigma of either run). The MDE for model 2 decreased by 6.45% , while the MIDP increased by 0.29% (well within 1 sigma of either run).

It is reiterated that the larger value of MIDP evident in figure Figure 4.18 is within 1 sigma of the value obtained in the multi-run follow up trials. Thus, it is reasonable to conclude that the mean MIDP and MDE obtained in this follow up trial are numbers that can be used in

evaluating future results, within an error of  $\pm 1 \sigma$ . Between the 2 models tested, it is evident that Model 2 consistently had higher MIDP values; it is, therefore, reasonable to draw the aforementioned qualitative (but logical) conclusion to this informal optimization study and state that the best geometric configuration for the instrument, from amongst the models surveyed, is that with an aspect ratio of 1:3, 3 stacks, and a 100 cm length. Considered from a physical perspective, this makes sense in a few ways: Firstly, the long length and fewer number of stacks mean that there is a larger proportion of polymer shielding per track length than virtually any other configuration; this apparently stops a larger proportion of secondary particles that might otherwise confuse readings. Secondly, the 1:3 aspect ratio means that any secondary particle with a large radial velocity component relative to the major axis of the instrument (or primary particle entering from outside the instrument's field of view) has a relatively short distance to traverse before exiting the instrument volume. Coupled with the aforementioned lower number of sensitive layers, this decreases the number of errant particle signals picked up. Thirdly, and finally, the long and skinny aspect ratio of the instrument presents another advantage: namely that particles with large angle of incidence compared with the nadir vector between the instrument and the asteroid are rejected. As concluded in the previous parametric study where the effect of non nadir incidence vectors of incoming particles was analyzed, the instrument and algorithm baseline worked best when pointed very nearly, or perfectly, parallel to the nadir vector. Rejecting large incidence-angle particles reinforces this effect.

A side-view illustration of Model 2, as used in this parametric study, is shown below for reference:

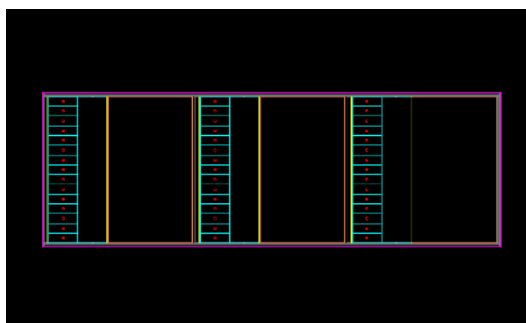


Figure 4.19: Geometric Parameter Study: Final Design

### Geometric Parameter Study Implications

It must be noted that the original instrument design was supposed to fit within 1 or 2 standard CubeSat units (U). It rapidly became evident that, with a maximum timing resolution of something around 100ps, such a small instrument would not be able to provide sufficiently precise timestamps for particle transition through each hodoscope layer to give critical data on time of flight. As it happens, time of flight data is used to determine the direction of flight in the active shielding algorithm, and if it is ambiguous whether an event progressed through each layer sequentially in the right direction, the event was thrown out; hurting the MIDP. Thus, the smaller instruments surveyed in this study, including the baseline design of an instrument fitting within 3Us, showed poor MIDP results, and were eventually thrown out. The winning model is much more massive; at a meter in length, and 33cm on a side for width and height, it is evident that such an instrument is far beyond the confines of a traditional CubeSat, even a larger 12U or 16U model. Such an instrument would, necessarily, require a larger microsatellite or small-satellite bus to hold it; though power requirements would still be minimal. Perhaps the most relevant implication of this parametric study's strong support of a larger instrument is the much increased mass. The mass of the selected instrument, for example, is estimated at somewhere around 150 kg. This is quite large, but not unfeasible; the AMS-2 particle detector, for instance flown on the ISS, weighs in at more than 6700 kg [18].

For the purposes of this study, which exists in a design space somewhere before the preliminary design, the mere fact that launching such an instrument in a small-sat format is possible is enough for a go ahead to the next phase. It must be re-emphasized that such treatment of the design mass is possible only because this is not a design exercise, but a feasibility study; the goal here is to determine if muon tomography of asteroids is possible, and what such an instrument *might* look like as a starting point for more detailed mission and instrument design exercises that might follow.

A final point to be made is that the muon ID probability of the selected design is around 71.47%. This means that a clean hit in an environment dominated by GCR primaries and any radiation that may come off the surface of an asteroid, there is a 71.47% chance ( $\pm 19.04\%$ ) that the particle is a muon. In normal circumstances, even a qualitative assessment would be justified in concluding that this is too low without a more sophisticated active shielding algorithm to increase the ID probability. However, this project benefits from a few key unique environmental boundary conditions that make such an ID probability acceptable. This is simply that muons have a relatively short lifespan of around  $2.2\mu s$  [36], and can therefore only be detected quite close to the asteroid in question. It is likely that the instrument must be so close, in fact, that the asteroid will fully occult the field of view of the instrument. This means that the asteroid itself will block all incoming GCR primaries that would otherwise strike the frontal area of the instrument within its field of view; thus, the only particles that are likely to hit the instrument will come off the surface of the asteroid itself. The only high energy particles likely to do so are muons or the unlikely event of GCR back scatter. Because of this special situation where the instrument is unlikely to be subjected to any particle signal anywhere near as dirty as that used in this parametric study, a relatively low muon ID probability is compensated for by the fact that any high energy particles hitting the instrument are very likely to be muons in the first place.

## Verification and Validation

Any simulation based project requires at least some calibration or verification, comparing it to data collected from experimentation, to be grounded in reality. Ideally, full validation would be undertaken, where an experiment specifically designed to test the model itself was constructed.

Of the two "poles" of this project, time and budget constraints precluded such experimentation on the instrument side of things, though it is clear that building and testing an instrument prototype at some level would be the next logical step of development for this research. Thus, one falls back upon verification whereby the behavior and performance of simulation tool(s), in this case Geant4, are evaluated against existing data and/or theory.

The ultimate result of these time and budget constraints is quite simple; the findings of this research project are currently unvalidated. However, the *methodology* and background theory used to generate the results has been verified, according to the definitions used in the first paragraph of this chapter. It is useful, therefore, to think of the results of this report in the way that one may consider simple data extrapolations performed in less complex analyses. They give indications of behaviors beyond the confines of existing data, and are, perhaps, of the most worth in providing high level assessment of whether further experimentation is worthwhile. It is reiterated that that is the aim of this project.

It is worth noting that no novel physics theory was used, and the vast majority of the unknown parameters were macroscopic boundary conditions; in other words, the very well tested particle-physics mechanisms within Geant4's Monte Carlo transport code were neither modified nor employed to simulate totally novel processes. In trusting the physics kernels within Geant4, it is reasonable to trust the results of the analyses performed for this project within a reasonable expectation of approximation. The approximate nature of the results was kept in mind during the drawing of conclusions for this report.

Thus, ultimately, the methods employed for verification of the simulations performed in this project were principally intended to ensure the proper *use* of the simulation tool, and to debug the simulations themselves.

It did, ultimately, prove possible to perform a small amount of result validation analysis in this project, however, with respect to the opposite "pole" of research mentioned in the Introduction: namely the Asteroid Environment. As discussed in the Simulation chapter, in order to normalize all simulations to a timescale, and to calibrate a muon-only source used

to speed up computation times, a number of muon production and transmission parameters were generated. Of these, three turned out to be qualitatively comparable to similar results published in the 2014 NASA Advanced Innovative Concepts white paper on Asteroid muography written by Prettyman et al [61]. These were the muon production flux, the transmitted muon flux, and the surface count rate. These are compared in some detail in the final section of this chapter.

## 5.1. Instrument Simulation Verification

Verification of the whole Geant4 model central to this research project focused upon the subsidiary model of the instrument itself, which consisted mainly of a primary physics check. In said primary physics check, The Geant4 code used to simulate the detector was subjected to verification trials intended to ensure agreement of results with established theory. The basic form this took was to fire single particles of varying types, energies, and incident trajectories at isolated sensitive detector volumes of types surveyed within the design trade off process; thereafter comparing the response with published data or theory.

### 5.1.1. Basic Physics Test

Two types of Geant4 volumes were tested with a number of different particle types and energies: a polystyrene scintillator, and a borosilicate glass Cherenkov radiator. The primary goal of these tests was to verify the correct computation of particle energy loss within the model, of photon generation by either Cherenkov or scintillation mechanisms, and to generate an empirical model for the response of SiPMs used to pick up the photons generated in either type of detector volume.

#### Scintillation Mechanism Check

Scintillation, as briefly discussed in chapter 2, is the transformation of energy, deposited by a transiting particle, into photons.

Again, as aforementioned in chapter 3, the scintillator chosen for evaluation is a POPOP organic scintillator in a solid PVT solvent. These are readily available and have well-understood behavior.

A few key boundary conditions, related to Birk's law as detailed in the Background chapter, were needed by the Geant4 scintillation module: the scintillators specific photon sensitivity ( $S$ ), and the associated Birk's constant ( $k_B$ ). For the scintillator, these constants were  $k_B = 0.126 \text{ MeV/mm}$  and  $S = 10,000 \text{ photons/MeV}$  respectively [71]. It is critical to note here that there is a rather large uncertainty in these published values. The source with the best certainty was chosen, but inaccuracies persist.

A series of particles were fired at the scintillator with the following types and (total) energies:

Table 5.1: Single Particle Verification Test Run Parameters

Particle Type	Energy Range [GeV]	Charge [e]
Proton	0.1 - 1E+6	+ 1
Electron	1E-3 - 1E3	+/- 1
Muon	0.1 - 1E+6	+/- 1
Alpha particle	0.1 - 1E+6	+ 2

To model such a scintillator in Geant4, a standard physics list class was modified slightly to support both Cherenkov and Scintillator physics that were otherwise not included. The following figure shows the results of firing one particle at a time, at logarithmically increasing



kinetic energy intervals, at the scintillator block and testing the number of total detected photons (Note, this is NOT the number of processed photons, which is lower due to SiPM imperfections, but the total number generated). The results of this simulation, using protons as the particle species, can be seen below:

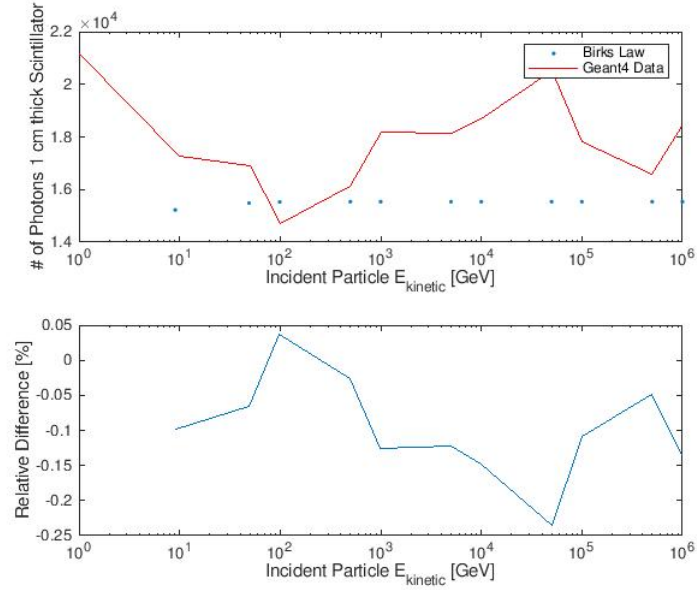


Figure 5.1: Comparison of Geant4 scintillation simulation results with high-kinetic-energy protons with analytical Birks model[21].

The above figure demonstrates that the results of Geant4's internal scintillation simulation and the well-established analytical model of Birk's law agree reasonably well. The average difference between theory and Geant4 data was -9.8% (i.e. the Geant4 photon count caused by proton strikes exceeded that predicted by theory by an average of 9.8%). It is, furthermore, readily apparent that the Geant4 data exhibits a large spread about its own mean, roughly  $\pm 9.96\%$ . There was only one secondary (an electron) produced in the verification trial plotted above. This occurred at the datapoint corresponding to a primary proton with a kinetic energy of  $50^4$  GeV: the highest spike in photon count. Accounting for this, the mean difference between theory and Geant4 results, relative to theoretical photon counts, was 8.5% and the spread of the Geant4 photon count about its own mean decreased to 9.04%.

For reference, the same trial was completed with both positive and negative muons. Despite one outlier in the Geant4 photon count, the agreement between theory and simulation showed the same trend. There was very little difference in scintillator response between the positive and negative muon trials. Thus the mean results can be seen plotted as follows:

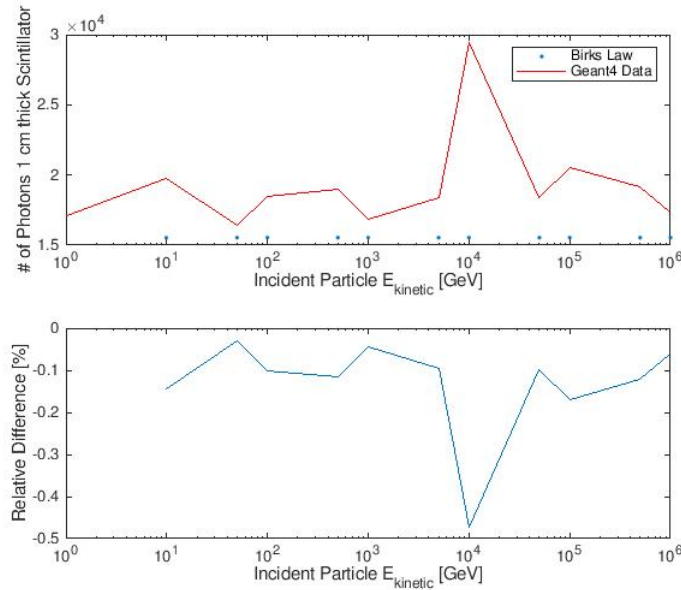


Figure 5.2: Comparison of Geant4 scintillation simulation results with high-kinetic-energy muons with analytical Birks model[21].

The outlier data point turned out to be due to a nuclear interaction; an otherwise highly improbable event that was, of course, not captured in the minimum - probable energy deposition model (discussed in Background Section Equation 2.12) used to generate the theoretical data points. This will not be a problem in future simulations because the source of the energy deposition data will be drawn from Geant4 itself instead of the analytical model used here. Without the outlier datapoint, negative muon strikes yielded a -18.86% deviation from theoretical photon counts, and positive muon strikes yielded a -16.61% deviation from theory. These deviations, plotted in the lower-pane of Figure 5.2 show an essentially stochastic variation around the mean except for the aforementioned point that showed a nuclear interaction.

However, this is a fairly bad deviation, higher than acceptable for empirical simulation results. It was discovered that literature values for the measured Birk's Constant ( $k_B$ ) for POPOP scintillator dissolved in PVT were quite variable, with the experimental value nearly 100% larger than the smallest experimental value [71]. Furthermore, the scintillation coefficient (number of photons per MeV of deposited energy) also varied significantly between sources; also exhibiting over 100% difference between maximum and minimum values [21][7][6].

This unreliability in the Geant4 scintillation kernel ultimately reinforces the decision to implement scintillation with Birk's theory. It would, of course, have been necessary regardless because of the huge computational load of tracking tens of thousands of optical photons for every strike, but the badly-behaved simulation kernel makes the use of extensively tested and validated theory doubly sensible.

The ultimate result of the analysis behind this verification trial is to render scintillation-based detector layers less favorable in the final design trade off. However, it is very important to note that the photon count calibration activity outlined in the Simulation chapter is *not* tainted by the poor results of the Geant4 Scintillation kernel. This is because the calibration is sensitive primarily to the propagation of optical photons. This optics kernel is well validated in scintillation, and other, applications [13] [73]. So long as the momentum vectors of the photons generated by the scintillation module are randomly generated as the primary transits the scintillator; the calibration is valid.

### Cherenkov Check

The same checks performed on the scintillation simulation were performed upon the Cherenkov simulation; refer to Table 5.1 for boundary conditions. In general, the results were much closer to theoretical predictions for Cherenkov photons. The following figure illustrates the comparison of theory vs. simulation over a logarithmic scale with over 100 increments:

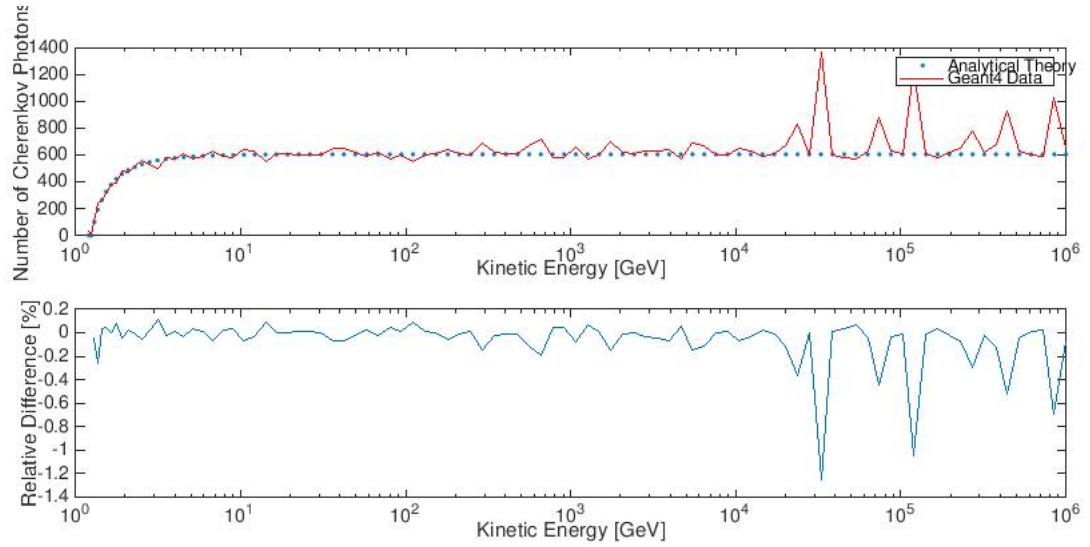


Figure 5.3: Comparison of Geant4 Cherenkov Radiation simulation results with high-kinetic-energy protons with analytical Frank & Tamm model [30].

The far greater number of increments than scintillation was due to the fact that the number of photons generated was, by and large, at least an order of magnitude less than the number of photons generated by the organic scintillator POPOP discussed in the previous section. This allowed much faster computation.

Some outliers are evident in Figure 5.3; these correspond to the generation of an electromagnetic shower within the Cherenkov radiator. These events were *not* separated from the output signal because they would not be separated in real life. This gives an estimate of expected error for a very wide range of input energies, and is still quite low at 6.84%. Because of the much lesser computational requirements, all of the particle energies mentioned in Table 5.1 were possible. The analysis performed on these plots was identical to that discussed with respect to Figure 5.3, and also to the similar evaluation of theory vs. simulation performed in the previous subsection. The verification results for the Cherenkov effect induced by impacting electrons can be seen below:

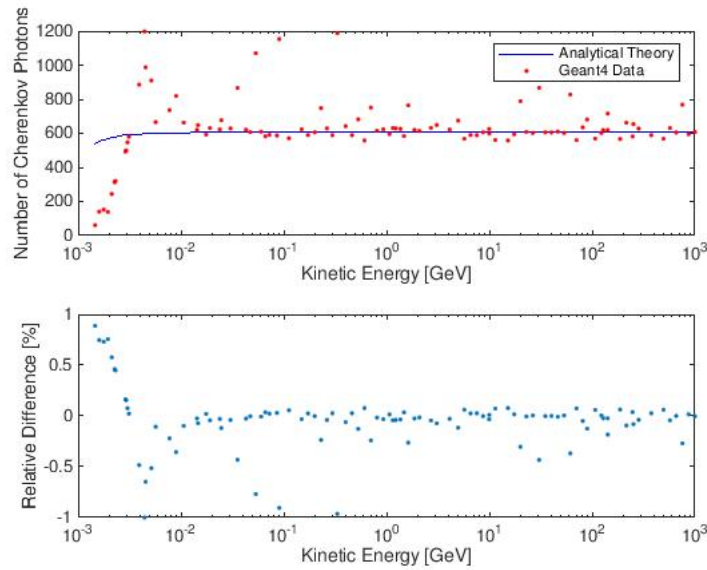


Figure 5.4: Comparison of Geant4 Cherenkov Radiation simulation results with high-kinetic-energy electrons with analytical Frank & Tamm model [30].

Perhaps unsurprisingly, electrons do not follow analytical theory very well, especially at lower energies. The overall difference to Frank & Tamm's theory was -4.55%, but the standard deviation from theoretical values was nearly 29.5%. This reflects the much higher scattering cross section that low-mass electrons experience as they pass through matter.

To attempt to characterize the probability of deviation, a second trial run was made where, instead of firing just one electron at every energy interval, 20 were fired. The standard deviation from theory was computed for each of these bins and plotted below:

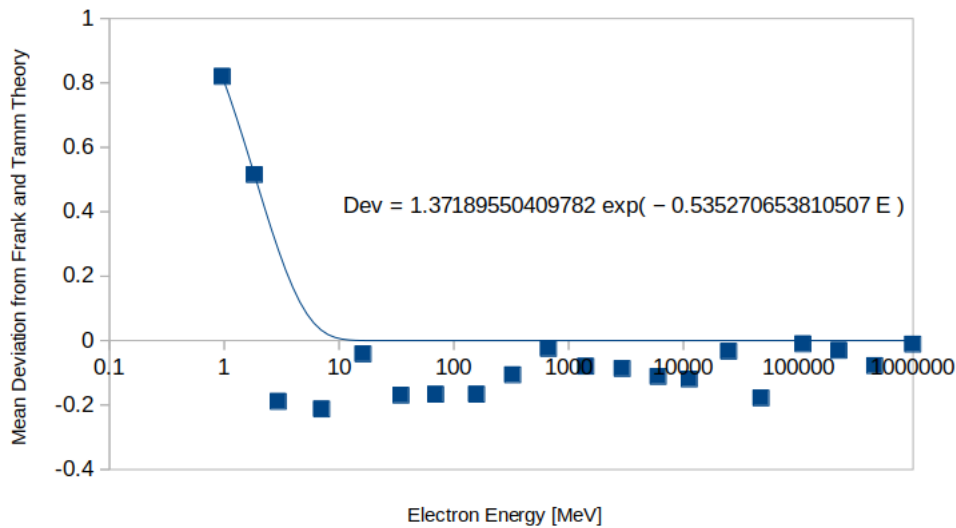


Figure 5.5: Mean deviation of the number of Cherenkov photons generated impacting electrons within Geant4 from Frank & Tamm's theory as a function of incident particle energy

This information shows the average deviation of the number of Cherenkov photons generated by Geant4 from Frank & Tamm's theory at a number of different energies between  $1\text{E-}3$  and  $1\text{E+}3$  GeV. At each incident electron energy the number of photons appears to deviate around a theoretical mean with a roughly normal distribution. However, this mean has a fairly high skewness in the negative direction. This means that the average photon count is close to

theory, but that there is a long tail trending upwards. This is perhaps best illustrated by the following figure:

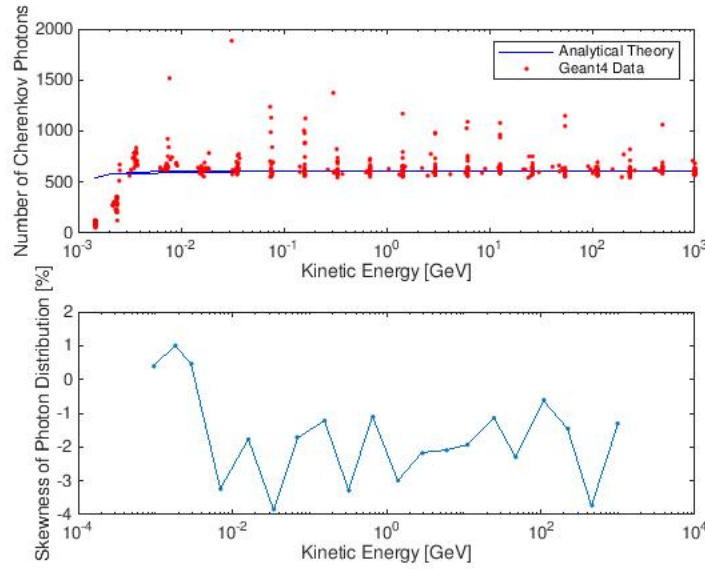


Figure 5.6: Skewness of distribution of the number of Cherenkov photons generated impacting electrons within Geant4 around a mean of Frank & Tamm's theory as a function of incident particle energy

While this does not really have any implications for the verification of the existing simulation, it does have great implications for the selection of a model for the generation of Cherenkov photons by transiting electrons. They will be simulated by calculating the mean number of photons from Frank & Tamm's theory, and applying a random deviation based upon the shape of the distribution curve evident in Figure 5.6.

The following figure shows the same check performed for alpha particles on a logarithmic energy scale.

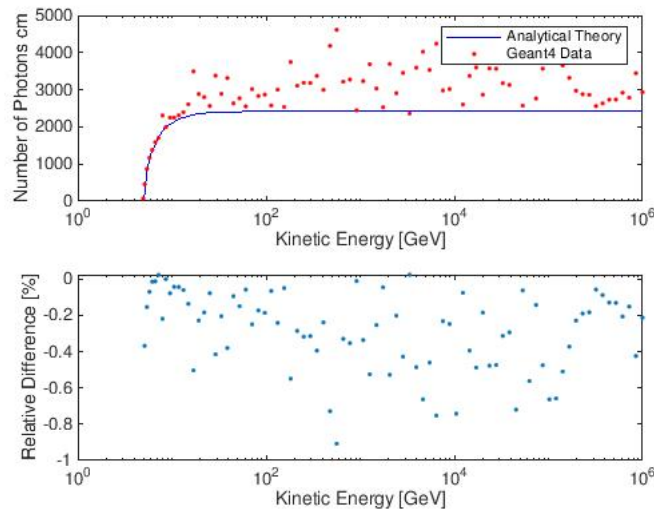


Figure 5.7: Comparison of Geant4 Cherenkov Radiation simulation results with high-kinetic-energy alpha particles with analytical Frank & Tamm model [30].

As with the electrons, a large scatter is evident in the data. Unlike the Electrons, the scatter in the number of Cherenkov photons evident as the energy of particle increases, is almost exclusively due to the production of secondaries which then induce their own Cherenkov radiation. Electrons show similar secondary production at high energies, but their deviation is also affected by the higher path length of their easily-deflected transit through the radiator.

The number of secondaries, and the total energy of secondary particles produced, is plotted below for the alpha-particle trial:

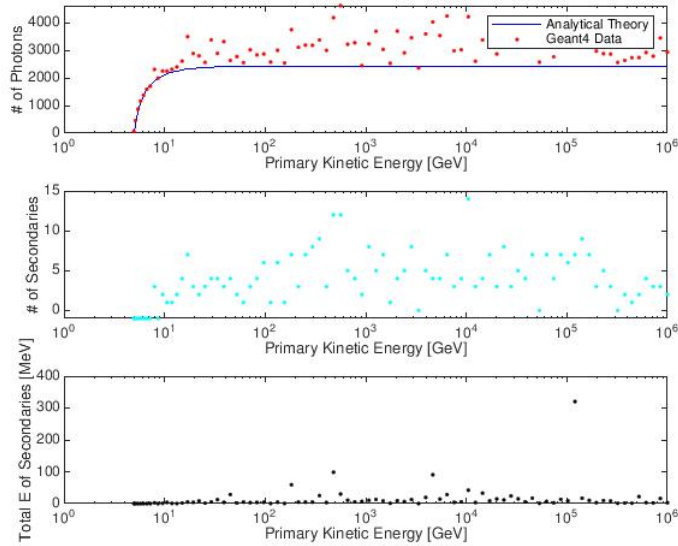


Figure 5.8: Number of secondary particles, and the total energy of all secondaries, produced by alpha particles transiting the Cherenkov radiator

It is evident simply from qualitative observation that the number of secondaries is correlated to the increased deviation of the photon count from theory. In fact, the correlation coefficient between the number of secondaries and the photon count deviation was 0.788, which, referring to Table 3.1, is a "high correlation."

Further analysis into the effect of secondaries is not warranted for the simple reason that the only physical process that needs to be implemented in a more computationally cheap manner is the cherenkov effect itself *not* the generation of secondaries. Implementation of a formula-based Cherenkov module need only poll the hit-tracker module within Geant4 to obtain each individual particle's energy deposition, whereupon the total photon count seen in Figure 5.7 can be reproduced by calculating each individual particle's contribution.

## 5.2. Asteroid Environment Simulation Validation

One of the reasons that the oft-mentioned 2014 NASA Advanced Innovative Concepts white paper on Asteroid Muon Tomography by Prettyman et al proved so foundational in this project is because it provides one of the few sources against which at least the environmental simulation results can be cross checked. The white paper reports upon the simulation (using FLUKA instead of Geant4) of muon transport through spherical asteroid models with concentric (large) inclusions. Two models were simulated by Prettyman et al, a 50m diameter model (with inclusion) and an 800m diameter model (with inclusion) [61]. The ultimate asteroid model used for this project was 100m in diameter, neatly splitting the difference. Prettyman et al used a much smaller bulk density, however, and a more simplistic chemical composition for their asteroid model. The regolith density used in this project, the reader will recall, was  $3.4 \text{ g/cm}^3$ , while Prettyman et al used a value roughly half of that:  $1.6 \text{ g/cm}^3$ .

In this project, it was ultimately chosen to model asteroid composition from the microscopic to the macroscopic; based upon the evaluation that the hard mineralogical data and bulk-density estimations of the sample returned by Hayabusa I were superior to rough approximations based on rotational dynamics or in-kind comparison of surface spectroscopy with terrestrial mineralogy. It must be noted, however, that both densities, that used by this project, and that used by Prettyman et al, are within the range of possible S-type asteroid densities reported in associated literature [15]. With respect to chemical composition, the white paper reported use of what they call "Standard Rock," which was composed of 20%  $\text{FeO}$  and 80%  $\text{SiO}_2$ . The comparison of chemical composition can be seen tabulated below:

Table 5.2: Comparison of the chemical composition of model used in NASA white paper [61] and this thesis

<i>25143 Itokawa Regolith Composition (this project)</i>				<i>"Standard Rock" Composition (Prettyman)</i>			
Element	MF*	Element	MF	Element	MF	Element	MF
O	0.3565	Ti	0.0263	O	0.3776	Ti	0.000
Fe	0.1926	S	0.0060	Fe	0.3887	S	0.000
Mg	0.1104	H	0.0022	Mg	0.000	H	0.000
Si	0.0940	Ni	0.0011	Si	0.2337	Ni	0.000
K	0.0514	Co	0.0011	K	0.000	Co	0.000
Na	0.0460	Cu	0.0010	Na	0.000	Cu	0.000
Ca	0.0443	Cr	2.1015e-4	Ca	0.000	Cr	0.000
Mn	0.0337	V	2.0878e-4	Mn	0.000	V	0.000
Al	0.0329	P	1.0110e-4	Al	0.000	P	0.000

\*Mass Fraction

The average compositional atomic number ( $Z_{AVG}$ ) of the 25143 Itokawa regolith samples was 14.9172, while that of Prettyman et al's "Standard Rock" was 11.00. The average compositional atomic mass ( $A_{AVG}$ ) of the 25143 Itokawa regolith samples was  $31.0301 \text{ g/mole}$  while that of the "Standard Rock" was 22.30 [61]. Thus, the compositions were fairly similar, though the bulk density and nucleus-density of the 25143 Itokawa regolith data used in this project was appreciably higher than that used in the white paper.

The implications of this relatively small compositional difference on the comparability of results is complex. The lower density used in the white paper increases the probability of secondary particle propagation in hadronic showers, but the larger density and/or nucleus count of the regolith model used in this project increases the chance of nuclear interactions that generally lead to the richest secondary generation in any case. Furthermore, Prettyman et al also highlight the complexity of comparing the propagation of EM and hadronic showers through different materials; they used a density-scaling method to compare their in-regolith results with well established atmospheric GCR air-shower data, but mentioned key flux factors, like the cross section moment and attenuation lengths used in this analytical scaling that are sensitive to chemical composition [61]. Their results point out that muon production in planetary regolith is somewhere around 3 orders of magnitude less than that in the



atmosphere.

Because of the inherent approximation necessary throughout a feasibility project such as this thesis (and indeed the Prettyman white paper), it was deemed unnecessary to dig deeper into the complex physical behavior of hadronic showers through different media to achieve a more quantitatively exact comparison between the results of Prettyman et al and those in this project. Ultimately, if the simulation results proved comparable within an order of magnitude, the discrepancy could probably be chalked up to compositional and density effects. A relatively close result would be sufficient to validate the approximate nature of the thesis simulation results, and thereafter propagate through to imply a coarse validity of any conclusions drawn. Considering the utter lack of any experimental or in-situ data to confirm or deny even the white-paper results (a fact explicitly noted in the white paper itself, one might add [61]), this would essentially have to be good enough; and indeed, fits within the framework of this feasibility study as first discussed in the Introductory chapter of this report.

In considering the validity of this comparison, it is, perhaps relevant to mention one final query: Why did this project not simply use the exact same composition and model constraints as the white paper that provides the only even partial validation opportunity? The ultimate answer is simply that, as previously alluded to, that it was judged that using the best available compositional data was more important. There is, after all, so little that is actually known about the interior of asteroids at present that improving the accuracy of *any* model parameters (for instance by using data gathered from returned samples from 25143 Itokawa) becomes quite critical in contributing to the realistic accuracy of any conclusions drawn, even the broad qualitative conclusions that are the ultimate aim of this feasibility study. This was, at the end of the day however, essentially a judgement call. It was impossible to quantify the benefits and detriments of either choice for a formal trade off without first performing the simulations. Thus, in retrospect, it would likely have been better to use density and composition values similar to that use by Prettyman et al for the asteroid model; but due to the (painfully) large amount of computation time required for simulations, it was not feasible to redo the entire environmental simulation study, analysis, and write up (a process of approximately 1.5 months) with the altered composition. However, as will be demonstrated in the following text, taking into account the aforementioned differences between the two models, there turned out to be remarkably good agreement between comparable metrics used in the white paper and the thesis project.

The first, and most important, point of comparison between the two simulations is the generation-flux of muons in a downward direction in a solid-asteroid regolith proxy. The comparative results can be seen below:

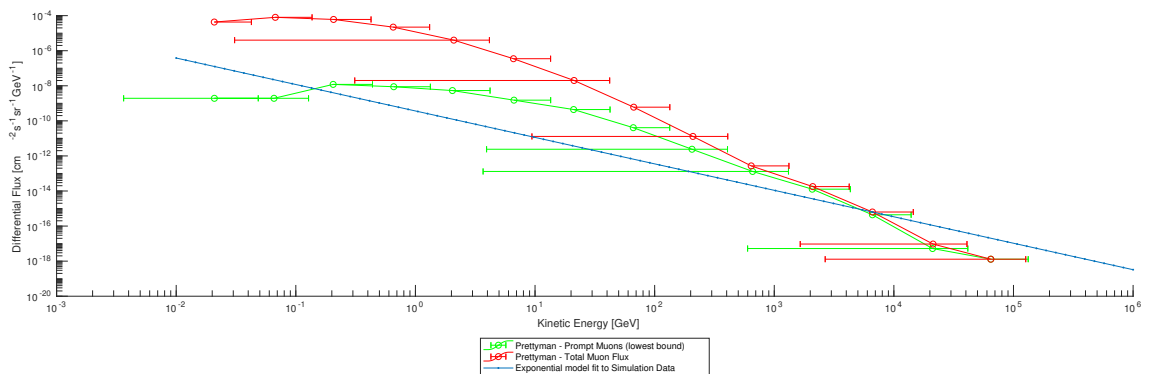


Figure 5.9: Comparison of simulated differential flux of muon generation in regolith reported by Prettyman et al and exponential model for same value fitted to this project's simulation results[61].



The red and green series on the plot represent the total muon flux reported by Prettyman et al, and the prompt muon flux caused by the decay of higher energy mesons (e.g. pions, kaons etc.) [61]. They serve as convenient upper and lower bounds on the estimated flux presented in the whitepaper. The blue line shows the extrapolated muon generation flux as presented in the Simulation chapter (Equation 3.12). It is critical to reiterate here that despite 30+ hours of simulation time and over 9 million injected GCR primaries, there were considerably less than 100 muons generated; all of relatively low energy. By themselves, these results are very much *not* statistically significant. *However* they are the best that could be hoped for with the limitations that have often been mentioned before in this report, *and* they yielded results that agree, to the first order, with those published in this white paper. Therefore, the muon energy function denoted by the blue line in Figure 5.9 was used to build the muon-only particle source described in the Simulation chapter. The question may arise: Why not use the data from Prettyman et al that appears to be more accurate than a simple exponential energy-spectrum for muon production? A few major reasons arise: Firstly, it was deemed more consistent to use the data generated in this simulation for future applications in the same simulation chain. Secondly, as is evident above, the uncertainty in the energy coordinate of the data provided in the white paper is quite large. Finally, and perhaps most critically, Prettyman et al verified *their* results against a density-scaling method proposed by Geisser [34]. This method involves scaling atmospheric muon-flux data to a regolith density. The two separate scalings that were presented in the white paper are shown below with the exponential model derived from this project's simulation data:

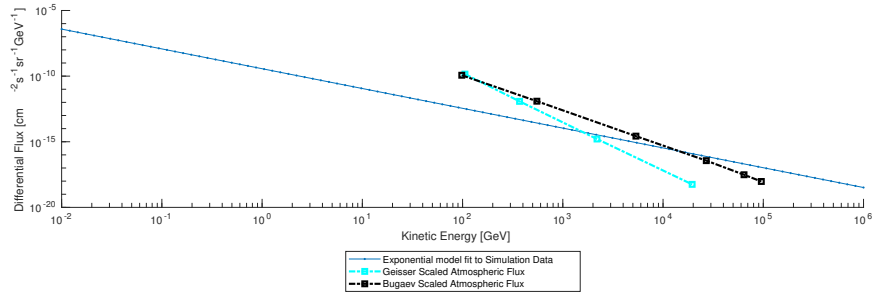


Figure 5.10: Comparison of scaled differential flux of muon generation in atmosphere reported by Prettyman et al, and exponential model value fitted to this project's simulation results[61].

The two data series presented were both used by Prettyman et al, and represent scaling of two different data sources presented by Geisser and Bugaev respectively [34][23]. Accounting for the difference of regolith density and the aforementioned discrepancy in chemical composition between the simulated data in this project and that used by Prettyman et al, there is at least some agreement that supports the approximate validity of the simulation results. It should be noted that no error estimates were provided for the scaled fluxes shown in Figure 5.10.

There are some critical implications to this approximate validation however. Namely, the simple exponential muon-energy spectrum model that was built from the limited simulation results tends to underestimate at lower energies and tends to over estimate at very high energies (greater than  $10^5$  GeV). The latter high energy overestimation is less worrisome because the flux of these muons is nearly 20 orders of magnitude lower than the highest flux, and is about 9 orders of magnitude less than the flux predicted at  $10^3$  GeV (the upper end of the most useful transmitted muon energy range predicted by Prettyman et al themselves [61]). Thus, the implications of this less-than-perfect model is in keeping with the whole theme of this feasibility study, good enough to draw preliminary, mostly qualitative, conclusions that nevertheless may prove useful to any future research on this topic. It is re-emphasized that it was deemed more important to maintain consistency and use results generated from prior simulations in future simulations instead of borrowing muon fluxes from Prettyman et al.

One final point of comparison that presents itself is the comparison of backscatter. Prettyman et al included some results for upward leakage current of particles generated in a large asteroid (figure 14 [61]). Of the backscatter particles produced in the simulations of *this* project (the reader is referred back to the Simulation chapter for more detail), the white paper presents results for only a limited number of particles. Of these species, the presented proton leakage rate was chosen for comparison (from fig 14 in Prettyman et al) because the proton flux was relatively large in both simulations, thereby reducing the probability of stochastic error. This leakage rate was not presented parameterized by altitude, but as an energy spectrum. Unfortunately this yields limited opportunity for comparison, but, the white paper reports an upward flux of 0.1564 protons per second per square meter at 117.69 MeV. The simulation results of this project show 0.1085 protons per second per square meter at an energy of 150 MeV; both measured at the surface. Considering all of the previously discussed limitations and caveats of both this project and the comparison to this NASA white paper, this result shows a reasonable level of first order agreement. It is less important than the muon fluxes presented before, but was deemed worth inclusion because of the dearth of data, either simulated or real, about asteroid regolith backscatter.

# Conclusions & Recommendations

## 6.1. Review of Research Questions

A final audit of the original research questions from a retrospective viewpoint is useful. By and large, most of the research questions were at least partially answered:

*Question (1Ai): What are the characteristics of muon emissions that have traversed the thickness of said asteroid; as opposed to same-side muon generation in the surface regolith?*

As discussed in the results of the Simulation chapter, transmitted muons displayed an overall count rate of between 1-2 per square meter per day. This count rate was investigated over a range of potential altitudes, and can be seen in Figure 3.20. The corresponding integrated flux of the transmitted muons, at the surface and beyond, can be seen in Figure 3.19. By comparison, the differential flux of the muons generated by backscatter was higher, as shown in Figure 3.15, but their comparative energy was very low, as shown in Figure 3.16.

*Question (1Aii): Are there any other appreciable sources of muon emissions that may interfere with the detection of particles that directly penetrate the full asteroid?*

The only sources of muons in the asteroid environment were from GCR backscatter, the secondaries produced by the transmitted muons, the transmitted muons themselves, and any muons that may have been produced by hadronic showers within the instrument itself. Of these, the backscatter was already covered in the previous question, and the active shielding algorithm used is largely capable of filtering out any secondaries that are produced within the instrument.

*Question (1Aiii): Will the other types of radiation present at the study site pose a risk of false detection and unusable data for the detector?*

This was primarily covered in the Design chapter: particularly in the section detailing the results of the final design trade study simulations. Two sub studies were performed to evaluate the effect of changing radiation boundary-condition parameters, and to evaluate the effect of changing geometric configurations of the detector, respectively. The final design option that was indicated by the results of these studies showed partial success at filtering out background radiation; it was able to correctly identify about 72% of the muons that struck it. The results of the final geometric configuration trade-study can be seen in Figure 4.18.

It is possible to conclude, from this result, and from the results presented in the Simulation chapter that showed that the count rate of muons generated in asteroid regolith is approximately 8 orders of magnitude lower than the count rate of impinging GCR primary particles, that the major limiting factor of instrument/filtering algorithm design is its ability to distinguish the exceedingly faint transmitted muon signal against a loud background.

*Question(1B): What is the optimum target size and/or location for an asteroid targeted for muon tomography?*

This question, ultimately, was hampered by computation constraints. Aside from the basic success of muon transmission through a 100 meter diameter, S-class asteroid, no specific results were achieved for larger asteroids. Muon transmission through larger asteroids remains feasible [61], but any further conclusions remain unsupported by the simulations conducted during this project.

*Question (2): What detection method(s) are best suited to a low-power, small form-factor, cheap, space-tolerant, hodoscopic detector design?*

Ultimately, the full answer to this question could be produced only with physical test data to back up simulation results. That is, as mentioned in the Introduction, outside the available scope of this project. The best possible conclusion that can be drawn from the available data is that the instrument design option that was ultimately selected at the end of the final trade-study, detailed in the Design chapter, is one possible combination of detection methods that could be used. In some small defense of this project, it is worth noting that this combination of detection methods would be a decent starting point, at least, in any future design study. The particular advantage of the configuration surveyed is that it is composed principally of materials that are very resistant to long-term radiation exposure, and has a fairly low number of fault-intolerant subsystems.

*Question (3A): What passive shielding will best shield the detector from non-muon radiation with a minimum amount of mass?*

As detailed in the assumptions write up in the Design chapter, a parametric study with differing shielding *compositions* was deemed to be of less value than studying the effects of varying other instrument parameters. However, one of the geometric parameters thus investigated was the effect of the number of sensitive planes on the overall detection efficiency of the instrument. A lower number of planes corresponded to a higher proportion of inter-plane passive shielding. The final design selected can be seen in Figure 4.19, and, indeed, favors a higher proportion of passive shielding in between sensitive planes. This is likely because the extra passive shielding stops some of the unwanted secondaries generated within the instrument volume itself. It is possible to conclude, therefore, that the more inter-plane shielding possible, the better; this corresponds with the general principle of high-energy particle calorimetry as well [54].

*Question (3B): Is it possible to design a simple active shielding filtration algorithm that will enable the sorting of unwanted detection events from the desired muon radiation signal?*

Though the ultimate muon detection efficiency of the final instrument design was only 72% (under worst-case-scenario test conditions admittedly), when considered *within* the scope of this particular application, this active-shielding result is acceptable. This is because, as mentioned in the review of question (1ai) and (1aaii), the backscatter signals within the field of view of the instrument are low energy, low flux, or both. Thus, a simple algorithm designed to filter out far greater fluxes and energies of particle species within its field of view that shows a

72% success rate under such worst-case scenarios, is acceptable under more-realistic, more favorable, conditions.

It is worth noting, however, that the active shielding algorithm used in this investigation was one of the main limiting factors for performance. It was kept to a basic level because of the above-mentioned advantageous environmental conditions, but is likely the single most fruitful area of potential investigation available for any future work based upon the results of this project.

*Question (4A): What is the optimum field of view for a singular instrument in surveying a roughly spherical asteroid about which it is in orbit?*

The field of view was originally constrained by a series of deductive arguments made to the effect that, in order to take advantage of the oft-mentioned effect of the asteroid, in effect, blocking most of the incoming GCR primaries if it fully occults the field of view of the instrument, the instrument should have a relatively small field of view. Practically, this translates to an instrument with an aspect ratio (mean frontal width divided by length) of around 1:3. In the final trade study, detailed in the Design chapter, it became evident that there was a certain advantage of such high aspect ratio instrument options, most likely due to the fact that secondaries generated within the instrument with a large radial momentum component would exit the instrument volume of a 'skinnier' detector far more rapidly than a 'fat' detector, thus decreasing the probability of producing tertiary particles and further confusing the detection signal. Thus, there were, at least, some simulation results that supported the use of lower fields of view.

However, it is important to mention that the results of the asteroid environment simulations showed that an instrument is best applied very close to the surface of said asteroid. By simple geometry, this means that the field of view of the instrument is not only fully occulted, but that a narrow field of view captures only a relatively small sliver of the asteroid's interior. Furthermore, a very strong conclusion that could be derived from the asteroid-environment simulation results was that the more area a detector could muster, the better. Again, by simple geometry, this favors 'fat' instruments, because they get more frontal area and a wider field of view, with less volume than a 'skinny' instrument of equal frontal area.

It is unfortunate that results from the the two opposing poles of this project should contradict one another like this, but it does provide some insight that is ultimately more valuable in a feasibility study than a low-detail design option.

*Question (4B): What is the optimum Pointing Accuracy of the Instrument?*

The answer to this question arose in the first parametric study that was performed as part of the final trade study. This was detailed in the Design chapter. This study observed the effects of both bulk incidence angle of the test beam (including muons) and varying muon proportion on detection efficiency. The most indicative result with respect to the varying of incidence angle can be seen in the left pane of Figure 4.14. Essentially, the detector efficiency is highest at incidence angles. In fact, it was even possible to constrain the pointing accuracy to within about 3 degrees from this data. It is critical to note that the metric shown in the right-hand pane of Figure 4.14, the ID probability of Muons shows what appears to be an inverse behavior to the detection efficiency. Firstly, the metrics are conceptually related, but quantitatively quite different. Secondly, the pointing accuracy results drawn from the detection efficiency results are not invalidated by the ID probability results because the ID probability merely shows that high-incidence angle particles were more likely to be properly identified as muons; no pointing requirement can be distilled from this conclusion.

## 6.2. Conclusions & Recommendations

In keeping with the definition of a feasibility study used throughout the execution of this project, and the limited scope outlined by the research questions pursued, the conclusions drawn here were made with an eye toward broad validity and future applicability rather than exhaustive quantitative specificity. The inability to undertake prototype testing, and the limited resolution possible with limited computing power allow for nothing else.

Thus, the following is a list of the major conclusions of this study:

- It is, ultimately, feasible to design an instrument capable of detecting muons against a space background radiation environment.
- The most important characteristic of such a detector is its sensitive area.
- The largest margin for performance improvement of such a detector is in the design of its active shielding and/or post processing algorithms.
- The optimum placement for such a detector is as close to the asteroid surface as possible; though there may be "sweet spots" at select higher altitudes that yield good performance as well (see Appendix B).
- The final instrument design option and active shielding algorithm are *not* capable of adequately characterizing the energy of successfully identified muons. It is, therefore, capable only of muography based upon count-rates and incidence angle, not internal density mapping through energy-loss back-computations as proposed by Prettyman et al [61].
- The transmission of muons through an asteroid of 100m diameter is possible.
- The fluence of transmitted muons at the surface of the asteroid is around 1-2 per square meter per day; this agrees, to first order considering model and simulation differences, with results from Prettyman et al [61].
- It is possible to take advantage of the asteroid itself as a shield against most unwanted radiation in the instrument's field of view.

One further item to consider, though there was not enough data to draw formal conclusions, is that the dynamic nature of orbit around an asteroid would complicate the muographic data collection of any instrument. This dynamic simulation was originally planned, but time constraints simply precluded it. However, most asteroids rotate, and because of the complexity of adding orbital dynamics into the muon tomography of asteroids, it may even be advisable for any orbital instrument to be placed at an "asteroid-synchronous" orbital altitude for long enough to provide sufficient integration time, and then perhaps moved to a different "asteroid-synchronous" orbit. Such a situation would fairly closely mimic the results of this project in any case. Furthermore, because of the inherent advantage of placing a hodoscope as close to the surface as possible, there is a reasonable case to be made that an orbiting instrument concept could be thrown out altogether in favor of landing a stationary hodoscope on the asteroid surface. In fact, this latter idea is probably the simplest execution of muon tomography on an asteroid. It closely mimics the highly-successful muon tomography of a volcano performed by Tanaka et al [70], and there is recent precedent of landing an instrument on an asteroid by the Hayabusa II spacecraft currently visiting the Ryugu asteroid.

### 6.2.1. Recommendations

The next major deliverable for a feasibility study are inputs to any future design studies in the form of definitive recommendations. Specificity is advantageous, but only where such a specific recommendation can be derived from valid conclusions. Otherwise, the recommendations cover general boundary conditions and certain options that did *not* work. The

following is a list of major recommendations derived from this study that would likely be good to at least consider in any future work on this topic:

- Increase detector frontal area as much as possible
- Perform simulations that include orbital and rotational dynamics. Perhaps integrate Geant4 and Tudat libraries for this task AND / OR
- Investigate stationary (or rover-based) surface deployment of a muographic hodoscope.
- Re-evaluate the relative merits of scintillating fibers (perhaps particularly glass scintillating fibers for rad hardness) vs. PSD arrays.
- Include a design for a stacked calorimeter intended to accurately measure particle energy.
- Shed internal shielding mass with a more sophisticated, and well calibrated, active shielding algorithm.
- Build and test a prototype, even a small one. Both GCRs and muons are present to some degree on Earth's surface without needing access to a particle accelerator. Take advantage of this relatively cheap and readily available particle physics laboratory.
- Run GCR-bombardment simulation of asteroid model with a High Performance Computer capable of increasing the number of injected particles from 9.2 million by at least an order of magnitude. Recalibrate the muon source with this data.
- Use recalibrated muon source and High Performance Computer to run full integrated simulation of instrument and asteroid instead of the partial simulation detailed in Chapter 6.
- If the ill-defined mass constraints, which are the best that can be done for so preliminary a study, become restrictive enough to contra-indicate the rather larger, and passive-shielding heavy, design suggested by the results of this project, consider re-evaluating the implementation of a miniature Ring-Imaging CHerenkov (RICH) detector.

A few items in the preceding list warrant treatment in slightly greater detail:

Based upon the probable headaches of muon tomography in the highly dynamic setting of a highly perturbed orbit, it is strongly recommended that future research consider surface-based design options. Given the recent success of the deployment of two small rovers from the Hayabusa II spacecraft on the surface of the Ryugu asteroid (22 September 2018), it would be well worth the effort to investigate a mobile surface hodoscope that could position itself in multiple locations. The latter concept would likely be the optimum solution to minimize instrument and algorithm complexity and maximize the tomographic capacity of any such mission.

Scintillating fiber panels, used for particle tracking, should be considered by the reader. The reason that they were eliminated, the detrimentally large number of SiPMs and computer input/output pins needed, was weighted higher than it really merited in the mid-level trade study. This does *not* affect the validity of the conclusions, merely makes it more likely that either scintillating fibers, or the PSD arrays used in this project, could have been chosen without much effect on any of the subsequent results. The change in the relative import of the number of I/O pins was unforeseeable at the time of the mid-level trade study, coming to light only after a few more months of work and no more time to formally re-evaluate scintillating fiber panels. It is re-iterated that this does not change the results of this thesis, but is, in retrospect, an equally viable option to that taken.

The most compelling instrument design surveyed in this report was arguably that of the high altitude balloon-based CREAM instrument flown for GCR spectroscopy over Antarctica [11]. This instrument collects much, if not all, of the data necessary for advanced particle discrimination and total energy measurements. This may (on one of the final few pages of this thesis) present the question: why was the CREAM instrument design not more closely followed in

the instrument design exercises of this thesis? The answer is twofold: simulation constraints precluded it (primarily the computation time needed), and initial trade study results indicated that a simpler design may suffice. However, one particular element of the CREAM instrument is deemed critical for future instrument design studies: the calorimeter. Kinetic energy, ultimately, was not directly measurable at very high particle energies encountered in the final simulations. This was, probably, a consequence of the basic active shielding algorithm used, but constitutes a gap in the capabilities of the instrument that should eventually be filled. Indeed, the selection of the final instrument design was *because* it's larger amount of passive shielding made it functionally similar to a more formally designed calorimeter.

As aforementioned, perhaps the greatest margin for improvement of any instrument design is the active shielding algorithm. In particular, the pulse-shapes of actual physical detector elements were not considered. This was because of the oft-mentioned lack of any hard data from a prototype with which to calibrate any simulation of scintillator, Cherenkov, or PSD pulse shape. However, pulse-width modulation, coupled with more extensive time of flight measurements, is a very common means of particle discrimination; this is especially true at lower particle kinetic energies. Also, if one took the approach used in this report, namely a top-down assessment of algorithm performance, instead of a bottom-up physics-heavy algorithm design, there are a myriad of new and emerging "big data" and machine-learning tools that might be able to generate particle identification from what might otherwise appear to be patternless stochastic data.

The construction of a prototype, and the collection of hard data from said prototype, would be a key first step in drawing more specific, quantitative conclusions. This is not without precedent. A number of very inexpensive detectors have been designed, built, and tested in simple ambient GCR primary and secondary showers present anywhere on the surface of Earth. Indeed, Axani et al were able to gather muon-specific data with a very inexpensive scintillation-based counter that, though far from novel, did accurately demonstrate various physical phenomena including muon flux dependence on penetration depth (in atmosphere) [16].

The future researcher on the topic of optimum instrument design for asteroid tomography was recommended to strongly re-consider the use of a RICH style Cherenkov detector. This recommendation is partly driven by retrospective qualitative evaluation on the part of the author having a great deal more data available at the very end of the thesis than at the beginning. However, RICH detectors, critically, allow the collection of angular information, and allow one to forgo the use of trajectory linearity constraints used in the basic active shielding algorithm designed for this feasibility study. This is because the Cherenkov uniquely transmutes the angular, charge, and energy characteristics of an incident particle into "shock-cones" of photons that impact the imaging plane of any subsequent optics in unique patterns that likely do not suffer from the low noise tolerance of the designs used ultimately selected by the results of this thesis. This type of detector, however, would be very difficult to simply model without any direct validation. It is very strongly recommended that no work should be undertaken on any RICH detector design without the ability to build a prototype. This reasoning is basically a summary of why the RICH detector was abandoned in this thesis: it is complex and difficult to model.

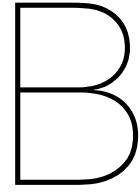


# A

## Mid Level Trade off AHP Matrix

Pairwise comparisons									
Criteria	1	2	3	4	5	6	7	8	9
1. Total Investment Value	1.00	0.50	0.33	0.25	0.20	0.17	0.14	0.11	0.09
2. Total Investment Value	2.00	1.00	0.67	0.50	0.40	0.33	0.29	0.23	0.19
3. Total Investment Value	3.00	1.50	1.00	0.75	0.60	0.50	0.43	0.35	0.29
4. Total Investment Value	4.00	2.00	1.33	1.00	0.80	0.67	0.57	0.46	0.38
5. Total Investment Value	5.00	2.50	1.67	1.25	1.00	0.83	0.70	0.57	0.48
6. Total Investment Value	6.00	3.00	2.00	1.50	1.20	1.00	0.86	0.71	0.59
7. Total Investment Value	7.00	3.50	2.33	1.75	1.40	1.17	1.00	0.83	0.68
8. Total Investment Value	8.00	4.00	2.67	2.00	1.60	1.33	1.14	1.00	0.80
9. Total Investment Value	9.00	4.50	3.00	2.25	1.80	1.50	1.29	1.07	1.00
10. Total Investment Value	10.00	5.00	3.33	2.50	2.00	1.67	1.43	1.19	1.00
11. Total Investment Value	11.00	5.50	3.67	2.75	2.20	1.83	1.57	1.31	1.00
12. Total Investment Value	12.00	6.00	4.00	3.00	2.40	2.00	1.71	1.43	1.00
13. Total Investment Value	13.00	6.50	4.33	3.25	2.60	2.17	1.86	1.55	1.00
14. Total Investment Value	14.00	7.00	4.67	3.50	2.80	2.33	1.99	1.67	1.00
15. Total Investment Value	15.00	7.50	5.00	3.75	3.00	2.50	2.14	1.79	1.00
16. Total Investment Value	16.00	8.00	5.33	4.00	3.20	2.67	2.29	1.90	1.00
17. Total Investment Value	17.00	8.50	5.67	4.25	3.40	2.83	2.43	2.02	1.00
18. Total Investment Value	18.00	9.00	6.00	4.50	3.60	3.00	2.57	2.14	1.00
19. Total Investment Value	19.00	9.50	6.33	4.75	3.80	3.17	2.71	2.26	1.00
20. Total Investment Value	20.00	10.00	6.67	5.00	4.00	3.33	2.86	2.38	1.00
21. Total Investment Value	21.00	10.50	7.00	5.25	4.20	3.50	3.00	2.50	1.00
22. Total Investment Value	22.00	11.00	7.33	5.50	4.40	3.67	3.14	2.62	1.00
23. Total Investment Value	23.00	11.50	7.67	5.75	4.60	3.83	3.29	2.74	1.00
24. Total Investment Value	24.00	12.00	8.00	6.00	4.80	4.00	3.43	2.86	1.00
25. Total Investment Value	25.00	12.50	8.33	6.25	5.00	4.17	3.57	2.98	1.00
26. Total Investment Value	26.00	13.00	8.67	6.50	5.20	4.33	3.71	3.10	1.00
27. Total Investment Value	27.00	13.50	9.00	6.75	5.40	4.50	3.86	3.22	1.00
28. Total Investment Value	28.00	14.00	9.33	7.00	5.60	4.67	3.99	3.34	1.00
29. Total Investment Value	29.00	14.50	9.67	7.25	5.80	4.83	4.14	3.46	1.00
30. Total Investment Value	30.00	15.00	10.00	7.50	6.00	5.00	4.29	3.58	1.00
31. Total Investment Value	31.00	15.50	10.33	7.75	6.20	5.17	4.43	3.70	1.00
32. Total Investment Value	32.00	16.00	10.67	8.00	6.40	5.33	4.57	3.82	1.00
33. Total Investment Value	33.00	16.50	11.00	8.25	6.60	5.50	4.71	3.94	1.00
34. Total Investment Value	34.00	17.00	11.33	8.50	6.80	5.67	4.86	4.06	1.00
35. Total Investment Value	35.00	17.50	11.67	8.75	7.00	5.83	5.00	4.18	1.00
36. Total Investment Value	36.00	18.00	12.00	9.00	7.20	6.00	5.14	4.30	1.00
37. Total Investment Value	37.00	18.50	12.33	9.25	7.40	6.17	5.29	4.42	1.00
38. Total Investment Value	38.00	19.00	12.67	9.50	7.60	6.33	5.43	4.54	1.00
39. Total Investment Value	39.00	19.50	13.00	9.75	7.80	6.50	5.57	4.66	1.00
40. Total Investment Value	40.00	20.00	13.33	10.00	8.00	6.67	5.71	4.78	1.00
41. Total Investment Value	41.00	20.50	13.67	10.25	8.20	6.83	5.86	4.90	1.00
42. Total Investment Value	42.00	21.00	14.00	10.50	8.40	7.00	6.00	5.02	1.00
43. Total Investment Value	43.00	21.50	14.33	10.75	8.60	7.17	6.14	5.14	1.00
44. Total Investment Value	44.00	22.00	14.67	11.00	8.80	7.33	6.29	5.26	1.00
45. Total Investment Value	45.00	22.50	15.00	11.25	9.00	7.50	6.43	5.38	1.00
46. Total Investment Value	46.00	23.00	15.33	11.50	9.20	7.67	6.57	5.50	1.00
47. Total Investment Value	47.00	23.50	15.67	11.75	9.40	7.83	6.71	5.62	1.00
48. Total Investment Value	48.00	24.00	16.00	12.00	9.60	8.00	6.86	5.74	1.00
49. Total Investment Value	49.00	24.50	16.33	12.25	9.80	8.17	6.99	5.86	1.00
50. Total Investment Value	50.00	25.00	16.67	12.50	10.00	8.33	7.14	5.98	1.00
51. Total Investment Value	51.00	25.50	17.00	12.75	10.20	8.50	7.29	6.10	1.00
52. Total Investment Value	52.00	26.00	17.33	13.00	10.40	8.67	7.43	6.22	1.00
53. Total Investment Value	53.00	26.50	17.67	13.25	10.60	8.83	7.57	6.34	1.00
54. Total Investment Value	54.00	27.00	18.00	13.50	10.80	9.00	7.71	6.46	1.00
55. Total Investment Value	55.00	27.50	18.33	13.75	11.00	9.17	7.86	6.58	1.00
56. Total Investment Value	56.00	28.00	18.67	14.00	11.20	9.33	8.00	6.70	1.00
57. Total Investment Value	57.00	28.50	19.00	14.25	11.40	9.50	8.14	6.82	1.00
58. Total Investment Value	58.00	29.00	19.33	14.50	11.60	9.67	8.29	6.94	1.00
59. Total Investment Value	59.00	29.50	19.67	14.75	11.80	9.83	8.43	7.06	1.00
60. Total Investment Value	60.00	30.00	20.00	15.00	12.00	10.00	8.57	7.18	1.00
61. Total Investment Value	61.00	30.50	20.33	15.25	12.20	10.17	8.71	7.30	1.00
62. Total Investment Value	62.00	31.00	20.67	15.50	12.40	10.33	8.86	7.42	1.00
63. Total Investment Value	63.00	31.50	21.00	15.75	12.60	10.50	9.00	7.54	1.00
64. Total Investment Value	64.00	32.00	21.33	16.00	12.80	10.67	9.14	7.66	1.00
65. Total Investment Value	65.00	32.50	21.67	16.25	13.00	10.83	9.29	7.78	1.00
66. Total Investment Value	66.00	33.00	22.00	16.50	13.20	11.00	9.43	7.90	1.00
67. Total Investment Value	67.00	33.50	22.33	16.75	13.40	11.17	9.57	8.02	1.00
68. Total Investment Value	68.00	34.00	22.67	17.00	13.60	11.33	9.71	8.14	1.00
69. Total Investment Value	69.00	34.50	23.00	17.25	13.80	11.50	9.86	8.26	1.00
70. Total Investment Value	70.00	35.00	23.33	17.50	14.00	11.67	10.00	8.38	1.00
71. Total Investment Value	71.00	35.50	23.67	17.75	14.20	11.83	10.14	8.50	1.00
72. Total Investment Value	72.00	36.00	24.00	18.00	14.40	12.00	10.29	8.62	1.00
73. Total Investment Value	73.00	36.50	24.33	18.25	14.60	12.17	10.43	8.74	1.00
74. Total Investment Value	74.00	37.00	24.67	18.50	14.80	12.33	10.57	8.86	1.00
75. Total Investment Value	75.00	37.50	25.00	18.75	15.00	12.50	10.71	8.98	1.00
76. Total Investment Value	76.00	38.00	25.33	19.00	15.20	12.67	10.86	9.10	1.00
77. Total Investment Value	77.00	38.50	25.67	19.25	15.40	12.83	11.00	9.22	1.00
78. Total Investment Value	78.00	39.00	26.00	19.50	15.60	13.00	11.14	9.34	1.00
79. Total Investment Value	79.00	39.50	26.33	19.75	15.80	13.17	11.29	9.46	1.00
80. Total Investment Value	80.00	40.00	26.67	20.00	16.00	13.33	11.43	9.58	1.00
81. Total Investment Value	81.00	40.50	27.00	20.25	16.20	13.50	11.57	9.70	1.00
82. Total Investment Value	82.00	41.00	27.33	20.50	16.40	13.67	11.71	9.82	1.00
83. Total Investment Value	83.00	41.50	27.67	20.75	16.60	13.83	11.86	9.94	1.00
84. Total Investment Value	84.00	42.00	28.00	21.00	16.80	14.00	12.00	10.06	1.00
85. Total Investment Value	85.00	42.50	28.33	21.25	17.00	14.17	12.14	10.18	1.00
86. Total Investment Value	86.00	43.00	28.67	21.50	17.20	14.33	12.29	10.30	1.00
87. Total Investment Value	87.00	43.50	29.00	21.75	17.40	14.50	12.43	10.42	1.00
88. Total Investment Value	88.00	44.00	29.33	22.00	17.60	14.67	12.57	10.54	1.00
89. Total Investment Value	89.00	44.50	29.67	22.25	17.80	14.83	12.71	10.66	1.00
90. Total Investment Value	90.00	45.00	30.00	22.50	18.00	15.00	12.86	10.78	1.00
91. Total Investment Value	91.00	45.50	30.33	22.75	18.20	15.17	13.00	10.90	1.00
92. Total Investment Value	92.00	46.00	30.67	23.00	18.40	15.33	13.14	11.02	1.00
93. Total Investment Value	93.00	46.50	31.00	23.25	18.60	15.50	13.29	11.14	1.00
94. Total Investment Value	94.00	47.00	31.33	23.50	18.80	15.67	13.43	11.26	1.00
95. Total Investment Value	95.00	47.50	31.67	23.75	19.00	15.83	13.57	11.38	1.00
96. Total Investment Value	96.00	48.00	32.00	24.00	19.20	16.00	13.71	11.50	1.00
97. Total Investment Value	97.00	48.50	32.33	24.25	19.40	16.17	13.86	11.62	1.00
98. Total Investment Value	98.00	49.00	32.67	24.50	19.60	16.33	14.00	11.74	1.00
99. Total Investment Value	99.00	49.50	33.00	24.75	19.80	16.50	14.14	11.86	1.00
100. Total Investment Value	100.00	50.00	33.33	25.00	20.00	16.67	14.29	11.98	1.00
101. Total Investment Value	101.00	50.50	33.67	25.25	20.20	16.83	14.43	12.10	1.00
102. Total Investment Value	102.00	51.00	34.00	25.50	20.40	17.00	14.57	12.22	1.00
103. Total Investment Value	103.00	51.50	34.33	25.75	20.60	17.17	14.71	12.34	1.00
104. Total Investment Value	104.00	52.00	34.67	26.00	20.80	17.33	14.86	12.46	1.00
105. Total Investment Value	105.00	52.50	35.00	26.25	21.00	17.50	15.00	12.58	1.00
106. Total Investment Value	106.00	53.00	35.33	26.50	21.20	17.67	15.14	12.70	1.00
107. Total Investment Value	107.00	53.50	35.67	26.75	21.40	17.83	15.29	12.82	1.00
108. Total Investment Value	108.00	54.00	36.00	27.00	21.60	18.00	15.43	12.94	1.00
109. Total Investment Value	110.00	54.50	36.33	27.25	21.80	18.17	15.57	13.06	1.00
110. Total Investment Value	111.00	55.00	36.67	27.50	22.00	18.33	15.71	13.18	1.00
111. Total Investment Value	112.00	55.50	37.00	27.75	22.20	18.50	15.86	13.30	1.00
112. Total Investment Value	113.00	56.00	37.33	28.00	22.40	18.67	16.00	13.42	1.00
113. Total Investment Value	114.00	56.50	37.67	28.25	22.60	18.83	16.14	13.54	1.00
114. Total Investment Value	115.00	57.00	38.00	28.50	22.80	19.00	16.29	13.66	1.00
115. Total Investment Value	116.00	57.50	38.33	28.75	23.00	19.17	16.43	13.78	1.00
116. Total Investment Value	117.00	58.00	38.67						

Pairwise comparisons									
Criteria	1	2	3	4	5	6	7	8	9
1. Total Investment Value	1.00	0.50	0.33	0.25	0.20	0.17	0.14	0.11	0.09
2. Total Investment Value	2.00	1.00	0.67	0.50	0.40				



## Limited Instrument/Environment Combined Simulation

There are two main poles, if you will, of this project: the dominant one were the studies and analyses regarding the pre-design feasibility of several potential instrument designs, while the second "pole" was developing an understanding of the environmental boundary conditions that any such instrument design would face in orbit around, or in situ upon, an asteroid in the main belt. By and large these two poles have remained separate ends of the same problem, gradually growing together toward a combination, or synthesis exercise, at the very end of the thesis project. This chapter discusses that meeting.

It is first necessary to mention that, at the risk of sounding like a broken record, computational constraints and the obvious time constraints that surround any thesis limited the amount of work that could be done in merging the two poles of this project satisfactorily. To be fair, said constraints were dominated by the computational requirements. Ideally, one would be able to place the final instrument model discussed in the Design chapter above the surface of the asteroid model described in the Simulation chapter, bombard both with GCR primaries from an all-enveloping spherical source, and observe the results. This would involve, to briefly touch upon what is described in more detail in the Normalization section of the Simulation chapter, a fairly uniform total integrated flux of around 4900-5000 GCR primaries per second per square meter per steradian. Assuming an asteroid of 100m diameter, a spacecraft orbiting at an altitude of 100m, and that the aforementioned all-enveloping spherical GCR source was of minimum possible size, it would still require the diameter of the source sphere to be no less than 100m. This would result in the need to inject and track over 7.74 billion high energy *primary* particles per second. Due to the geometry of the situation, every such primary is guaranteed to hit solid matter at least once. Assuming that the average number of secondaries can be estimated from the PDG's published average for EM air-shower events at sea level of approximately  $10^6$  particles [56], and that Prettyman et al's rough scaling factor of  $10^{-3}$  for using data from such air-shower fluxes to estimate that in planetary regolith with bulk density of  $1.6 \text{ g/cm}^3$  can be used [61], the total number of secondaries produced per second could easily exceed 7.74 trillion per second!

Thus, as discussed in the simulation chapter, it was necessary to undertake a far more detailed study of the asteroid/GCR interaction to attempt to create a more computationally efficient particle source. Ultimately, even with the spherical muon source discussed in the simulation chapter, the average transited-muon count rate at an altitude of zero for the 100m asteroid model was between 1 and 2 per square meter per day. This meant that, with a frontal area of  $1/9 \text{ m}^2$ , the final instrument design would average 1 hit approximately every 9-18 days. The spherical muon source had an overall count rate of approximately 95 muons

per second for the *whole* 100m asteroid. Thus, simulating 9-18 days would have required the injection of between 70 and 150 million muons, to say nothing of GCR primaries for background radiation. At a computational rate of approximately 67 injections per second, this would have required 2-4 weeks of non-stop computing.

These facts are included, not to induce sympathy, but as a somewhat chronological record of the logic that lead to the adoption of the final-case study boundary conditions. It was obvious that anything that approached a somewhat realistic proportional combination of GCR primaries and muons injected from the spherical source around the entire asteroid would be impractical to simulate over the required timescales. So, it was decided to approximate a very small portion of the spherical muon source, under the regolith, directly opposite from the instrument. Then, if the angular distribution of injected muons was restricted to a maximum azimuth and elevation deviation of 0.5 degrees from zero, it was possible to inject enough muons over a short enough timescale to achieve a hit on the sensitive area of the instrument. At the aforementioned approximate asteroid-wide count rate of 95 muons per second, scaled down to the approximate surface area of a spherical sector 2 meters in diameter, with a cosine distribution limited to between 0 and 0.5 degrees of deviation from the normal vector, one could expect no more than 1.817 muon strikes per square meter per year on the asteroid surface opposing the source. The computational steps taken to derive this count rate are detailed below:

$$CR_{partial} = \sum_{i=1}^{bins} I_{N_i} E_i A_{partial} \Omega_{partial} \quad (B.1)$$

Where the total count rate of the partial muon source,  $CR_{partial}$ , can be calculated by taking the sum of all the individual count rates over each data bin,  $i$  (note that this could also be integrated if the width of the bins approached zero). This equation is derived simply from the definition of the integrated flux. The critically different part to mention here is the calculation of the solid angle,  $\Omega_{partial}$ . The major variables in this calculation are illustrated below:

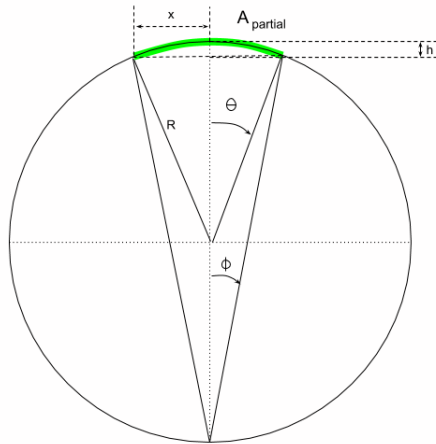


Figure B.1: Schematic representation of  $A_{partial}$  particle source area

It is possible to relate the area of a spherical sector ( $A = 2\pi Rh$ ) to the azimuth/elevation angle

$\phi$  shown in Figure B.1. This is shown below:

$$x = R \sin(\theta) \quad (\text{B.2a})$$

$$\tan(\phi) = \frac{x}{2R} = \frac{R \sin(\theta)}{2R} \quad (\text{B.2b})$$

$$\theta = \sin^{-1}(2 \tan(\phi)) \quad (\text{B.2c})$$

$$R - h = R \cos(\theta) \quad (\text{B.2d})$$

$$h = R(1 - \cos(\sin^{-1}(2 \tan(\phi)))) \quad (\text{B.2e})$$

$$A_{\text{partial}} = 2\pi R^2(1 - \cos(\sin^{-1}(2 \tan(\phi)))) \quad (\text{B.2f})$$

The last step in Equation B.2a shows the area of the spherical sector as a function of the azimuth/elevation deviation angle  $\phi$ . From there, it is trivial to compute the solid angle,  $\Omega_{\text{partial}}$ :

$$\Omega_{\text{partial}} = \frac{A_{\text{partial}}}{A_{\text{sphere}}} 4\pi [\text{sr}] \quad (\text{B.3a})$$

$$\Omega_{\text{partial}} = \frac{1}{2}(1 - \cos(\sin^{-1}(\tan(\phi)))) [\text{sr}] \quad (\text{B.3b})$$

Using Equation B.3a with Equation B.1 yields the 1.817 muon per year count rate mentioned previously.

A critical piece of information to make note of is that no tomography is possible with such a particle source because tomography would require hits from a far wider solid angle. It would be possible to determine the average density along the trajectory between the source and the detector, but likely not much else. Furthermore, even with this much decreased muon source, and the smallest possible GCR source surrounding the detector itself, the ratio of muon count rate to GCR primary count rate would still require the injection of enormous numbers of particles to maintain what might be called the "natural proportion." Thus, the second major logical step in designing a practical integrated simulation was the recollection of the result of the first parametric study detailed in the Design chapter.

In brief, a recapitulation of this study was that two major parameters were changed, the average incidence angle of the proton/electron/muon test beam, and, relevant here, the proportion of muons with respect to all other test beam particles. Referring back to Figure 4.14 and Figure 4.15 (reproduced below), it is evident that, even when the proportion of muons was increased by an *order of magnitude*, the instrument's detection efficiency (left pane) displayed only a very small sensitivity to the mix change.

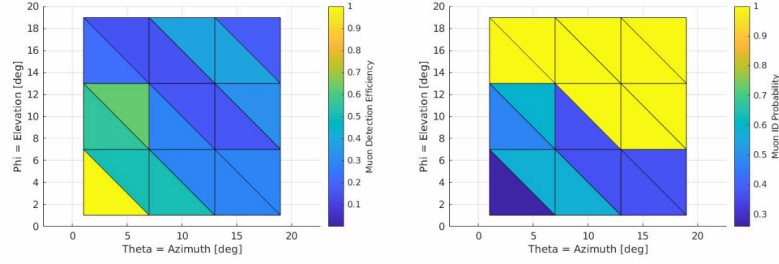


Figure B.2: Effect on Muon Detection Efficiency AND Muon ID Probability of altering instrument elevation and azimuth angles with respect to bulk direction of incident particles. This run used a higher proportion of muons, 25%

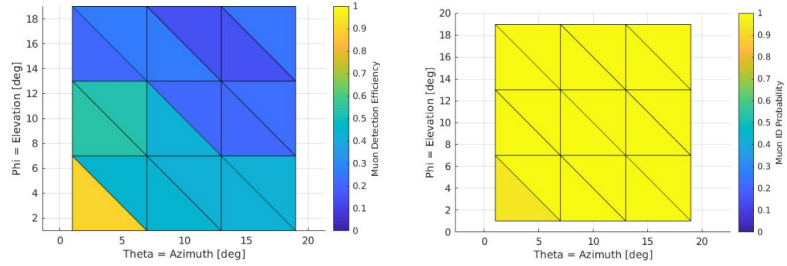


Figure B.3: Effect on Muon Detection Efficiency AND Muon ID Probability of altering instrument elevation and azimuth angles with respect to bulk direction of incident particles. This run used a higher proportion of muons, 250%

And, while the MIDP metric (right pane) did show an increase, this is simply an artifact of the fact that when the proportion of muons is increased to be more than 75% of the total mix, the probability that any particle detected is a muon also increases drastically, *regardless* of instrument design or active shielding algorithm. The instrument detection efficiency, therefore, is negligibly affected by the increase of muon proportion. At a higher level, this relates to the non-simultaneity assumption detailed in the Design chapter. Basically, it is highly improbable that any two primary particles hit the detector simultaneously; increasing the muon flux, even by orders of magnitude, does not effectively change this. Thus, the detector efficiency can still be usefully measured with an artificially increased muon flux, and an unnaturally low ratio of GCR primaries to transiting muons. This was the critical analytical step that lead to the conclusion that it was worthwhile at all to pursue such a lopsided simulation. The MDE could be assessed at several altitudes, though the MIDP metric would be saturated and not very useful.

Ultimately, the primary impact of this integrated study is provide a very similar simulation to that used in the geometric parametric study with the muon test beam source much more accurate in terms, not only of kinetic energy at injection, but also in terms of energy at emergence. So, from the perspective of evaluating instrument design, this study was worthwhile, if not as realistic as had originally been hoped.

Because Geant4 does not currently support hemispherical sources, the spherical sector area described in Equation B.2a was not possible. It was, instead, approximated by a disk source that was both concentric and co-radial with the spherical sector. Because the radius of the sector is much smaller than the radius of the muon particle source itself ( $x \ll R$ ), the sector was nearly flat in any case, so the area difference was negligible. Like the hemispherical muon source would have been, this disk source was placed below the surface of the asteroid model at a depth of approximately 3 meters. The instrument itself was surrounded by a cylindrical GCR source of radius just large enough to envelope the instrument without touching (0.25m), and appreciably greater length than the detector (though the foremost edge was coplanar with the front surface of the detector) to reasonably approximate a GCR source covering a solid angle of  $2\pi$  steradians. This, again, was done because a hemispherical source (which would

have been perfect) is not currently possible in Geant4.

Both partial muon source and cylindrical GCR source were lent the same probability of particle generation (50% / 50 % muon to background proportion) to speed up computation. Each run consisted of 10,000 injected particles (which equates to approximately 2500 years of muon strikes, and about 0.63 seconds of GCR primary strikes). One run was performed for incrementally increased altitudes at intervals of 5 meters. The resulting MDE as a function of altitude plot is shown below:

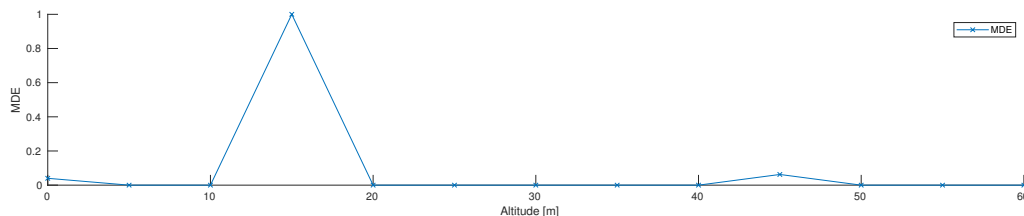


Figure B.4: Effect of increasing altitude above asteroid model surface on detector MDE

The statistical significance of the particle simulation results was just barely adequate to generate any MDE estimate at all; Figure B.4 is useful only for rough qualitative assessment. This was a function, lamentably yet again, of lack of computation time. However, all of the effort may prove worthwhile in that it allows 2 such qualitative assessments:

- The MDE is very low at most altitudes.
- There are 2 observable spikes of higher MDE that, interestingly, correspond to 2 spikes in the maximum muon count rate, computed in the Simulation chapter.

The combination of these observations yields: Firstly a place to start when any future work or analysis is performed upon the optimum altitude of a muographic instrument in orbit around an asteroid. And secondly, a corroboration that indicates that, while very coarse, the MDE assessment mirrors the count-rate peaks observed at 20m and 50m of altitude respectively.

From a point of view at the very end of this thesis project, but perhaps at the very start of future work on this topic, it is perhaps appropriate to offer an explanation of this phenomenon not in the form of a conclusion based upon sadly sparse data, but a hypothesis that may, once again, prove useful as a starting place: It is suggested that the spikes in both MDE and maximum muon count rate in altitude bands around the asteroid model may be due to a geometric "sweet spot" where the high-incidence angle transited muons that are otherwise invisible to the detector become detectable en masse for a brief altitude-window before they suffer extinction.

With that, it is, perhaps worthwhile to offer a final conclusion on the convergence of the two poles of this project. While a perfect exemplar of such a convergence would be a fully integrated simulation, and the much pared-down simulation presented here is a poor substitute for that at best, the two poles of the project can come together analytically in a much more useful way where the separate simulation results of the separate domains (instrument and environment) can be combined retro-actively to yield useful design recommendations. This will be discussed further in the final chapter outlining the overall results of the project.

# Bibliography

- [1] Interaction of Particles with Matter. Technical report, University of Florida, Department of Physics, Gainesville, Florida. URL [http://www.phys.ufl.edu/~korytov/tmp4/lectures/note\\_A10\\_interaction\\_of\\_particles\\_with\\_matter.pdf](http://www.phys.ufl.edu/~korytov/tmp4/lectures/note_A10_interaction_of_particles_with_matter.pdf).
- [2] Missions to asteroids. URL <http://sci.esa.int/rosetta/54342-missions-to-asteroids/>.
- [3] Psyche Mission – A Mission to a Metal World. URL <https://psyche.asu.edu/>.
- [4] Refractive index of SCHOTT - BK (Borosilicate crown) - N-BK7. URL <https://refractiveindex.info/?shelf=glass&book=SCHOTT-BK&page=N-BK7>.
- [5] Space in Images - Missions - Rosetta, 2013. URL [http://www.esa.int/spaceinimages/Missions/Rosetta/\(class\)/image?mission=Rosetta&type=I](http://www.esa.int/spaceinimages/Missions/Rosetta/(class)/image?mission=Rosetta&type=I).
- [6] BC-408, BC-412, BC-416 | Products | Saint-Gobain Crystals, 2018. URL <https://www.crystals.saint-gobain.com/products/bc-408-bc-412-bc-416>.
- [7] Eljen Technology - EJ-200, EJ-204, EJ-208, EJ-212, 2018. URL <https://eljentechnology.com/products/plastic-scintillators/ej-200-ej-204-ej-208-ej-212>.
- [8] Geant4 Book For Application Developers — Book For Application Developers 10.4 documentation, 2018. URL <http://geant4-userdoc.web.cern.ch/geant4-userdoc/UsersGuides/ForApplicationDeveloper/html/>.
- [9] NASA Technical Standards | NASA Technical Standards System (NTSS), 2018. URL <https://standards.nasa.gov/nasa-technical-standards>.
- [10] Various Definitions, 2018. URL <https://www.merriam-webster.com/dictionary/planet>.
- [11] H.S. Ahn, P. Allison, M.G. Bagliesi, J.J. Beatty, G. Bigongiari, P. Boyle, J.T. Childers, N.B. Conklin, S. Coutu, M.A. DuVernois, O. Ganel, J.H. Han, J.A. Jeon, K.C. Kim, J.K. Lee, M.H. Lee, L. Lutz, P. Maestro, A. Malinin, P.S. Marrocchesi, S.A. Minnick, S.I. Mognet, S.W. Nam, S.L. Nutter, I.H. Park, N.H. Park, E.S. Seo, R. Sina, S.P. Swordy, S.P. Wakely, J. Wu, J. Yang, Y.S. Yoon, R. Zei, and S.Y. Zinn. The Cosmic Ray Energetics And Mass (CREAM) instrument. *Nuclear Instruments and Methods in Physics Research Section A: Accelerators, Spectrometers, Detectors and Associated Equipment*, 579(3):1034–1053, 9 2007. ISSN 0168-9002. doi: 10.1016/J.NIMA.2007.05.203. URL <https://www.sciencedirect.com/science/article/pii/S0168900207010194>.
- [12] O C Allkofer, K Carstensen, and W D Dau. The Absolute Cosmic Ray Muon Spectrum At Sea Level. *Physics Letters B*, 36B(4):425–427, 1971. URL [https://ac.els-cdn.com/0370269371907416/1-s2.0-0370269371907416-main.pdf?\\_tid=spdf-28cc1048-4024-4408-b3fe-dd1fe33e5118&acdnat=1519921804\\_ae6e5217eb887c9e260f8206baf947d5](https://ac.els-cdn.com/0370269371907416/1-s2.0-0370269371907416-main.pdf?_tid=spdf-28cc1048-4024-4408-b3fe-dd1fe33e5118&acdnat=1519921804_ae6e5217eb887c9e260f8206baf947d5).
- [13] K. Amako, S. Guatelli, V. Ivanchenko, M. Maire, B. Mascialino, K. Murakami, L. Pandola, S. Parlati, M.G. Pia, M. Piergentili, T. Sasaki, and L. Urban. Geant4 and its validation. *Nuclear Physics B - Proceedings Supplements*, 150:44–49, 1 2006. ISSN 0920-5632. doi: 10.1016/J.NUCLPHYSBPS.2004.10.083. URL <https://www.sciencedirect.com/science/article/pii/S0920563205008066>.

- [14] F Anghinolfi, P Jarron, F Krummenacher, E Usenko, and M C S Williams. NINO: An Ultrafast Low-Power Front-End Amplifier Discriminator for the Time-of-Flight Detector in the ALICE Experiment. *IEEE TRANSACTIONS ON NUCLEAR SCIENCE*, 51(5), 2004. doi: 10.1109/TNS.2004.836048. URL <http://cds.cern.ch/record/818530/files/cer-002505863.pdf>.
- [15] Erik Asphaug, Eileen V Ryan, and Maria T Zuber. Asteroid Interiors. URL <https://www.lpi.usra.edu/books/AsteroidsIII/pdf/3038.pdf>.
- [16] Spencer N. Axani, Janet M. Conrad, and Conor Kirby. The Desktop Muon Detector: A simple, physics-motivated machine- and electronics-shop project for university students. 6 2016. doi: 10.1119/1.5003806. URL <http://arxiv.org/abs/1606.01196><http://dx.doi.org/10.1119/1.5003806>.
- [17] G D Badhwar and P M O 'neill. GALACTIC COSMIC RADIATION MODEL AND ITS APPLICATIONS. 1717(22295):7-273, 1996. URL [https://ac.els-cdn.com/027311779500507B/1-s2.0-027311779500507B-main.pdf?\\_tid=spdf-80aaf5d8-3512-4ce5-8888-559e2b9a8534&acdnat=1519921991\\_e3f9e1818fa873868fc5765ee8990df0](https://ac.els-cdn.com/027311779500507B/1-s2.0-027311779500507B-main.pdf?_tid=spdf-80aaf5d8-3512-4ce5-8888-559e2b9a8534&acdnat=1519921991_e3f9e1818fa873868fc5765ee8990df0).
- [18] F. Barao. AMS—Alpha Magnetic Spectrometer on the International Space Station. *Nuclear Instruments and Methods in Physics Research Section A: Accelerators, Spectrometers, Detectors and Associated Equipment*, 535(1-2):134-138, 12 2004. ISSN 0168-9002. doi: 10.1016/J.NIMA.2004.07.196. URL <https://www.sciencedirect.com/science/article/pii/S0168900204015888>.
- [19] Zane W Bell. Scintillation Counters. Technical report, Oak Ridge National Laboratory, Oak Ridge, Tennessee, USA, 2012. URL [https://link.springer.com/content/pdf/10.1007%2F978-3-642-13271-1\\_15.pdf](https://link.springer.com/content/pdf/10.1007%2F978-3-642-13271-1_15.pdf).
- [20] Richard Binzel, Junichi Watanabe, Iwan Williams, Owen Gingerich, and Catherine Cesarsky. The Final IAU Resolution on the definition of “planet”; ready for voting | Press Releases | IAU, 2006. URL <https://www.iau.org/news/pressreleases/detail/iau0602/>.
- [21] J.B. BIRKS. INTRODUCTION. In *The Theory and Practice of Scintillation Counting*. Elsevier, 1964. ISBN 9780080104720. doi: 10.1016/B978-0-08-010472-0.50006-9. URL <http://linkinghub.elsevier.com/retrieve/pii/B9780080104720500069>.
- [22] D T Britt, D Yeomans, K Housen, and G Consolmagno. Asteroid Density, Porosity, and Structure. URL <https://www.lpi.usra.edu/books/AsteroidsIII/pdf/3022.pdf>.
- [23] E. V. Bugaev, A. Misaki, V. A. Naumov, T. S. Sinigovskaya, S. I. Sinigovsky, and N. Takahashi. Atmospheric muon flux at sea level, underground, and underwater. *Physical Review D*, 58(5):054001, 7 1998. ISSN 0556-2821. doi: 10.1103/PhysRevD.58.054001. URL <https://link.aps.org/doi/10.1103/PhysRevD.58.054001>.
- [24] Schelte J Bus and Richard P Binzel. Phase II of the Small Main-Belt Asteroid Spectroscopic Survey A Feature-Based Taxonomy. *Icarus*, 158:146-177, 2002. doi: 10.1006/icar.2002.6856. URL [https://ac.els-cdn.com/S0019103502968569/1-s2.0-S0019103502968569-main.pdf?\\_tid=53e89abf-19f4-47f5-a1d8-eb2273a9b802&acdnat=1522145589\\_aef26df884882936d3eff63ffb538b1e](https://ac.els-cdn.com/S0019103502968569/1-s2.0-S0019103502968569-main.pdf?_tid=53e89abf-19f4-47f5-a1d8-eb2273a9b802&acdnat=1522145589_aef26df884882936d3eff63ffb538b1e).
- [25] Leszek Czechowski. Planetology and classification of the solar system bodies. doi: 10.1016/j.asr.2006.09.004. URL [https://ac.els-cdn.com/S0273117706004807/1-s2.0-S0273117706004807-main.pdf?\\_tid=13074b6a-87e0-49f0-a481-fd9918606787&acdnat=1522140752\\_3826f957f53eecddec277e19fbf39726b](https://ac.els-cdn.com/S0273117706004807/1-s2.0-S0273117706004807-main.pdf?_tid=13074b6a-87e0-49f0-a481-fd9918606787&acdnat=1522140752_3826f957f53eecddec277e19fbf39726b).



- [26] G De Angelis, JM Clem, SR Blattnig, MS Cloudsley, Je Nealy, RK Tripathi, and JW Wilson. Modeling of the Lunar Radiation Environment. doi: 10.1016/j.nuclphysbps.2006.12.034. URL [https://ac.els-cdn.com/S0920563206010164/1-s2.0-S0920563206010164-main.pdf?\\_tid=db9cfcc2-60fa-442f-8969-3b161a3ed23e&acdnat=1522759804\\_f9d237325af80fdd4dde4e94be8dedc7](https://ac.els-cdn.com/S0920563206010164/1-s2.0-S0920563206010164-main.pdf?_tid=db9cfcc2-60fa-442f-8969-3b161a3ed23e&acdnat=1522759804_f9d237325af80fdd4dde4e94be8dedc7).
- [27] Marcos Dracos. A Particle Identification Method for Ring Imaging Cherenkov Detectors. *Nuclear Instruments and Methods in Physics Research*, 1995. URL <http://lss.fnal.gov/archive/other/crn-95-21.pdf>.
- [28] ESA. Asteroids: The discovery of asteroids / ESA history / Welcome to ESA / About Us / ESA, 2018. URL [https://www.esa.int/About\\_Us/Welcome\\_to\\_ESA/ESA\\_history/Asteroids\\_The\\_discovery\\_of\\_asteroids](https://www.esa.int/About_Us/Welcome_to_ESA/ESA_history/Asteroids_The_discovery_of_asteroids).
- [29] S-O Flyckt and Carole Marmonier. PHOTOMULTIPLIER TUBES principles & applications. Technical report, Photonis Inc., Brive, 2002. URL [http://www2.pv.infn.it/~debari/doc/Flyckt\\_Marmonier.pdf](http://www2.pv.infn.it/~debari/doc/Flyckt_Marmonier.pdf).
- [30] I. Frank and Ig. Tamm. Coherent Visible Radiation of Fast Electrons Passing Through Matter. In *Selected Papers*, pages 29–35. Springer Berlin Heidelberg, Berlin, Heidelberg, 1991. doi: 10.1007/978-3-642-74626-0\2. URL [http://www.springerlink.com/index/10.1007/978-3-642-74626-0\\_2](http://www.springerlink.com/index/10.1007/978-3-642-74626-0_2).
- [31] A Fujiwara, J Kawaguchi, D K Yeomans, M Abe, T Mukai, T Okada, J Saito, H Yano, M Yoshikawa, D J Scheeres, O Barnouin-Jha, A F Cheng, H Demura, R W Gaskell, N Hirata, H Ikeda, T Kominato, H Miyamoto, A M Nakamura, R Nakamura, S Sasaki, and K Uesugi. The Rubble-Pile Asteroid Itokawa as Observed by Hayabusa. URL <http://science.sciencemag.org/content/sci/312/5778/1330.full.pdf>.
- [32] Robert Gaskell. 25143 Itokawa CAD Shape File. URL <https://darts.isas.jaxa.jp/planet/project/hayabusa/shape.pl>.
- [33] geant4; Cern. Physics reference manual - geant4. 1(December), 2013. URL <https://indico.cern.ch/event/679723/contributions/2792554/attachments/1559217/2454299/PhysicsReferenceManual.pdf>.
- [34] Thomas K. Geisser. *Cosmic Rays and Particle Physics*. Cambridge University Press, Cambridge, 1 edition, 1990. ISBN 0 521 32667 2. URL <http://alpha.sinp.msu.ru/~panov/Gaisser1990.pdf>.
- [35] Peter K F Grieder and A G Wright. A critical evaluation of theories of direct electron pair production by muons. *Journal of Physics A: Mathematical, Nuclear and General J. Phys. A : Math. Nucl. Gen.*, 6(0), 1973. URL <http://iopscience.iop.org/article/10.1088/0305-4470/6/1/008/pdf>.
- [36] David Griffiths. *INTRODUCTION TO ELEMENTARY PARTICLES*. Morlenbach, Germany, 2 edition, 2004. ISBN 978-0-471-60386-3.
- [37] David J. Griffiths. *INTRODUCTION TO ELECTRODYNAMICS*. Pearson, Boston, 4 edition, 2013. ISBN 978-0-321-85656-2. URL [http://kestrel.nmt.edu/~mce/griffiths\\_4.pdf](http://kestrel.nmt.edu/~mce/griffiths_4.pdf).
- [38] Hamamatsu Corporation. Si detectors for high energy particles. Technical report, Hamamatsu Photonics Inc., Hamamatsu City, 2018. URL [https://www.hamamatsu.com/resources/pdf/ssd/e10\\_handbook\\_for\\_high\\_energy.pdf](https://www.hamamatsu.com/resources/pdf/ssd/e10_handbook_for_high_energy.pdf).
- [39] E H M Heijne. ORGANISATION EUROPÉENNE POUR LA RECHERCHE NUCLÉAIRE MUON FLUX MEASUREMENT WITH SILICON DETECTORS IN THE CERN NEUTRINO BEAMS. Technical report, CERN, Geneva, 1983. URL [http://www.iaea.org/inis/collection/NCLCollectionStore/\\_Public/15/007/15007010.pdf](http://www.iaea.org/inis/collection/NCLCollectionStore/_Public/15/007/15007010.pdf).

- [40] D Heynderickx, B Quaghebeur, E Speelman, E Daly, and E J Daly. ESA's Space Environment Information System (SPENVIS): A WWW Interface to Models of the Space Environment and its Effects. ISSN 2000-0371. doi: 10.2514/6.2000-371. URL <https://arc.aiaa.org/doi/pdf/10.2514/6.2000-371>.
- [41] David Hodge. Technical University of Delft Faculty of Aerospace Engineering Literature Review :. 2018.
- [42] Jiangchuan Huang, Jianghui Ji, Peijian Ye, Xiaolei Wang, Jun Yan, Linzhi Meng, Su Wang, Chunlai Li, Yuan Li, Dong Qiao, Wei Zhao, Yuhui Zhao, Tingxin Zhang, Peng Liu, Yun Jiang, Wei Rao, Sheng Li, Changning Huang, Wing-Huen Ip, Shoucun Hu, Menghua Zhu, Liangliang Yu, Yongliao Zou, Xianglong Tang, Jianyang Li, Haibin Zhao, Hao Huang, Xiaojun Jiang, and Jinming Bai. The Ginger-shaped Asteroid 4179 Toutatis: New Observations from a Successful Flyby of Chang'e-2. *Scientific Reports*, 3(1):3411, 12 2013. ISSN 2045-2322. doi: 10.1038/srep03411. URL <http://www.nature.com/articles/srep03411>.
- [43] E.T. Jaynes. *Probability Theory: The Logic of Science*. Cambridge University Press, Cambridge, 2 edition, 2003. ISBN 0521592712.
- [44] J.V. Jelley. Cerenkov Radiation and its applications. Technical report, United Kingdom Atomic Energy Authority, London, 1958. URL <https://ia802508.us.archive.org/18/items/cerenkovradiatio030980mbp/cerenkovradiatio030980mbp.pdf>.
- [45] Hiroyuki K M Tanaka and Izumi Yokoyama. Muon radiography and deformation analysis of the lava dome formed by the 1944 eruption of Usu, Hokkaido—contact between high-energy physics and volcano physics—. *Proceedings of the Japan Academy. Series B, Physical and biological sciences*, 84(4):107–16, 2008. ISSN 1349-2896. doi: 10.2183/PJAB.84.107. URL <http://www.ncbi.nlm.nih.gov/pubmed/18941290><http://www.pubmedcentral.nih.gov/articlerender.fcgi?artid=PMC2805507>.
- [46] Cornelis Klein, Cornelius Searle Hurlbut, and James Dwight Dana. *Manual of mineralogy (after James D. Dana) Cornelis Klein, Cornelius S. Hurlbut, Jr. [electronic resource] - Version details - Trove*. Wiley, New York, 20 edition, 1985. ISBN 0471805807. URL [https://trove.nla.gov.au/work/8455391?q&sort=holdings+desc&\\_id=1537252600650&versionId=207919346](https://trove.nla.gov.au/work/8455391?q&sort=holdings+desc&_id=1537252600650&versionId=207919346).
- [47] Pa010 Lipari. Lepton spectra in the earth's atmosphere. URL [https://ac.els-cdn.com/0927650593900226/1-s2.0-0927650593900226-main.pdf?\\_tid=5299555d-1076-4809-b894-6cfddbe3f5a3&acdnat=1519923757\\_26395758dcac54e9956292ea9596e007](https://ac.els-cdn.com/0927650593900226/1-s2.0-0927650593900226-main.pdf?_tid=5299555d-1076-4809-b894-6cfddbe3f5a3&acdnat=1519923757_26395758dcac54e9956292ea9596e007).
- [48] Jack J. Lissauer and Imke de Pater. *Fundamental Planetary Science*. Cambridge University Press, Cambridge, 1 edition, 2014. ISBN 978-0-521-85339-9. URL [http://assets.cambridge.org/97805218/53309/frontmatter/9780521853309\\_frontmatter.pdf](http://assets.cambridge.org/97805218/53309/frontmatter/9780521853309_frontmatter.pdf).
- [49] Andrew T McNichols. VARIABLE ALTITUDE MUON DETECTION AND ENERGY DEPENDENCE OF COSMIC RAY MUONS. URL [http://www.spacegrant.hawaii.edu/reports/23\\_SUM13-SP14/AMcNichols\\_S14.pdf](http://www.spacegrant.hawaii.edu/reports/23_SUM13-SP14/AMcNichols_S14.pdf).
- [50] Marcus H. Mendenhall and Robert A. Weller. A probability-conserving cross-section biasing mechanism for variance reduction in Monte Carlo particle transport calculations. *Nuclear Instruments and Methods in Physics Research Section A: Accelerators, Spectrometers, Detectors and Associated Equipment*, 667:38–43, 3 2012. ISSN 01689002. doi: 10.1016/j.nima.2011.11.084. URL <http://linkinghub.elsevier.com/retrieve/pii/S0168900211021541>.
- [51] Paul Monk. *Physical Chemistry*. John Wiley & Sons Ltd., Chichester, 1 edition, 2004. ISBN 0-471-49180-2. URL [https://astro.ins.urfu.ru/sites/default/files/upload\\_files/temp/1/%5BPaul\\_M.\\_S.\\_Monk%5D\\_Physical\\_Chemistry\\_Understandin\(BookSee.org\).pdf](https://astro.ins.urfu.ru/sites/default/files/upload_files/temp/1/%5BPaul_M._S._Monk%5D_Physical_Chemistry_Understandin(BookSee.org).pdf).

- [52] C. L. MORRIS, C. C. ALEXANDER, J. D. BACON, K. N. BOROZDIN, D. J. CLARK, R. CHARTRAND, C. J. ESPINOZA, A. M. FRASER, M. C. GALASSI, J. A. GREEN, J. S. GONZALES, J. J. GOMEZ, N. W. HENGARTNER, G. E. HOGAN, A. V. KLIMENKO, M. F. MAKELA, P. McGAUGHEY, J. J. MEDINA, F. E. PAZUCHANICS, W. C. PRIEDHORSKY, J. C. RAMSEY, A. SAUNDERS, R. C. SCHIRATO, L. J. SCHULTZ, M. J. SOSSONG, and G. S. BLANPIED. Tomographic Imaging with Cosmic Ray Muons. *Science & Global Security*, 16(1-2):37–53, 10 2008. ISSN 0892-9882. doi: 10.1080/08929880802335758. URL <https://www.tandfonline.com/doi/full/10.1080/08929880802335758>.
- [53] M M Mukaka. Statistics corner: A guide to appropriate use of correlation coefficient in medical research. *Malawi medical journal : the journal of Medical Association of Malawi*, 24(3):69–71, 9 2012. ISSN 1995-7270. URL <http://www.ncbi.nlm.nih.gov/pubmed/23638278><http://www.pubmedcentral.nih.gov/articlerender.fcgi?artid=PMC3576830>.
- [54] et al Nakamura, K. Particle Data Group, Review of Particle Physics: Part 33 - Particle Detectors. Technical report, Lawrence Berkely National Laboratory, 2015. URL <http://pdg.lbl.gov/2015/reviews/rpp2015-rev-particle-detectors-accel.pdf>.
- [55] et al Nakamura, K. 33. Passage of particles through matter 1. In *Review of Particle Physics*. 2016. URL <http://pdg.lbl.gov/2016/reviews/rpp2016-rev-passage-particles-matter.pdf>.
- [56] K Nakamura. 24. Cosmic Rays. Technical report, Lawrence Berkely National Laboratory, 2011.
- [57] M V Nemallapudi, S Gundacker, P Lecoq, and E Auffray. Single Photon Time Resolution of state of the art SiPMS. *Journal of Instrumentation*, 11(P10016), 2016. doi: 10.1088/1748-0221/11/10/P10016. URL <http://iopscience.iop.org/article/10.1088/1748-0221/11/10/P10016/pdf>.
- [58] T. Noguchi, T. Nakamura, M. Kimura, M. E. Zolensky, M. Tanaka, T. Hashimoto, M. Konno, A. Nakato, T. Ogami, A. Fujimura, M. Abe, T. Yada, T. Mukai, M. Ueno, T. Okada, K. Shirai, Y. Ishibashi, R. Okazaki, Mitsuru Ebihara, Trevor R. Ireland, Fumio Kitajima, Keisuke Nagao, Hiroshi Naraoka, Takaaki Noguchi, Ryuji Okazaki, Hisayoshi Yurimoto, Michael E. Zolensky, Toshifumi Mukai, Masanao Abe, Toru Yada, Akio Fujimura, Makoto Yoshikawa, and Junichiro Kawaguchi. Incipient Space Weathering Observed on the Surface of Itokawa Dust Particles. *Science*, 333(6046):1121–1125, 8 2011. ISSN 0036-8075. doi: 10.1126/science.1207794. URL <http://www.ncbi.nlm.nih.gov/pubmed/21868670><http://www.sciencemag.org/cgi/doi/10.1126/science.1207794>.
- [59] Slawomir Piatek. A technical guide to silicon photomultipliers (SiPM) | Hamamatsu Photonics, 2017. URL [https://www.hamamatsu.com/us/en/community/optical\\_sensors/articles/technical\\_guide\\_to\\_silicon\\_photomultipliers\\_sipm/index.html#what\\_is\\_pde](https://www.hamamatsu.com/us/en/community/optical_sensors/articles/technical_guide_to_silicon_photomultipliers_sipm/index.html#what_is_pde).
- [60] Jordi Poch and Isabel Villaescusa. Orthogonal Distance Regression: A Good Alternative to Least Squares for Modeling Sorption Data. *Journal of Chemical & Engineering Data*, 57(2):490–499, 2 2012. ISSN 0021-9568. doi: 10.1021/je201070u. URL <http://pubs.acs.org/doi/10.1021/je201070u>.
- [61] T H Prettyman, S L Koontz, L S Pinsky, A Empl, D W Mittlefehldt, B D Reddell, and M V Sykes. Deep Mapping of Small Solar System Bodies with Galactic Cosmic Ray Secondary Particle Showers. Technical report, NASA Innovative Advanced Concepts, Houston, 2014. URL [https://www.nasa.gov/sites/default/files/files/Prettyman\\_2013\\_PhI\\_MuonDeepMapping.pdf](https://www.nasa.gov/sites/default/files/files/Prettyman_2013_PhI_MuonDeepMapping.pdf).
- [62] S.P. Puri. *Classical Electrodynamics*. Alpha Sciene International Inc., Oxford, 1st edition, 2011. ISBN 978-1-84265-658-7.

- [63] R.W. Saaty. The analytic hierarchy process—what it is and how it is used. *Mathematical Modelling*, 9(3-5):161–176, 1 1987. ISSN 0270-0255. doi: 10.1016/0270-0255(87)90473-8. URL <https://www.sciencedirect.com/science/article/pii/0270025587904738>.
- [64] Quintin G Schiller, Abhishek Mahendrakumar, and Xinlin Li Advisor. REPTile: A Miniaturized Detector for a CubeSat Mission to Measure Relativistic Particles in Near-Earth Space. URL <https://digitalcommons.usu.edu/cgi/viewcontent.cgi?article=1226&context=smallsat>.
- [65] SensL Corporation. ArrayC – SensL, 2017. URL <http://sensl.com/products/sipmarrays/arrayc/>.
- [66] SensL Corporation. Introduction to SiPM - Technical Note. Technical report, SensL Technologies Ltd., Cork, 2017. URL <https://www.sensl.com/downloads/ds/TN-IntrotoSPMTech.pdf>.
- [67] Garrett Shea, editor. *NASA Systems Engineering Handbook Revision 2*. NASA Office of the Chief Engineer, Washington DC, 2 edition, 2017. ISBN 978-0-16-079747-7. URL <https://www.nasa.gov/connect/ebooks/nasa-systems-engineering-handbook>.
- [68] Haroon Siddique. Luxembourg aims to be big player in possible asteroid mining | Science | The Guardian, 2016. URL <https://www.theguardian.com/science/2016/feb/03/luxembourg-aims-to-be-big-player-in-possible-asteroid-mining>.
- [69] Susan Solomon. 9.3 Stoichiometry of Gaseous Substances, Mixtures, and Reactions – Chemistry, 2015. URL <https://opentextbc.ca/chemistry/chapter/9-3-stoichiometry-of-gaseous-substances-mixtures-and-reactions/>.
- [70] H. K. M. Tanaka, T. Nakano, S. Takahashi, J. Yoshida, H. Ohshima, T. Maekawa, H. Watanabe, and K. Niwa. Imaging the conduit size of the dome with cosmic-ray muons: The structure beneath Showa-Shinzan Lava Dome, Japan. *Geophysical Research Letters*, 34(22):L22311, 11 2007. ISSN 0094-8276. doi: 10.1029/2007GL031389. URL <http://doi.wiley.com/10.1029/2007GL031389>.
- [71] L. Torrisi. Plastic scintillator investigations for relative dosimetry in proton-therapy. *Nuclear Instruments and Methods in Physics Research Section B: Beam Interactions with Materials and Atoms*, 170(3-4):523–530, 10 2000. ISSN 0168-583X. doi: 10.1016/S0168-583X(00)00237-8. URL <https://www.sciencedirect.com/science/article/pii/S0168583X00002378>.
- [72] Jacques P Vallée. Observations of the Magnetic Fields Inside and Outside the Solar System: From Meteorites ( $\sim 10$  attoparsecs), Asteroids, Planets, Stars, Pulsars, Masers, To Protostellar Cloudlets ( $\sim 1$  parsec). 19:319–422, 1998. URL <https://ned.ipac.caltech.edu/level5/March03/Vallee2/paper.pdf>.
- [73] D J (Jan) van der Laan, Dennis R Schaart, Marnix C Maas, Freek J Beekman, Peter Bruyndonckx, and Carel W E van Eijk. Optical simulation of monolithic scintillator detectors using GATE/GEANT4. *Physics in Medicine and Biology*, 55(6):1659–1675, 3 2010. ISSN 0031-9155. doi: 10.1088/0031-9155/55/6/009. URL <http://stacks.iop.org/0031-9155/55/i=6/a=009?key=crossref.85a99e5be09f070b21dc8586c2fe5dbc>.
- [74] Gary S. Was. *Fundamentals of Radiation Materials Science: Metals and Alloys* - GARY S. WAS - Google Books. Spring Science+Business Media, New York, 2 edition, 2017. ISBN 978-1-4939-3436-2. doi: 10.1007/978-1-4939-3438-6. URL <https://books.google.nl/books?hl=en&lr=&id=yDGmDAAQBAJ&oi=fnd&pg=PR8&dq=particle+radiation+degradation+of+metal&ots=FkfG9kj1Xs&sig=4Vr6hl06eUHsqG1Q3Q3gI1DLRA4#v=onepage&q=particle%20radiation%20degradation%20of%20metal&f=false>.

- 
- [75] James Richard. Wertz, David F. Everett, and Jeffery John. Puschell. *Space mission engineering : the new SMAD*. Microcosm Press, 2011. ISBN 1881883159. URL [https://books.google.nl/books/about/Space\\_Mission\\_Engineering.html?id=alFNMAEACAAJ&redir\\_esc=y](https://books.google.nl/books/about/Space_Mission_Engineering.html?id=alFNMAEACAAJ&redir_esc=y).
- [76] Edgar Zapata. The State of Play US Space Systems Competitiveness. Technical report, NASA Kennedy Space Center, Cape Canaveral, Florida, USA, 2018. URL <https://ntrs.nasa.gov/archive/nasa/casi.ntrs.nasa.gov/20170009967.pdf>.